Dissertation
submitted to the
Combined Faculties for the Natural Sciences
and for Mathematics
of the Ruperto-Carola University
of Heidelberg, Germany
for the degree of
Doctor of Natural Sciences

presented by
Dipl. Phys. Marc-André Pleier
born in Fulda, Germany
Oral examination: 03.07.2002

Measurement of inclusive $\Lambda/\bar{\Lambda}$ hyperon polarisation in proton nucleus collisions at 920 GeV proton beam energy

Referees: Prof. Dr. Karl-Tasso Knöpfle
Prof. Dr. Franz Eisele

Abstract

A minimum bias dataset was analysed for transverse hyperon polarisation in $pA \to \Lambda/\bar{\Lambda}\ X$ events. The data were taken in the commissioning phase of the HERA-B detector at HERA, DESY, using the proton beam of 920 GeV energy to collide with fixed target wires of different materials.

A sample of approximately 2900 Λs was obtained in a kinematical region of transverse momentum $p_t \in [0.2, 2.2]\ GeV/c$ and Feynman variable $x_F \in [-0.19, 0.03]$ and roughly 1350 $\bar{\Lambda} s$ were found in the range of $p_t \in [0.12, 1.64]\ GeV/c$ and $x_F \in [-0.13, 0.01]$.

These samples were analysed for transverse polarisation using extensive Monte Carlo studies for acceptance determination, yielding:

$$Pol(\Lambda) : 0.073\ \pm\ 0.073\ (stat)\ \pm\ 0.0095\ (syst)$$
$$Pol(\bar{\Lambda}) : 0.006\ \pm\ 0.129\ (stat)\ \pm\ 0.0381\ (syst).$$

The found result is compatible with the only other inclusive measurement that is available at $x_F < 0$. Concluding, the possible significant contribution to the field of hyperon polarisation physics of the HERA-B spectrometer due to its unique kinematical range and possibility to study A dependencies is pointed out.

Zusammenfassung

Im Rahmen dieser Arbeit wurde ein "Minimum Bias" Datensatz im Hinblick auf transversale Hyperon-Polarisation in $pA \to \Lambda/\bar{\Lambda}\ X$ Ereignissen analysiert. Die Datennahme erfolgte während der Inbetriebnahme des HERA-B Detektors am HERA Speicherring des DESY unter Verwendung des Protonenstrahls einer Energie von 920 GeV in Wechselwirkung mit Draht-Targets unterschiedlicher Materialien.

Im kinematischen Bereich von Transversalimpuls $p_t \in [0.2, 2.2]\ GeV/c$ und Feynman Variable $x_F \in [-0.19, 0.03]$ wurden hierbei ca. 2900 Λs rekonstruiert; weiterhin wurden ca. 1350 $\bar{\Lambda} s$ im Bereich von $p_t \in [0.12, 1.64]\ GeV/c$ und $x_F \in [-0.13, 0.01]$ gefunden.

Die Polarisationsanalyse dieser Hyperonen ergab unter Verwendung von detaillierten Monte Carlo Studien zur Akzeptanzbestimmung folgendes Ergebnis:

$$Pol(\Lambda) : 0.073\ \pm\ 0.073\ (stat)\ \pm\ 0.0095\ (syst)$$
$$Pol(\bar{\Lambda}) : 0.006\ \pm\ 0.129\ (stat)\ \pm\ 0.0381\ (syst).$$

Dieses Resultat ist mit der einzigen im Bereich $x_F < 0$ verfügbaren inklusiven Messung verträglich. Abschließend wird ausgeführt, daß das HERA-B Spektrometer aufgrund seines kinematischen Bereiches und der Möglichkeit, unterschiedliche Targetmaterialien einzusetzen, einen wesentlichen Beitrag zum Gebiet der Hyperon-Polarisation leisten könnte.

Contents

List of Figures

List of Tables

"The story so far:
In the beginning the Universe was created.
This has made a lot of people very angry
and been widely regarded as a bad move."
Douglas Adams,
The Restaurant at the End of the Universe

Chapter 1

Introduction

1.1 Motivation

One of the oldest questions mankind ponders on is what our world and the universe is actually made of and what its building blocks might be.

There have been many different answers so far as science explored matter to smaller and smaller dimensions to find its fundamental constituents. The present knowledge of the fundamental fermions (particles with half integral spin) synthesising matter described in the so called "Standard Model" is reflected in table 1.1. According to their hierarchy in mass, quarks and leptons are assigned to three "generations".

	charge [e]	generation		
		1.	2.	3.
quarks	$+\frac{2}{3}$	up 1 - 5 MeV/c^2	charm 1.15 - 1.35 GeV/c^2	top 174.3 $\pm$ 5.1 GeV/c^2
	$-\frac{1}{3}$	down 3 - 9 MeV/c^2	strange 75 - 170 MeV/c^2	bottom 4.0 - 4.4 GeV/c^2
leptons	0	ν_e < 3 eV/c^2	ν_μ < 0.19 MeV/c^2	ν_τ < 18.2 MeV/c^2
	-1	e 0.511 MeV/c^2	μ 105.658 MeV/c^2	τ 1777 MeV/c^2

Table 1.1: The known fundamental fermions and their masses [Gro00].

Within the Standard Model, the fundamental forces are described by gauge theories where interactions are mediated by exchange of the respective gauge bosons (particles with integral spin) as illustrated in table 1.2. One

interaction	couples to	affected particles	exchange boson	mass $[GeV/c^2]$	electric charge $[e]$	spin
strong	colour charge	quarks, gluons	gluon (g)	0	0	1
weak	flavour	quarks, leptons	W^+, W^- Z^0	80.419 91.188	+1, -1 0	1 1
electro-magnetic	electric charge	electrically charged	photon (γ)	0	0	1
gravitation	mass, energy	all	graviton (unobserved)	0	0	2

Table 1.2: The fundamental interactions and their properties [Gro00]. Gravitation is shown separately as it is not included in the Standard Model.

fundamental property of the used gauge theories is their symmetry under the combined application of the discrete symmetries C (Charge conjugation, flipping the sign of all charge like, additive quantum numbers), P (Parity, flipping the sign of all space coordinates) and T (Time, flipping the sign of the time direction). This symmetry is also called CPT invariance.

Originally, it was assumed that the interactions described by the Standard Model are also invariant under the application of each single symmetry operation C, P and T. However, in the 1950's it was found, that both C and P symmetry are violated. In 1964, Christenson et al. discovered the violation of combined CP in the K^0 system. If CPT invariance holds, this discovery corresponds to a violation of T.

The discovery of CP violation triggered the evolution of the Standard Model into the present state, since Kobayashi and Maskawa [Kob73] had to postulate the existence of at least six quark flavours in order to accommodate CP violation in the Standard Model at a time where only three quarks were known. The later discoveries of the missing three quarks were important confirmations to the model and laid the foundation to its success.

Since the CP operation corresponds to the exchange of matter with antimatter, its violation is one premise to the obvious asymmetry between matter and antimatter in our universe. It is thus of great interest to check to what extent the CP violation implemented in the Standard Model is able to describe all observed corresponding effects in nature.

Another system where CP violation is expected to occur, according to the Standard Model, is the B^0 system. Measurements of different decay modes allow to over-constrain the parameters of the Standard Model and thus to crosscheck whether the model is still valid or something new is required to describe the observations.

Several experiments have been developed to investigate the system of B^0 mesons: The BaBar [Bou95] and Belle [Che95] collaborations use dedicated electron-positron colliders to produce B mesons, whereas the HERA-B [HB94] experiment collides protons of the HERA storage ring with the nucleons of fixed target wires to produce B mesons in deeply inelastic reactions.

Due to the many technical challenges involved in the measurement of heavy flavour decays in a huge hadronic background, the ambitious time schedule of HERA-B could not be met, and the detector was still in its commissioning phase in the year 2000 data taking period.

This thesis uses the year 2000 data to explore the physics potential of HERA-B also for minimum bias data, especially for the study of hyperon polarisation. Hyperon polarisation is the effect to observe spin polarised hyperons produced in the interaction of unpolarised beam and target which is still poorly understood theoretically.

Since the whole detector design of HERA-B is oriented to the measurement of CP violation in the so-called "Golden Decay" $B^0/\bar{B}^0 \to J/\Psi K^0_s$, the next section will sketch the basic properties and ideas of this measurement, before the main focus of this thesis is addressed. The following sections will outline the known experimental properties of $\Lambda/\bar{\Lambda}$ polarisation, the corresponding theoretical models available at present and the basic theoretical considerations necessary for the polarisation measurement. Finally, an outline of the structure of this thesis is given.

1.2 CP violation in the Standard Model

The neutral current (g, γ, Z^0) eigenstates of the quarks, also called flavour, are not the eigenstates of the charged currents (W^+, W^-). The Cabibbo-Kobayashi-Maskawa (CKM) matrix [Kob73] describes the mixing of the flavour eigenstates into the charged current eigenstates. By convention, this is done by a 3 x 3 unitary matrix V_{CKM} which operates on the negatively charged flavour states d, s and b.

$$\begin{pmatrix} d' \\ s' \\ b' \end{pmatrix} = \begin{pmatrix} V_{ud} & V_{us} & V_{ub} \\ V_{cd} & V_{cs} & V_{cb} \\ V_{td} & V_{ts} & V_{tb} \end{pmatrix} \begin{pmatrix} d \\ s \\ b \end{pmatrix} \equiv \mathbf{V_{CKM}} \begin{pmatrix} d \\ s \\ b \end{pmatrix} \tag{1.1}$$

In principle, this complex matrix could have 18 independent parameters. To conserve the number of states, this matrix has to be unitary which means that only 9 free parameters remain. Additional 5 out of the 9 can be absorbed as phases in the quark wave functions. This results in 4 independent

parameters in total. Since any rotation in n dimensional space can be described with $\frac{1}{2}n(n-1)$ Euler-type angles, with three quark families there are 3 real Euler angles, resulting in the fourth parameter to be a complex phase. The imaginary component of the CKM matrix is necessary to implement CP violation in the Standard Model: If the CPT theorem holds, CP violation is equivalent to T violation which means complex conjugation of the matrix elements. If the matrix would be real, no CP violation could occur.

It is quite popular to approximate the CKM matrix as introduced by Wolfenstein [Wol83] in terms of powers of $\lambda = V_{us} \approx 0.22$ since this shows nicely the hierarchy of quark transitions:

$$\mathbf{V_{CKM}} = \begin{pmatrix} 1-\frac{1}{2}\lambda^2 & \lambda & \lambda^3 A(\rho - i\eta) \\ -\lambda & 1-\frac{1}{2}\lambda^2 & \lambda^2 A \\ \lambda^3 A(1-\rho-i\eta) & -\lambda^2 A & 1 \end{pmatrix} + \mathcal{O}(\lambda^4) \qquad (1.2)$$

This parametrisation contains four real parameters A, ρ, η, λ, where λ is the sine of the Cabibbo angle sin θ_c.

The unitarity of the CKM matrix results in six equations of the type $A + B + C = 0$ that can be visualised as triangles in the complex plane having the same area that is proportional to the "strength" of CP violation. One "common" example is:

$$V_{ud}V_{ub}^* + V_{cd}V_{cb}^* + V_{td}V_{tb}^* = 0 \qquad (1.3)$$

If we divide the above equation by the middle term $V_{cd}V_{cb}^*$, one leg of the triangle lies on the real axis from 0 to 1, and the triangle is then defined by the coordinates of a single point in the plane (ρ, η) as shown in figure 1.1. CP violation is thus implemented in the Standard Model for any $\eta \neq 0$. The three angles of this "unitarity triangle" are defined as:

$$\alpha \equiv arg\left(\frac{V_{td}V_{tb}^*}{V_{ud}V_{ub}^*}\right), \ \beta \equiv arg\left(\frac{V_{cd}V_{cb}^*}{V_{td}V_{tb}^*}\right), \ \gamma \equiv arg\left(\frac{V_{ud}V_{ub}^*}{V_{cd}V_{cb}^*}\right). \qquad (1.4)$$

The Golden Decay $B^0/\bar{B}^0 \to J/\Psi K_s^0$

The measurement of CP violation is difficult in many physical processes since the amplitudes containing products of the CKM matrix elements are modified by strong interaction corrections. In the decay channel $B^0/\bar{B}^0 \to J/\Psi K_s^0$ however, this is not true since the contributing penguin diagrams shown in figure 1.2 (b) do not destroy the CP phase to be measured (see e.g. [Har98]). In addition, this decay mode has a very good identifiable

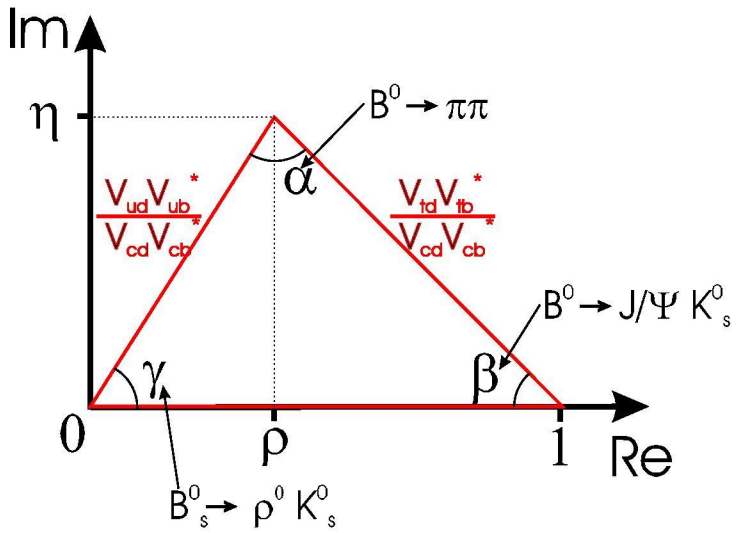

Figure 1.1: The unitarity triangle. Decays sensitive to the respective angles are indicated (see e.g. [Che95]).

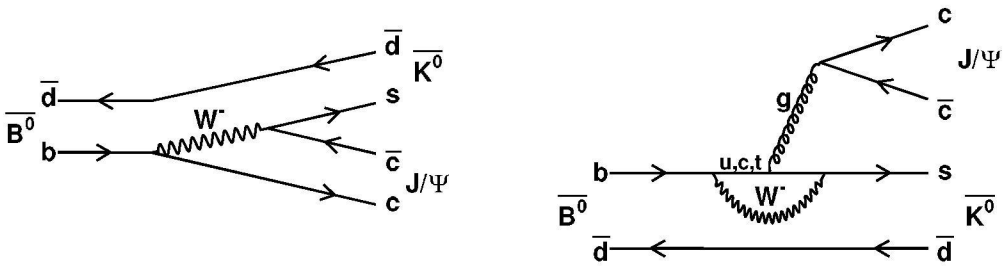

Figure 1.2: (a): Tree diagram for the golden decay (b): Penguin contributions to the golden decay.

experimental signature, as the J/Ψ can decay immediately into two leptons and the K_s^0 will decay mainly into two charged pions, yielding the following decay chain:

$$B^0/\bar{B}^0 \rightarrow J/\Psi K_s^0 \rightarrow l^+l^-\pi^+\pi^-.$$

This decay allows a very powerful means to access the β angle of the unitarity triangle shown in figure 1.1 both from experimental and theoretical point of view, earning it the name "Golden Decay".

It should be noted that for the measurement of CP violation in the Golden Decay the interference of decay amplitudes is necessary since the probability P for a certain transition is proportional to the squared absolute value of the corresponding amplitude: $P_i \propto |A|^2$. If only one Amplitude would occur instead of a sum, the complex phase would be lost for the measurement. In case of the Golden Decay, interference occurs due to the possible mixing of $B^0/\bar{B}^0$ before decaying into the same final state.

The angle β can be determined by the measurement of the time dependent asymmetry A_{CP} of the decay rates for $B^0/\bar{B}^0$ decaying into the same final state:

$$A_{CP}(t) = \frac{\Gamma\left(B^0 \rightarrow J/\Psi K_s^0\right) - \Gamma\left(\bar{B}^0 \rightarrow J/\Psi K_s^0\right)}{\Gamma\left(B^0 \rightarrow J/\Psi K_s^0\right) + \Gamma\left(\bar{B}^0 \rightarrow J/\Psi K_s^0\right)} = \sin(2\beta)\sin(xt). \quad (1.5)$$

x denotes the mixing parameter between B^0 and $\bar{B}^0$ and is a measure for the oscillation frequency between the states. A measurement of a non zero β angle would be the evidence for CP violation in the B^0 meson system.

In order to distinguish whether a B^0 or a $\bar{B}^0$ has decayed into $J/\Psi K_s^0$, the decay of the second produced B meson from the original $b\bar{b}$ quark pair must be detected. Figure 1.3 shows a typical Golden Decay chain for the HERA-B detector with indicated average energies and flight paths. In the example, the charge of the decay lepton or kaon of the second produced B meson will reveal the identity of the B meson in the Golden Decay (the so called "tagging").

At HERA-B, 920 GeV/c protons interact with the nucleons of up to eight target wires (corresponding to a centre of mass energy of $\sqrt{s} = 41.57\ GeV$) and produce a rate of about 10^{-6} $b\bar{b}$ quarks per interaction[1]. Taking also into account the following branching fractions [Gro00] for the Golden Decay as shown in figure 1.3 and the probability $P_{b\rightarrow B^0}$ to produce a B^0 ($\bar{B}^0$) from a $\bar{b}$ (b) quark:

[1] Assuming a $\sigma_{b\bar{b}}$ of 12 nb, see [HB95].

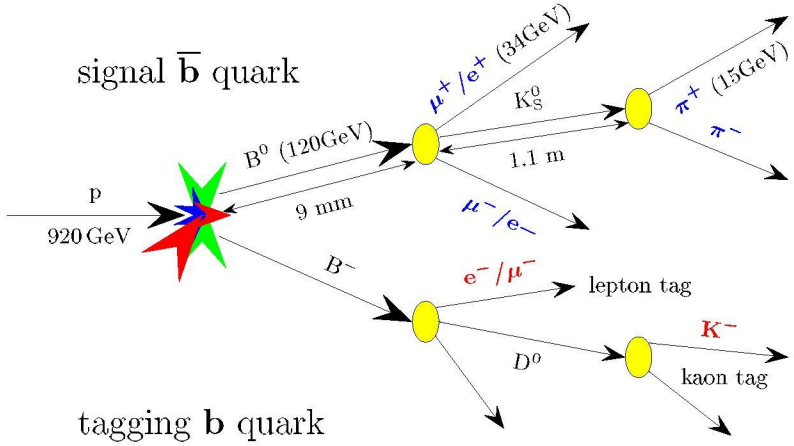

Figure 1.3: The golden decay $B^0 \to J/\Psi K^0_s$.

- $2P_{b\to B^0} \approx 0.8$,
- $\mathrm{Br}(B^0/\bar{B}^0 \to J/\Psi K^0_s) \approx 0.5 \cdot 8.9 \cdot 10^{-4}$,
- $\mathrm{Br}(J/\Psi \to e^+e^-/\mu^+\mu^-) \approx 0.12$,
- $\mathrm{Br}(K^0_s \to \pi^+\pi^-) \approx 0.69$,

one yields a rate for golden decays of about $2.9 \cdot 10^{-11}$ per interaction. In order to get sufficient statistics, HERA-B was designed to operate with four interactions on average distributed over the target wires per 100 ns bunch crossing corresponding to an interaction rate of 40 MHz. Thus, in a year of operation ($\approx 10^7 s$) one yields about 11600 golden decays to be detected. Assuming a detection efficiency of roughly 10 % and a tagging power of 30 %, several years of data taking would be needed for a competitive CP violation measurement: For a precision of $\Delta \sin(2\beta) \approx 0.1$, $\mathcal{O}(1000)$ *reconstructed and tagged* $J/\Psi K^0_s$ would be needed [HB94].

The high interaction rate necessary to fight against the hadronic background leads to particle fluxes inside HERA-B as they are expected for LHC: $(30\ MHz \cdot cm^2)/r^2$ minimum ionising particles per cm^2 with r being the distance to the beam. The consequent demands on the detector with respect to radiation hardness and trigger efficiency made more R&D necessary than originally anticipated. By now, HERA-B will not be able to measure $\sin(2\beta)$ competitive to the measurements already performed by BaBar and Belle. The results of Belle and BaBar have already established CP violation in the

B^0 system. The latest preliminary result from BaBar using about 62 million $\Upsilon(4S) \rightarrow B\bar{B}$ decays collected between 1999 and 2001 gives as result [Aub02]:

$$\sin(2\beta) = 0.75 \pm 0.09\ (stat) \pm 0.04\ (syst).$$

The struggle for measurements of angles and sides of the unitarity triangle will continue until a conclusive picture has been reached to answer the question if the Standard Model is self-consistent and able to explain all observations or not. The next generation experiments for precise measurements of CP violation and rare decays like LHCb [Ama98] are already being built.

1.3 Experimental observations of hyperon polarisation

In the middle of the 1970's it was discovered that Λ hyperons created in the interaction of an unpolarised proton beam with unpolarised target nuclei were spin polarised transverse to the production plane [Bun76]. This was completely unexpected since the theoretical expectation was that spin effects should diminish and finally disappear at high energies. The reasoning went as follows: For a significant polarisation effect[2] the coherent interference between at least two large amplitudes is necessary. This gets more and more unlikely towards higher energies due to the increasing multiplicity of final states [Hel90].

In contradiction to this, the experimental observation shows that spin effects play an important role in high energy particle physics and the existence of polarisation in hyperon production can be used to learn more about the strong interaction. The correct description of spin effects has become a critical test to any dynamical theory of hadronic phenomena [Bro81].

By now, this polarisation effect of inclusively produced Λ hyperons has been confirmed by many different experiments in a proton energy range from 12 GeV at KEK [Abe86] to the equivalent of 2000 GeV at the ISR [Erh79] on a fixed target. Additionally, also for the other hyperons in the baryon octet shown in figure 1.4 polarisation effects have been observed (Ξ^- : [Tro89], Ξ^0 : [Hel83], Σ^- : [Wah85], Σ^0 : [Duk87] , Σ^+ : [Wil87]). The found polarisations follow roughly the scheme (see e.g. [Hel85, Wil87] for a more detailed discussion):

$$P(\Lambda) \approx P(\Xi^-) \approx P(\Xi^0) \approx -P(\Sigma^-) \approx -P(\Sigma^0) \approx -P(\Sigma^+).$$

[2] That is, if the expectation value of the projection of the spin $\vec{\sigma}$ onto a direction vector $\vec{n}$ is non-zero: $< \vec{\sigma} \cdot \vec{n} > \neq 0$.

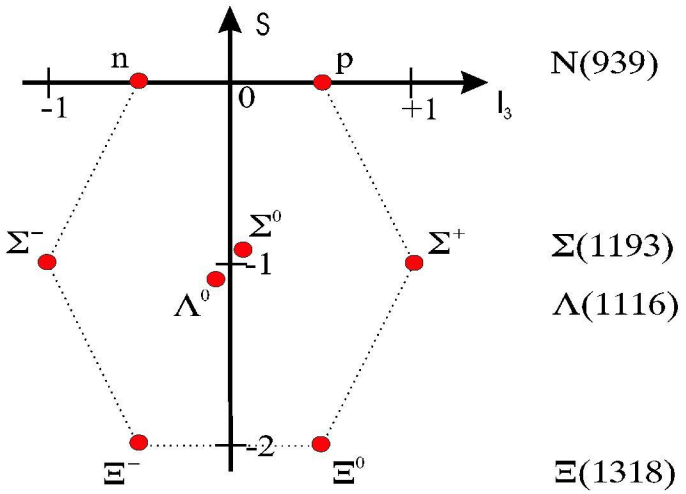

Figure 1.4: The spin-parity $J^P = \frac{1}{2}^+$ baryon octet. Strangeness S is drawn versus the third component of isospin I_3.

Obviously, hyperon polarisation is "one of the most universal regularities observed in the strong interactions" [Lun89]. The usual kinematical variables used to study the polarisation effects are:

- p_t: Transverse component of the total momentum of the hyperon relative to the proton beam direction.
- x_F: Feynman x of the hyperon: $x_F = \frac{p_l}{p_l(max)} \approx \frac{2 \cdot p_l}{\sqrt{s}}$, with p_l being the longitudinal momentum relative to the proton beam direction in the centre of mass system.

The most extensive studies so far have been performed on Λ hyperons inclusively produced in reactions of the type

$$pA \rightarrow \Lambda X.$$

The experimental signature found in those reactions can be summarised as follows [Hel85, Mag95]:

- The Λ hyperons are polarised transverse to the production plane along $-(\vec{p}_{beam} \times \vec{p}_\Lambda)$ while the polarisation of $\bar{\Lambda}$ hyperons is compatible with 0, see figure 1.5.
- The magnitude of the polarisation increases linearly with the Λ p_t , see figures 1.5 and 1.6 (a).

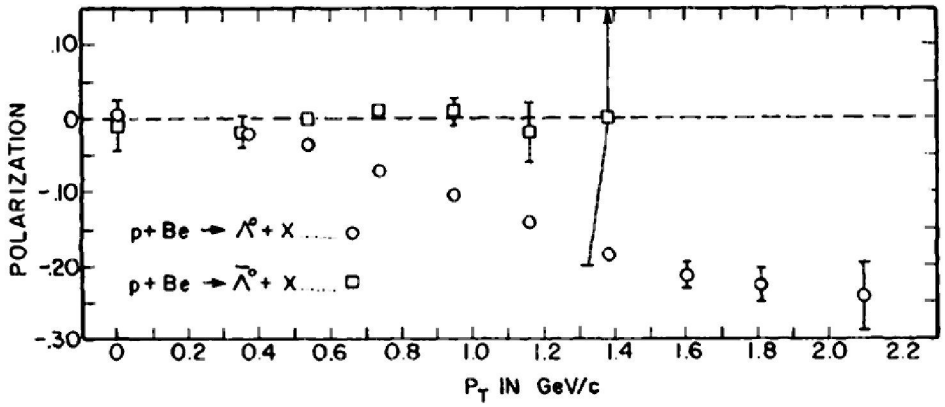

Figure 1.5: Polarisation of Λ and $\bar{\Lambda}$ in $p + Be \rightarrow \Lambda/\bar{\Lambda} + X$ with 400 GeV protons. The figure is taken from [Hel78].

- The magnitude of the polarisation grows linearly with the Λ x_F, see figure 1.6 (b).
- If any, there is only a very weak energy dependence. For a comparison between 12 GeV and 400 GeV see figure 1.7.
- The dependence of Λ polarisation on the target mass is found to be small. For targets with larger A, the magnitude of the polarisation decreases as expected due to rescattering processes inside the nucleus. The effect is on the level of a few percent [Hel85].

More detailed reviews on hyperon polarisation and references to many related experiments can be found in [Hel85], [Pon85] and [Lac91].

Many theories have so far been developed trying to describe the observed effects. In the beginning, the observations of polarised Λs and unpolarised $\bar{\Lambda}s$ supported the idea that polarisation is a leading particle effect since for the Λ only one valence quark (the s quark) needs to be produced, whereas for the $\bar{\Lambda}$ all three anti-quarks have to be created. However, later measurements of antihyperon polarisation destroyed this simple picture: The $\bar{\Xi}^+$ was found to be polarised with approximately the same magnitude than the Ξ^- [Ho90], and the $\bar{\Sigma}^-$ polarisation was measured to have the same sign but smaller magnitude than the Σ^+ [Mor93]. To date, there is still no conclusive theory available that is able to describe all the observed polarisation effects. The most common approaches will be sketched in the next section, but still more experimental information is needed to test and develop the theories.

HERA-B can contribute to this polarisation puzzle due to the unique kinematical range it covers: As shown in figure 1.6, inclusive measurements

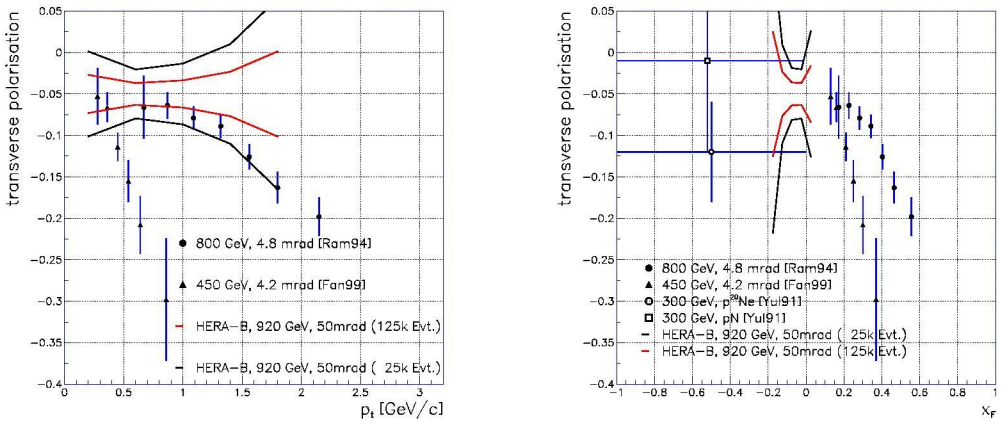

(a) (b)

Figure 1.6: Dependency of the Λ polarisation on (a) p_t and (b) x_F. The used references are indicated in the legend. The extrapolated runs of the statistical errors on an assumed polarisation value of -5 % are shown for HERA-B data samples containing 25000 and 125000 Λ hyperons respectively.

are only abundant in the high positive x_F range, whereas the negative region is almost uncovered except for some bubble chamber measurements. As indicated in the picture, HERA-B can provide measurements of Λ polarisation especially in the transition area between beam and target fragmentation region, where theories did not have experimental input so far. Provided a high statistics data set, also polarisation measurements for other hyperons will be possible. Additionally, A dependencies of the polarisation can be easily measured with HERA-B due to the different available target materials (in 2002: C, Al, Ti, Pd, W).

1.4 Models of hyperon polarisation

Although the effect of hyperon polarisation in pA collisions as described in section 1.3 is now known for more than 25 years, there is still no theoretical description which is able to explain properly all experimental observations.

This section will introduce some of the theoretical models which have been developed so far. A more extensive description of respective theories can be found in [Fel99] and references therein.

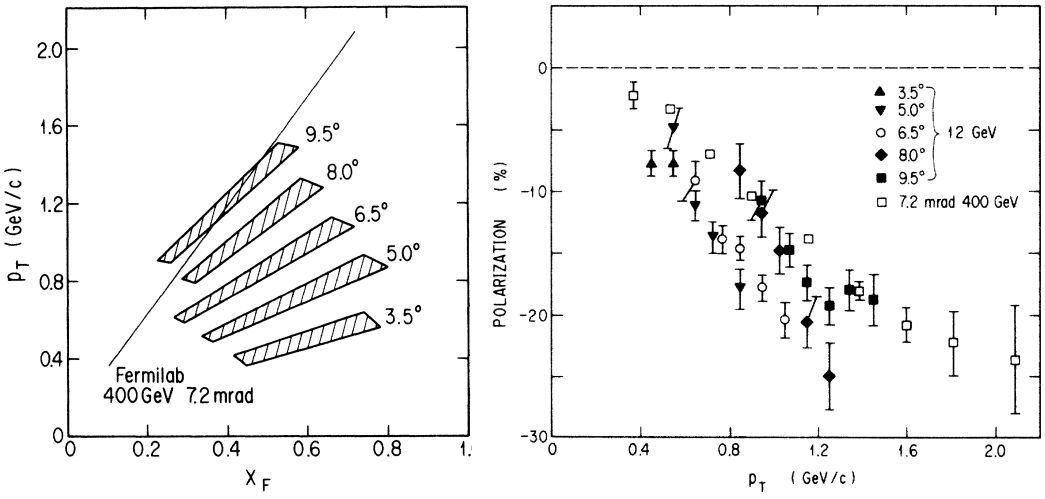

(a) (b)

Figure 1.7: Comparison of Λ polarisation measurements at different energies: (a) shows the kinematic regions covered by the data presented in [Abe86] as hatched areas and the data of [Hel78] as a straight line. The results of the respective polarisation analysis are shown in (b). Both figures have been taken from [Abe86].

Many models are motivated from the SU(6) valence quark model of the Λ, where it is formed out of an ud-diquark in a spin singlet state coming from the incident proton and one s quark which then gives the Λ p_t, spin and polarisation. The main difference between those models is then the way the s quark is produced (e.g. gluon bremsstrahlung or from the proton sea) and how its polarisation is introduced. Also, depending on the time when the theory was developed, some models do not take into account the full experimental knowledge of hyperon polarisation we have so far. For example, models like those from Heller or DeGrand and Miettinen do not reflect the polarisation dependency on x_F. Nevertheless, they will be presented because they draw a vivid picture of the possible polarisation process and illustrate the variety of available models.

It has to be noted that a theory describing all experimental information about hyperon polarisation is still not at hand, let alone the polarising phenomenology itself is established [Fel02].

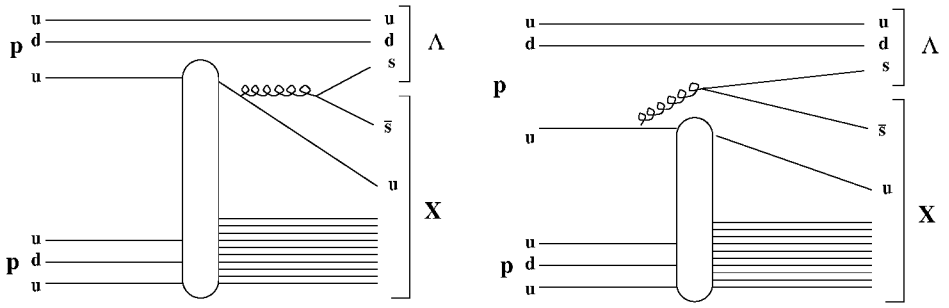

Figure 1.8: The gluon bremsstrahlung mechanism in Λ production as described by the Heller model.

1.4.1 The Heller model

This is the earliest model that tried to describe the experimental observations [Hel78]. It is reasoned that since polarisation requires coherence between at least two amplitudes and the number of contributing amplitudes should be small to yield a sizeable polarisation in an inclusive reaction, the simplest quark model should provide an appropriate description of the process. The simplest model to describe the Λ and its spin is the SU(6) quark model, where the Λ consists of an u, d and a s valence quark.

The Λ is assumed to be formed by an ud-diquark in a spin singlet state from the incoming proton as spectator and a s quark that is generated by a gluon bremsstrahlung process as indicated in figure 1.8:

During the collision a gluon is emitted from the second u quark of the proton scattered by the target yielding a $s\bar{s}$ pair. Since the s quark will provide the Λ transverse momentum and its spin, Λ polarisation would occur if the gluon and thus the $s\bar{s}$ pair is polarised, creating also the desired correlation between polarisation and transverse momentum.

In contrast to this, in order to generate a $\bar{\Lambda}$, additionally the $\bar{u}, \bar{d}$ quarks have to be produced that can contribute to the transverse momentum of the $\bar{\Lambda}$, but not to the polarisation. Thus, for a given value of transverse momentum, the polarisation would be suppressed compared to the Λ which is in agreement with the observed data.

The model also predicts the polarisations of other hyperons via the SU(6) quark wave functions in terms of the Λ polarisation P_Λ, assuming that all $q\bar{q}$ pairs are produced with the same polarisation, for example: $P_{\Sigma^0} = -\frac{1}{3}P_\Lambda$ and $P_{\Sigma^+} = \frac{1}{3}P_\Lambda$.

Taking into account the last consideration, the vanishing polarisation for the $\bar{\Lambda}$ seems not to be smoothly embedded in this theory any more: If the

assumption that all $q\bar{q}$ pairs are produced with the same polarisation is used to predict the polarisation of other hyperons, why should the respective anti-quarks in return *not* contribute to a polarisation of the $\bar{\Lambda}$?

An extension of this model thus is stated in [Fel99]: Assuming by symmetry arguments that the s and the $\bar{s}$ quark are produced with equal and opposite polarisation, one would expect also equal but opposite polarisations of Λ and $\bar{\Lambda}$ when produced simultaneously in pp reactions.

Looking at the prediction that the polarisation of the Σ^+ should have the same sign than the Λ polarisation, this is already proven to be wrong by the measurement of Σ^+ polarisation to be positive [Wil87].

1.4.2 The DeGrand and Miettinen model

This model ([DeG81a],[DeG81b]) works in the parton recombination framework, using like Heller SU(6) quark wave functions to relate various hyperon polarisations to each other. The proposed relations allow to test the recombination picture without stating the underlying dynamical origin of the polarisation on the quark level which is then additionally proposed to be a Thomas precession effect in the recombination of the quarks.

The production of hyperons is classified with respect to common (fast) valence quarks (V) in the fragmenting and produced secondary particle. All quarks not available as valence quarks in the fragmenting particle have to be retrieved from (slow) sea quarks (S) that are assumed to be initially *unpolarised*. For example, the Λ production is referred to as VVS recombination, and $\bar{\Lambda}$ production corresponds to SSS recombination.

All hyperons shown in figure 1.4 are treated as bound states of a diquark and a quark, produced either via VVS or VSS recombination. The baryon production can then be described via two amplitudes for the single quark, $A_\uparrow$ and $A_\downarrow$, which parametrise the recombination with spin up or down with respect to the scattering plane and four amplitudes $A_{j,m}$ that parametrise the recombination of the diquark in one of the states j=0, m=0 or j=1, m=$\pm$1,0. The total amplitude to produce a baryon B' in the spin state s' from a baryon B in spin state s is then given by:

$$< B'_{s'}|B_s >= \sum_{j=0,1} \left(\alpha_j A_\uparrow A_{j,s'-\frac{1}{2}} + \beta_j A_\downarrow A_{j,s'+\frac{1}{2}} \right)$$

with α and β being Clebsch-Gordan coefficients.

From this, the polarisation of the Λ in the transition p$\rightarrow\Lambda$ can be obtained, taking into account j=0 for the ud-diquark in the Λ:

$$P(p \rightarrow \Lambda) = \frac{|A_\uparrow|^2 - |A_\downarrow|^2}{|A_\uparrow|^2 + |A_\downarrow|^2}.$$

Parametrising the data by setting $|A_\uparrow|^2 = A(1-\epsilon)$ and $|A_\downarrow|^2 = A(1+\epsilon)$, assuming a small ϵ that is linear in p_t, we get

$$P(p \to \Lambda) = -\epsilon.$$

Similarly, in case of the Σ^+ the amplitudes for the diquark recombinations into the j=1 state are parametrised: A small asymmetry δ of the *opposite* sign compared to the single quark recombination amplitude is introduced:

$$\begin{aligned} |A_{0,0}|^2 &= B \\ |A_{1,1}|^2 &= B(1+\delta) \\ |A_{1,0}|^2 &= B \\ |A_{1,-1}|^2 &= B(1-\delta). \end{aligned}$$

From this, the polarisation of the Σ^+ in the transition p$\to \Sigma^+$ yields:

$$P(p \to \Sigma^+) = \frac{1}{3}\epsilon + \frac{2}{3}\delta,$$

which corresponds to the experimental observations if $\epsilon = \delta$.

Regarding the signs in front of the introduced asymmetries ϵ and δ, taking into account that for both Λ and Σ^+ VVS recombination occurs with a fast valence diquark and a slow single quark from the sea, the following rule is phrased (see [DeG81b]):

> "Slow partons preferentially recombine with their spins down in the scattering plane while fast partons recombine with their spins up."

As a crosscheck, the polarisation for Ξ^0/Ξ^- is derived *with flipped signs* in front of ϵ and δ, since in this case VSS recombination occurs, yielding:

$$P(p \to \Xi^0) = P(p \to \Xi^-) = -\frac{1}{3}\epsilon - \frac{2}{3}\delta.$$

This again corresponds to the observations if $\epsilon = \delta$. Several more relations can be found in [DeG81b].

The semiclassical model presented for the origin of the polarisation is based on Thomas precession[3] effects on the quarks' spins being affected by the confining force as illustrated in figure 1.9 in an example for the Λ:

Since the s quark in the sea of the proton will carry some transverse momentum but less longitudinal momentum than it will have as valence

[3]Thomas precession can be understood as a relativistic kinematic effect resulting from the fact that the product of non-collinear boosts is equivalent to a boost *and* a rotation.

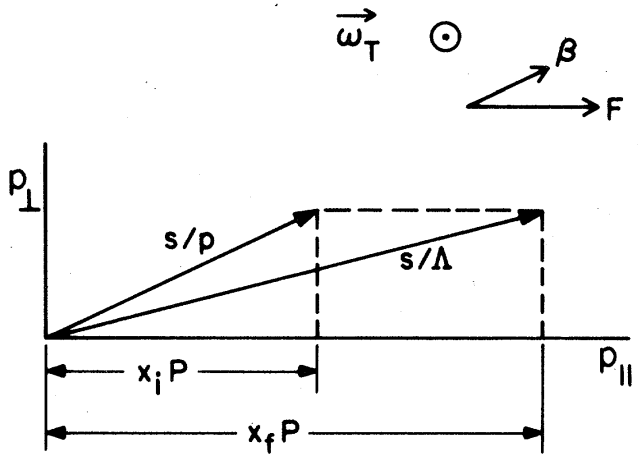

Figure 1.9: The Thomas precession effect: The momentum vectors of the s quark in the proton (s/p) and in the Λ (s/Λ) are shown. The transverse momentum component is conserved while the longitudinal component is boosted. $\vec{\omega}_T \propto$ confining force $\vec{F}\times$ the s quark's velocity $\vec{\beta}$ points out of the paper. The figure is taken from [DeG81b].

quark in the Λ, its velocity vector $\vec{\beta}$ will not be parallel to the confining force $\vec{F}$. Thus, the quark will experience a Thomas precession, leading to an effective interaction $U = \vec{s} \cdot \vec{\omega}_T$, where $\vec{\omega}_T \propto \vec{F} \times \vec{\beta}$ is the Thomas frequency vector having the direction of the normal to the scattering plane $\vec{p}_{beam} \times \vec{p}_\Lambda$ and $\vec{s}$ is the spin vector of the s quark.

The amplitude for Λ production A_Λ will be inversely proportional to the energy difference between initial state (where we have an ud-diquark and a strange quark) and the final state (where the Λ has been formed):

$$A_\Lambda \propto \frac{1}{\Delta E_0 + U}$$

with $\Delta E_0 = E_{diquark} + E_s - E_\Lambda$ being the energy difference in absence of spin effects and U the Thomas precession term stated above. Consequently, the Λ production is enhanced if $\vec{s} \cdot \vec{\omega}_T$ is negative corresponding to the s quark having its spin down with respect to the normal on the production plane, as actually observed. The opposite sign of asymmetry stated in the recombination rule above for the fast partons immediately follows from the fact that the fast V partons have to be *de*celerated in the recombination process, yielding the opposite direction of $\vec{\omega}_T$ compared to the slow sea quarks.

The p_t dependency of the polarisation also directly follows from this model: If we choose the quantisation axis along the normal of the production

plane, we obtain the following amplitudes for Λ production with spin up and spin down:

$$A_\uparrow \propto \frac{1}{\Delta E_0 + \frac{1}{2}\omega_T}, \quad A_\downarrow \propto \frac{1}{\Delta E_0 - \frac{1}{2}\omega_T}.$$

Calculating from this the polarisation asymmetry, one gets in leading order of ω_T:

$$P(p \to \Lambda) = -\frac{\omega_T}{\Delta E_0}.$$

Because ω_T will increase with p_t, also the polarisation will.

The production of antihyperons according to this model has to be unpolarised: Since antihyperons are produced via SSS recombination, there will be as many configurations with the single quark being faster than the diquark than vice versa. Hence, on average ω_T will be zero and the polarisation will vanish.

The last statement experimentally holds for $\bar{\Lambda}$ production, but stands in contradiction to the observations of $\bar{\Xi}^+$ and $\bar{\Sigma}^-$ polarisation.

1.4.3 The Lund model

The Lund model by Andersson et al. [And79] is a semiclassical string fragmentation model for Λ polarisation where the process introducing the polarisation is soft, making perturbative QCD not applicable.

Like in previous models, the beam proton provides an ud-diquark in spin singlet state to form the Λ. When the diquark is propagating away from the central collision region with momentum $\vec{q}$ and transverse momentum $\vec{q}_t$, a colour field is stretched in-between. This colour field is assumed to be spacially confined in a one dimensional flux tube without any transverse degrees of freedom. A Λ is produced, if the flux tube breaks up by the production of a $s\bar{s}$ pair, where again the s quark will determine the spin of the Λ.

As illustrated in figure 1.10, to conserve locally the transverse momentum, the $s\bar{s}$ pair is produced with equal but opposite transverse momenta $\vec{k}_t$ and $-\vec{k}_t$ relative to the string. Because of the quark mass, the quark pair has to be produced with a finite distance to each other, resulting in an orbital angular momentum along the direction $\vec{m} = (\vec{q} \times \vec{k}_t)/|\vec{q} \times \vec{k}_t|$ perpendicular to the production plane, which has to be compensated by the spin of the quark-antiquark pair.

In this model, polarisation arises from a "trigger bias" effect: If the Λ polarisation is measured versus p_t, with increasing p_t the probability to find $\vec{k}_t$ aligned with $\vec{q}_t$ and thus to have a preferred spin direction is increasing, since

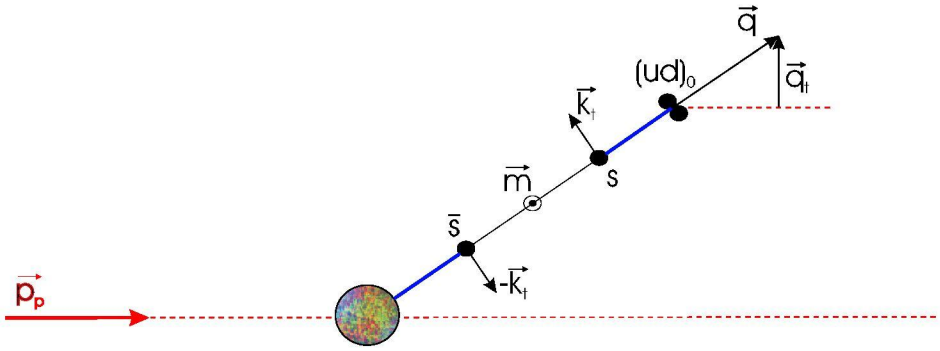

Figure 1.10: String fragmentation in the Lund model: A $s\bar{s}$ pair is produced in the breaking up of the colour force field between the scattered diquark and the central collision zone. The transverse momenta of the s quarks generate an angular momentum along $\vec{m}$, in this case pointing out of the paper, to be balanced by their spin.

the probability for the production of a diquark is decreasing with increasing q_t.

The proposed polarisation mechanism has one interesting implication for $\bar{\Lambda}$ polarisation: in this model, Λ and $\bar{\Lambda}$ must have equal polarisation if they are produced associated, in contradiction to both previous models. Polarisations for Σ^0 and Ξ^0 are predicted with the right signs. The polarisation of "indirect" Λs originating from a Σ^0 decay is estimated to be roughly $\frac{1}{9}$ of the polarisation of directly produced Λs.

A comparison between data and the predictions of this model shown in [Fel99] illustrates the disagreement between model and Λ data. A polarisation dependence on x_F is not included in the model.

1.4.4 The Hadronisation model

One recent model by Anselmino et al. [Ans01a] is based on perturbative QCD using so called "polarising fragmentation functions":

The Λ polarisation P_Λ can be expressed by the following asymmetry:

$$P_\Lambda = \frac{d\sigma^{AB\to\Lambda^\uparrow X} - d\sigma^{AB\to\Lambda^\downarrow X}}{d\sigma^{AB\to\Lambda^\uparrow X} + d\sigma^{AB\to\Lambda^\downarrow X}}.$$

In "hard" processes with sufficiently high energy, where the fast moving hadron can be described as a jet of quasi free collinearly moving partons, the process $AB \to \Lambda^\uparrow X$ at leading twist can be described as follows according

to a QCD factorisation theorem:

$$d\sigma^{AB\to\Lambda^\uparrow X} = \sum_{a,b,c,d} f_{a/A}(x_a) \otimes f_{b/B}(x_b) \otimes d\hat{\sigma}^{ab\to cd} \otimes D_{\Lambda^\uparrow/c}(z).$$

In the above expression $f_{a/A}(x_a)$ and $f_{b/B}(x_b)$ denote the unpolarised parton densities depending on the longitudinal momentum fraction x_a, x_b inside an unpolarised hadron A, B. $d\hat{\sigma}^{ab\to cd}$ is the partonic cross-section for the process $ab \to cd$, and $D_{\Lambda^\uparrow/c}(z)$ denominates the fragmentation function for the process $c \to \Lambda^\uparrow + X$, where the Λ is produced with longitudinal momentum fraction z. The sum $\sum_{a,b,c,d}$ finally takes into account all possible elementary interactions.

In the absence of intrinsic transverse momentum between hyperon and fragmenting quark $\vec{k}_t$ (or when $\vec{k}_t$ is integrated over), the fragmentation function $D_{\Lambda^\uparrow/c}(z)$ or also $D_{\Lambda^\downarrow/c}(z)$ cannot depend on the hyperon polarisation to conserve rotational invariance. Consequently, we get $d\sigma^{AB\to\Lambda^\uparrow X} = d\sigma^{AB\to\Lambda^\downarrow X}$ and hence $P_\Lambda = 0$.

The main idea of Anselmino et al. is to use new polarising fragmentation functions to describe the hadronisation process of an unpolarised quark into a transversely polarised hyperon. This new function type takes into account intrinsic $\vec{k}_t$ in the hadronisation process. Assuming that the factorisation theorem still holds also when $\vec{k}_t$ is included[4], the usual, $\vec{k}_t$ integrated unpolarised fragmentation functions $D_{\Lambda/c}(z)$ are replaced[5] by:

$$\begin{aligned}\Delta^N D_{h\uparrow/a}(z,\vec{k}_t) &\equiv \hat{D}_{h\uparrow/a}(z,\vec{k}_t) - \hat{D}_{h\downarrow/a}(z,\vec{k}_t) \\ &= \hat{D}_{h\uparrow/a}(z,\vec{k}_t) - \hat{D}_{h\uparrow/a}(z,-\vec{k}_t).\end{aligned}$$

The polarising fragmentation function denotes the difference between the density numbers $\hat{D}_{h\uparrow/a}(z,\vec{k}_t)$ and $\hat{D}_{h\downarrow/a}(z,\vec{k}_t)$ of hadrons h with spin $\frac{1}{2}$, momentum $\vec{p}_h = z\vec{p}_a + \vec{k}_t$, and transverse polarisation $\uparrow$ or $\downarrow$ inside a jet originated from the fragmentation of an unpolarised parton a.

The main features of this function are:

- It vanishes if the transverse momentum $\vec{k}_t$ of the hyperon with respect to the fragmenting quark direction is zero.
- The fragmentation function can be viewed as effectively including the contamination due to Σ^0s.

[4]The partons a and b inside the the unpolarised hadrons A and B are still assumed to be collinear; transverse motion is only considered in the fragmentation process.

[5]The distribution functions f are still assumed to be spin and $\vec{k}_t$ independent.

- Due to parity conservation in the hadronisation process, only $\vec{k}_t$ components perpendicular to the polarisation direction, i.e. lying in the production plane, can contribute to the fragmentation function.
- Applying charge conjugation invariance to obtain $\bar{q} \to \bar{\Lambda}$ fragmentation properties from the $q \to \Lambda$ process, we get $\Delta^N D_{\bar{\Lambda}\uparrow/\bar{q}} = \Delta^N D_{\Lambda\uparrow/q}$.
- The polarising fragmentation function is assumed to be non-vanishing only for Λ and $\bar{\Lambda}$ valence quarks u, d, s and $\bar{u}$, $\bar{d}$, $\bar{s}$.

A simple parametrisation of the polarising fragmentation function containing seven free parameters is finally used to fit some available data on $\Lambda/\bar{\Lambda}$ polarisation produced in p-p and p-Be collisions. For the evaluation of the cross section for scattering off a nucleus with A nucleons and Z protons, a simple incoherent sum is used, neglecting nuclear effects:

$$d\sigma^{AB\to\Lambda X} = Z d\sigma^{pp\to\Lambda X} + (A - Z) d\sigma^{pn\to\Lambda X}.$$

The agreement of the model with the Λ and $\bar{\Lambda}$ data is good, exhibiting the expected behaviour in x_f and p_t. This shows a description of Λ polarisation in unpolarised hadronic reactions is in principle feasible using perturbative QCD to factorise the elementary dynamics and non-perturbative spin and $\vec{k}_t$ dependent fragmentation functions. As shown in figure 1.11, these functions are sizable with respect to the unpolarised fragmentation functions only in a limited z range.

However, this model is only applicable in the appropriate kinematical regions, where perturbative QCD can be used. As an example, for the x_F range of HERA-B, data with $p_t > 4\ GeV/c$ would be needed in order to be able to compare with predictions of this model [Ans01b] which seems unreachable looking at the respective distributions shown in appendix A. Additionally, it would be interesting to see the predictions of this model for the polarisations of the other (anti-) hyperons in the baryon octet.

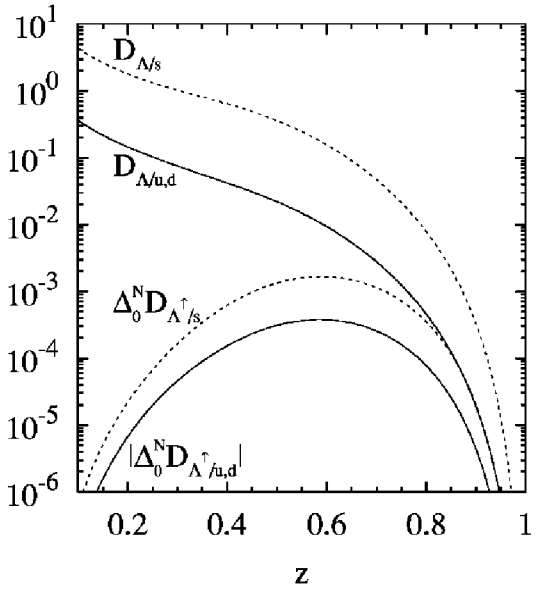

Figure 1.11: Comparison of polarising and unpolarised fragmentation functions versus longitudinal momentum fraction z. The figure has been taken from [Ans01a].

1.5 Theory of the weak Λ decay

The analysis of Λ polarisation is possible via the parity violation in its weak decay:

In the weak decay $\Lambda \to N\pi$ the $J^P = \frac{1}{2}^+\Lambda$ decays into a $J^P = \frac{1}{2}^+$ nucleon N and a $J^P = 0^-$ pion. To conserve the total angular momentum, only decays with the relative angular momentum l between nucleon and pion of 0 and 1 are allowed.

If parity would be conserved, only the decay with nucleon and pion in a relative p-wave would be possible ($P = (-1)^l$). Since the weak interaction violates parity, additionally the s-wave is allowed in the above decay.

The following derivation is based on [Per82]. To study the angular distributions (ϑ, Φ) of the Λ decay products, we move into the Λ rest frame where we define the direction of the z-axis to point along the Λ spin $\vec{\sigma}$ (see figure 1.12).

In this coordinate system, we have $J_\Lambda = \frac{1}{2}$ and $J_{z,\Lambda} = +\frac{1}{2}$. If we define m_p to be the z-component of the proton spin vector and m_l as the z-component of the angular momentum vector $\vec{l}$, we obtain as total wave function for the s-wave (since $l = m_l = 0$):

$$\Psi_s = a_s Y_0^0 \chi^+, \tag{1.6}$$

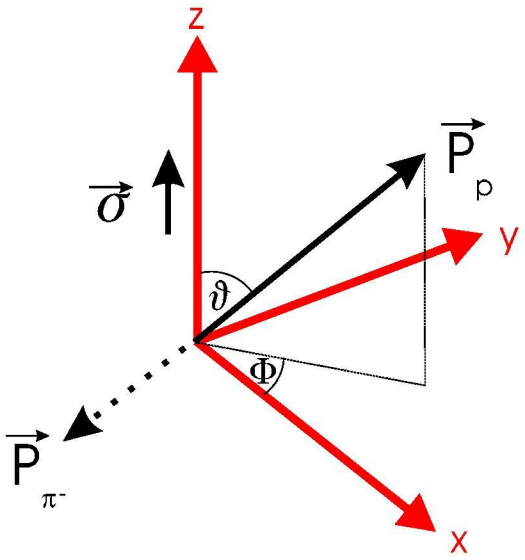

Figure 1.12: The Λ coordinate system in the Λ rest frame with Λ spin and momentum vectors of the decay products.

where a_s is the amplitude of the s-wave and χ^+ denotes the proton state with $m_p = +\frac{1}{2}$ ("spin-up"). In this case, the proton spin and the Λ spin are parallel. In the p-wave case, the equation $m_p + m_l = J_{z,\Lambda}$ can be fulfilled by having either $m_p = +\frac{1}{2}$ and $m_l = 0$ or $m_p = -\frac{1}{2}$ and $m_l = 1$. Taking into account the Clebsch-Gordan coefficients for the addition $1 \otimes \frac{1}{2}$ to $J_\Lambda = \frac{1}{2}$ and $J_{z,\Lambda} = +\frac{1}{2}$, one yields:

$$\Psi_p = a_p \left(\sqrt{\frac{2}{3}} Y_1^1 \chi^- - \sqrt{\frac{1}{3}} Y_1^0 \chi^+ \right), \tag{1.7}$$

with a_p as the amplitude of the p-wave and the corresponding spherical harmonics. The total wave function Ψ is now given by the superposition of s- and p-wave:

$$\Psi = \Psi_s + \Psi_p = \left(a_s Y_0^0 - a_p \sqrt{\frac{1}{3}} Y_1^0 \right) \chi^+ + \left(a_p \sqrt{\frac{2}{3}} Y_1^1 \right) \chi^-.$$

In principle, both amplitudes a_s and a_p can be complex numbers, between which only a relative phase can be measured. Taking advantage of the orthogonality of the proton states χ^+ and χ^-, the angular distribution becomes

$$\Psi\Psi^* = |a_s|^2 \left|Y_0^0\right|^2 + \frac{1}{3} |a_p|^2 \left|Y_1^0\right|^2 + \frac{2}{3} |a_p|^2 \left|Y_1^1\right|^2 - \sqrt{\frac{1}{3}} \left(a_s a_p^* Y_0^0 Y_1^{0*} + a_s^* a_p Y_0^{0*} Y_1^0 \right).$$

Inserting the needed spherical harmonics

$$Y_0^0 = \frac{1}{\sqrt{4\pi}}, \quad Y_1^0 = \sqrt{\frac{3}{4\pi}}\,\cos\vartheta, \quad Y_1^1 = -\sqrt{\frac{3}{8\pi}}\,\sin\vartheta\; e^{i\varphi},$$

one finally gets as angular distribution $I(\cos\ \vartheta)$:

$$I(\cos\ \vartheta) \;=\; \Psi\Psi^* \;=\; \frac{1}{4\pi}\;(1\; +\alpha\;\cdot\;\cos\ \vartheta) \tag{1.8}$$

with

$$\alpha \;=\; -\;\frac{2\ Re\left(a_s a_p^*\right)}{|a_p|^2\;+\;|a_s|^2} \tag{1.9}$$

being the so-called decay asymmetry parameter. The parity violation in the Λ decay appears as up-down asymmetry of the decay proton (or pion) with respect to the production plane. Note that this asymmetry is due to the interference of the s and p wave: both amplitudes have to be finite to yield a finite α. The decay asymmetry parameter can be regarded as a measure for how much of the information about the Λ spin "survives" the decay. If we assume CP invariance, the absolute value of α for Λ and $\bar{\Lambda}$ will be identical, since just the ϑ angle will be transformed into $\pi - \vartheta$, resulting in an additional - sign in front of the cosine that can be absorbed into α. Experimentally, the decay asymmetry parameter is measured to be $\alpha = 0.642 \pm 0.013$ [Gro00].

Since the emission angle ϑ of the proton cannot be measured with respect to the Λ spin $\vec{\sigma}$ but only relative to the normal vector on the production plane, we can redefine the angular distribution as follows:

$$I(\cos\ \vartheta) \;=\; \frac{1}{4\pi}\;(1\; +\alpha\; P\;\cos\ \vartheta)\,, \tag{1.10}$$

where P denotes the average polarisation.

For a polarisation measurement, we define for every event our coordinate system of reference in the following way (see figure 1.13): The z axis points along the momentum of the produced Λ $\vec{p}_\Lambda$, the x axis is chosen as the normal on the production plane defined by the Λ and the beam momentum $\vec{p}_b$, and the y axis is selected to form a right-handed coordinate system:

$$\vec{n}_z \;=\; \frac{\vec{p}_\Lambda}{|\vec{p}_\Lambda|},\; \vec{n}_x \;=\; \frac{\vec{p}_b \times \vec{p}_\Lambda}{|\vec{p}_b \times \vec{p}_\Lambda|},\; \vec{n}_y \;=\; \vec{n}_z \times \vec{n}_x. \tag{1.11}$$

Extending the angular distribution derived before into all three coordinates and introducing $A(\cos\ \vartheta_i)$ as the acceptance of the HERA-B apparatus, the Λ

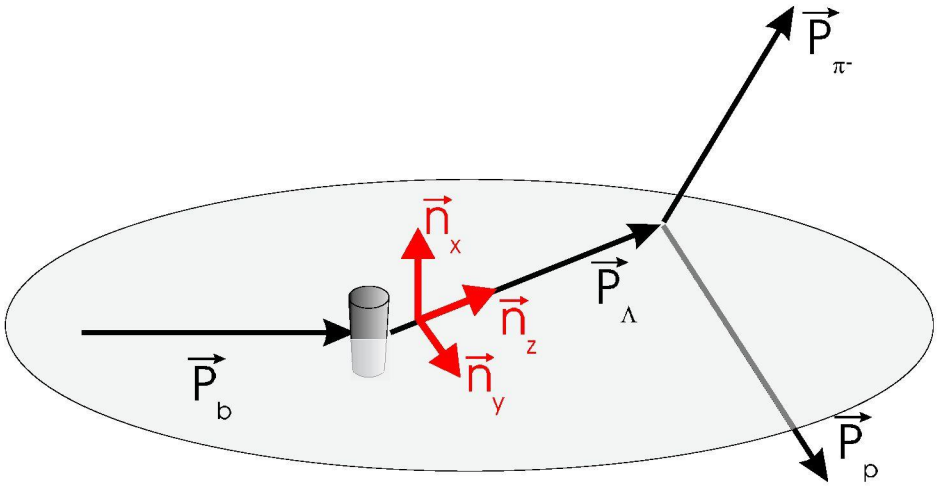

Figure 1.13: The coordinate system of reference for polarisation measurements: the momentum vectors of the proton beam and the Λ produced in the target wire define the reaction plane.

polarisation $\vec{P} = (P_x, P_y, P_z)$ can be determined by the angular distributions of the decay proton in the Λ rest frame:

$$\begin{aligned} I(\cos\ \vartheta_i) &= \frac{1}{4\pi} A(\cos\ \vartheta_i)\ (1\ + \alpha\ P_i\ \cos\ \vartheta_i) \\ &= \frac{1}{4\pi} A(\cos\ \vartheta_i)\ R\,(\cos\ \vartheta_i)\,, i = x, y, z. \end{aligned} \tag{1.12}$$

Here, $\cos\ \vartheta_i = \vec{n}_i \cdot \vec{n}_p$ with $\vec{n}_p$ being the direction vector of the decay-proton in the Λ rest frame.

As illustrated in figure 1.14, the parity conservation in the strong interaction by which the Λ particle is produced forbids any polarisation to occur in the reaction plane if the incoming proton beam is unpolarised. Thus, the only asymmetry can occur normal to the production plane which we chose as x coordinate. Since $P_y\ =\ P_z\ = 0$, the corresponding angular distributions have to be flat which can be used to crosscheck systematic errors.

The derived angular distributions can, of course, easily be obtained also for the other two "V^0" signals K^0_s and $\bar{\Lambda}$: The definition of the coordinate system of reference can obviously be rewritten in a more general way:

$$\vec{n}_z\ =\ \frac{\vec{p}_{V^0}}{|\vec{p}_{V^0}|},\ \vec{n}_x\ =\ \frac{\vec{p}_b \times \vec{p}_{V^0}}{|\vec{p}_b \times \vec{p}_{V^0}|},\ \vec{n}_y\ =\ \vec{n}_z \times \vec{n}_x, \tag{1.13}$$

with V^0 being one of the particles K^0_s, Λ or $\bar{\Lambda}$. The angular distributions can then be obtained by using the direction vector of the decay $\bar{p}$ for the $\bar{\Lambda}$ and

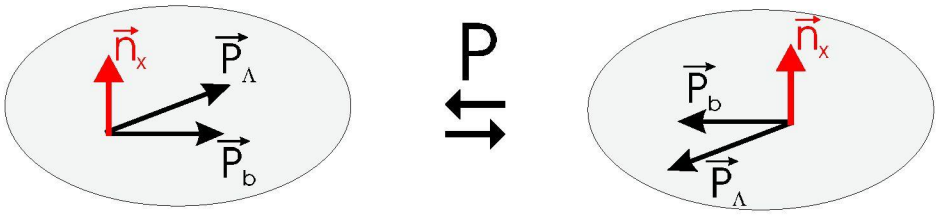

Figure 1.14: Effect of the parity operation on Λ production

the decay π^+ for the K^0_s in the respective V^0 restframe: cos $\vartheta_i = \vec{n}_i \cdot \vec{n}_{\bar{p}}$ and cos $\vartheta_i = \vec{n}_i \cdot \vec{n}_{\pi^+}$. Taking finally into account the following α parameters: $\alpha_{K^0_s} = 1$, $\alpha_\Lambda = 0.642$, $\alpha_{\bar{\Lambda}} = -0.642$, the polarisations for each V^0 can be obtained.

Of course, the "polarisation" for the K^0_s being a spinless particle has to be zero, and by setting $\alpha_{K^0_s} = 1$, "polarisation analysis" means checking the flatness of the angular distributions. Due to this and parity conservation forbidding polarisation effects to occur in the reaction plane, 7 of the 9 measurements being performed have to yield zero as the result.

Using all V^0 signals thus provides an inherent crosscheck for the consistency of the analysis to be performed.

1.6 Layout of the thesis

In this thesis, data taken during the HERA-B commissioning in the year 2000 are used to perform an analysis of transverse polarisation of Λ and $\bar{\Lambda}$ inclusively produced in pA collisions at a centre of mass energy of $\sqrt{s} = 41.57\ GeV$ in the proton nucleon system.

In chapter 2, the HERA-B apparatus with special emphasis on the components crucial for the presented analysis is introduced, before in the next chapter the used dataset and reconstruction chain is explained.

Chapter 4 illustrates the cuts and track selection criteria that were used to reconstruct the V^0 signals in the data. The determination of the detector acceptance via Monte Carlo simulations is then presented in the next chapter, which is necessary for the polarisation analysis algorithm explained in chapter 6.

The possible sources of systematic errors are investigated in chapter 7, before finally in the last chapter all obtained results are summarised and discussed, and an outlook with conclusion is given.

Chapter 2

The HERA-B spectrometer

The HERA-B detector [HB94] is a forward magnetic spectrometer which was designed to study the violation of CP symmetry in the system of neutral B mesons, especially in the golden decay $B^0/\bar{B}^0 \to J/\Psi K_s^0$. To make this measurement feasible despite the signal to background ratio of about $2.9 \cdot 10^{-11}$, HERA-B was planned to be capable to process interaction rates of 40 MHz (see section 1.2). This imposes severe requirements on radiation hardness, detector granularity, trigger performance and DAQ bandwidth. The interactions are obtained by placing up to eight target wires in the proton beam of the HERA storage ring.

The spectrometer covers the full azimuth angle and polar angles between 10 *mrad* and 250 (160) *mrad* in the bending (non-bending) plane, as shown in figure 2.1. This angular coverage corresponds to about 90 % of 4π in the centre of mass system [HB95].

The right-handed coordinate system of HERA-B which will also be used in this thesis is oriented in respect of the proton beam direction: The z-axis points into the beam direction, the horizontal x-axis points to the centre of HERA and the vertical y-axis processes from bottom to top.

In the following sections, the HERA storage ring and the individual components of the HERA-B spectrometer will be briefly described. Special focus will be put on those components which have been crucial for the analysis presented in this thesis, namely vertex detector and main tracker.

A detailed review on the detector status in the year 2000 can be found in [HB00].

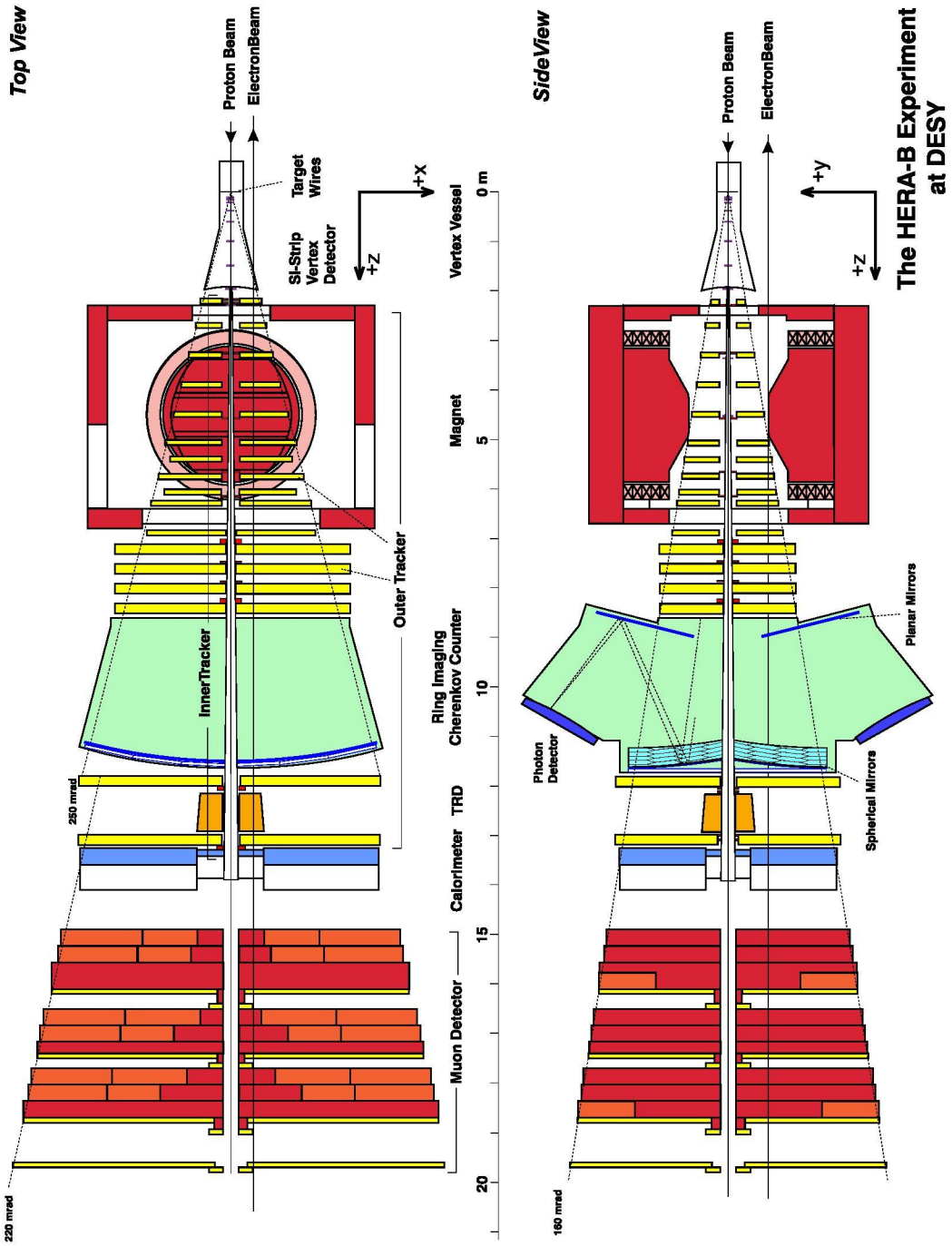

Figure 2.1: Schematic drawing of the HERA-B spectrometer with its various sub-detectors [Pyr98].

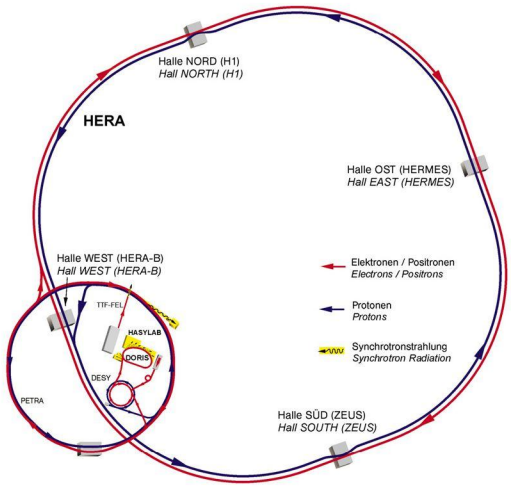

Figure 2.2: The HERA storage ring with its accelerators at DESY [DES01].

2.1 The HERA double storage ring

The HERA-B experiment is utilising the HERA ("**H**adron **E**lektron **R**ing **A**nlage") double $e^-(e^+)$-p storage ring[1] at the DESY facility in Hamburg, Germany [DES01]. The HERA ring with a circumference of 6.3 km stores protons of 920 GeV and electrons (positrons) of 27.5 GeV energy. As shown in figure 2.2, there are four experimental areas at HERA:

In the north and south areas, the experiments H1 and ZEUS investigate the internal structure of the proton by colliding the $e^-(e^+)$ beam with the proton beam. In the east, the HERMES experiment explores the internal spin structure of proton and neutron by deep inelastic scattering of the longitudinally polarised electron (positron) beam on a polarisable target. Finally, the HERA-B experiment situated in the western experimental area uses the HERA proton beam for interactions with up to eight fixed target wires.

For the proton beam, 180 out of 220 possible stable bunches of protons are filled into the HERA storage ring. These bunches have a distance of 96 ns to each other and are $\mathcal{O}(1\ ns)$ long, which means that the data acquisition of HERA-B is triggered with a frequency of approximately 10 MHz.

[1] It is possible to store electrons *or* positrons in HERA.

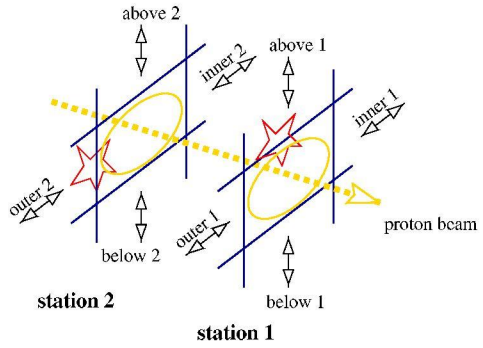

(a)

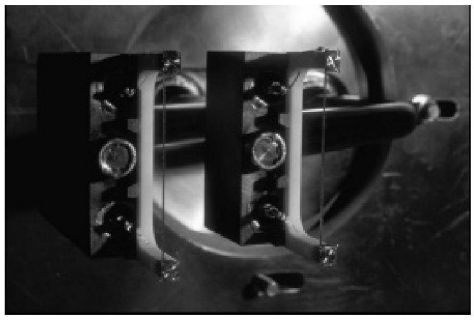

(b)

Figure 2.3: (a): The spatial configuration of the HERA-B internal target. The arrows indicate the direction of movement of the wires, their names are referring to their positions with respect to the HERA ring. (b): Two ceramic target forks with mounted wires. Figure (a) has been taken from [HB00], figure (b) from [Spr00].

2.2 The internal target

The internal target system [Ehr00] of HERA-B consists of 8 individually movable target wires enclosing the HERA proton beam. They are distributed over two stations which are separated 40 mm from each other along z (see figure 2.3).

This distance is chosen as it allows reconstruction of secondary vertices of decaying B mesons coming from target station 2 independently from vertices of station 1, since the average decay length of a B meson in HERA-B is 9 mm as shown in figure 1.3. Furthermore, the individual movement of the wires permits to distribute the needed multiple interactions uniformly over them resulting in well separated vertices.

The width of the wires is typically 50 μm transverse to and 500 μm along the beam direction; the usage of different materials also makes studies of nuclear dependencies possible. A more detailed description of the target geometry and used materials can be found in [Spr00].

Originally, it was planned to operate the target only parasitically in the beam halo [HB94], but since the lifetime of the proton beam in HERA increased over the years, the natural proton loss rate is too low to produce the desired interaction rates. Therefore the wires are now operated as "scraping targets" at 4 to 6 beam sigma[2], reducing the lifetime of the proton beam in e-p mode from a few hundred to about 50 hours [Ehr02, Fun99].

[2]The proton beam core can be regarded as Gaussian shaped with a typical width of roughly 400 μm [Ehr01].

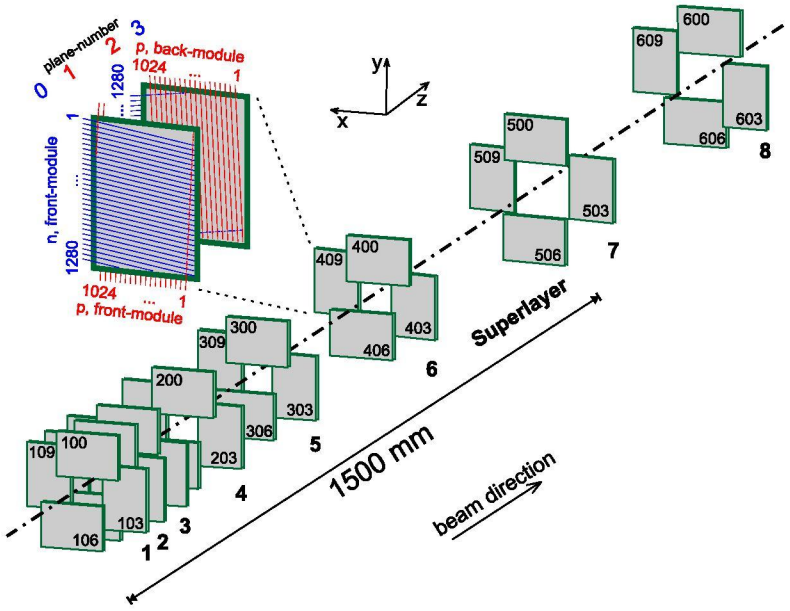

Figure 2.4: Arrangement of the double-sided silicon microstrip detectors around and along the proton beam. The figure has been taken from [Bau02].

2.3 The tracking and vertexing system

The tracks and vertex positions of the charged particles produced at the target are detected by the tracking and vertexing components of HERA-B. Together with the bending of the particle trajectories inside the magnet, momentum information can be obtained. In front of the magnet, the silicon vertex detector determines primary and secondary vertices and track-segments of the charged particles. The tracking system inside and behind the magnet is divided into an inner part (Inner Tracker, ITR) and an outer part (Outer Tracker, OTR) starting at approximately 25 *cm* distance from the beam. This partitioning is necessary to adjust granularity and expected occupancies with a minimal number of channels.

2.3.1 The Vertex Detector System (VDS)

The vertex detector system of HERA-B consists of 64 double-sided silicon microstrip detectors which are arranged in pairs distributed around the beam in four quadrants and along the beam in eight layers ("superlayers", SLs) as shown in figure 2.4.

The detectors cover the polar acceptance between 10 and 250 *mrad* with

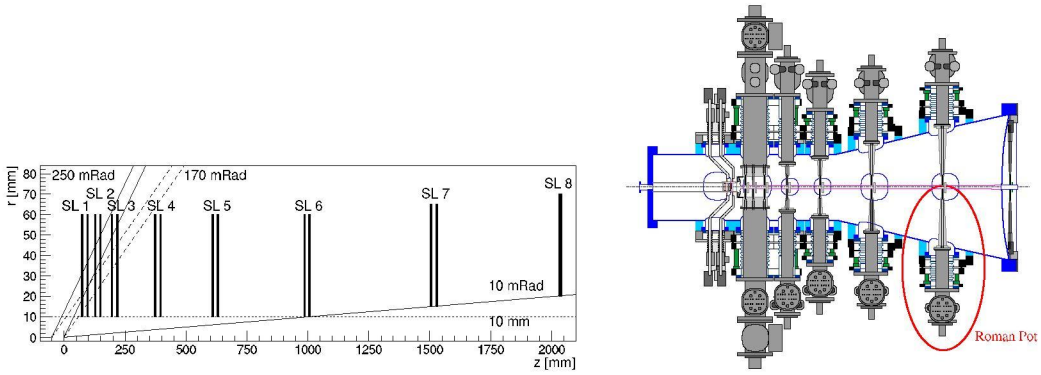

(a) (b)

Figure 2.5: (a): Radial distances of the different SLs with respect to the proton beam and acceptance of the VDS (b): VDS vessel equipped with target stations, detector modules mounted in Roman pots, manipulators and mini crates. Figure (a) has been taken from [Brä01], figure (b) from [Aga01].

every track coming from the targets and falling into that region crossing at least 3 superlayers. This acceptance determines also the shape of the stainless steel ultra-high vacuum vessel that is a part of the storage ring and into which the first seven superlayers are mounted as a Roman pot system in order to minimise multiple scattering (figure 2.5). The eighth superlayer located 2 m behind the targets is mounted directly after the aluminium exit window of the VDS vessel.

The detector modules of the first seven superlayers are mounted in Roman pots which are fixed to the vacuum vessel via manipulators for radial and lateral positioning.

As indicated in figure 2.5, the acceptance starting from 10 $mrad$ requires the detectors to be at a radial distance of 10 mm from the beam for measurement. During the injection of the proton beam however, a larger radial distance of 20 mm is needed, requiring radial movement. The lateral movement allows to distribute the expected flux of minimum ionising particles per cm^2 over a larger detector region by rotation of the detector positions. For 40 MHz interaction rate, this flux is comparable to that expected at the LHC: $(30\ MHz \cdot cm^2)/r^2$ minimum ionising particles per cm^2 with r being the distance to the beam [Bau00a].

Both detectors and the especially designed HELIX readout chip [Fal98], [Tru00], which integrates 128 channels with charge sensitive preamplifier, a shaper with 50 ns peaking time and a 141 cell deep pipeline each, have shown in tests to be still operational after the expected irradiation dose of one year,

after which the damaged modules are planned to be exchanged (see [Bau00a], [Bau00b] and references therein).

The double-sided strip detectors have dimensions of 53 mm × 73 mm with 280 μm thickness and an active area of 50 mm × 70 mm. The bulk is n type with 1024 "p on n" strips of 54.6 μm readout pitch and 1280 orthogonal "n on n" strips with a readout pitch of 51.7 μm. The strips are rotated by 2.5° with respect to the wafer edges. To enhance radiation hardness, each detector is surrounded by a multi-guard ring structure by which the voltage between the active area and detector edges is gradually reduced. Fully equipped, the VDS provides 147456 readout channels.

For every module, two double-sided detectors are mounted back-to-back on carriers with high thermal conductivity (see figure 2.6) that have a fork-like shape underneath the detectors in order to reduce the amount of material in the active area. The hybrids carrying the readout chips placed radially 4 cm further away with respect to the detectors and connected to them via multilayer Kapton cables are mounted on own carriers to separate the cooling paths. The copper cooling block to which all carriers are connected is located outside of the detector acceptance. The modules are operated in a secondary vacuum, being separated from the storage ring vacuum by 150 μm thick aluminium caps that also provide protection against RF pick-up. One module corresponds to 1.2 % radiation lengths averaged over the active area.

To reduce wake fields in the vessel, four 5 μm thick and 13 mm wide stainless-steel bands are strung parallel to the beam that serve as "beam pipe".

For every superlayer, four track projections[3] are measured (± 2.5° and 90° ± 2.5°) allowing standalone track reconstruction in addition to vertex finding. The resolution of the VDS is found to be about 40 μm in transverse and 630 μm in longitudinal direction for the convolution of primary and reconstructed J/Ψ vertices. The resolution is dominated by multiple scattering. The design values are oriented with respect to the typical B meson decay length and require a resolution of about 500 μm in longitudinal and 25 μm in transverse direction [HB95].

The VDS operation in the year 2000 showed that all components function and the achieved performance essentially corresponds to the specifications. Typical signal to noise ratios of roughly 25 (18) on the n- (p-)side and hit efficiencies above 95 % were achieved. A more detailed review on the performance of the VDS in the year 2000 can be found in [Bau02].

[3]For the data taken in the year 2000, which will be used in this thesis, in the first three superlayers one double-sided module was grouped with one single-sided module in every quadrant.

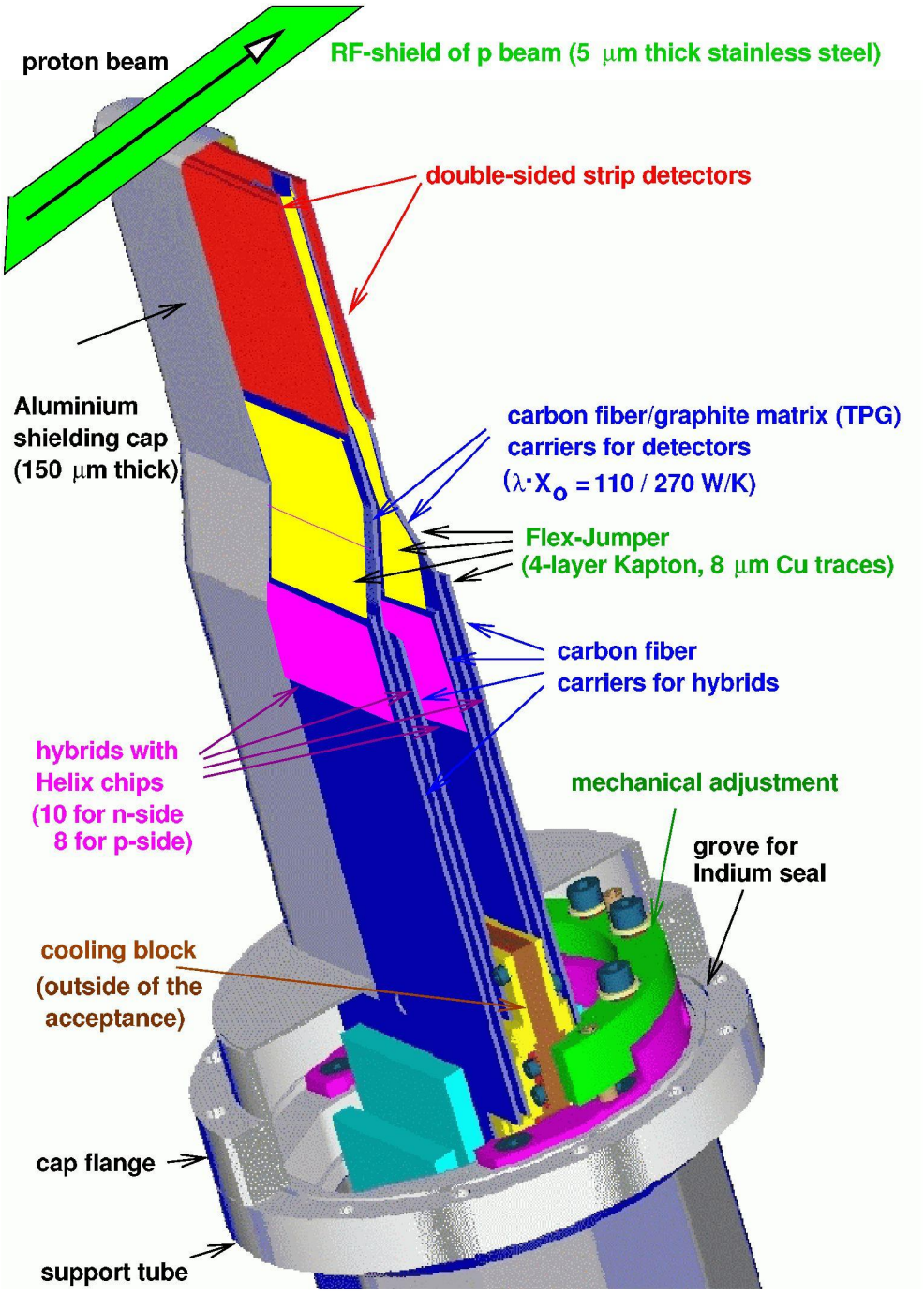

Figure 2.6: Cross section through a VDS detector module.

2.3.2 The Dipole Magnet

The spectrometer magnet uses normal-conducting coils that provide a field integral of 2.2 Tm at a power consumption of 1.1 MW. The curvature of the particle tracks due to the magnetic field occurs in the xz plane of the HERA-B coordinate system and allows to determine the momentum of the respective charged particle.

2.3.3 The Outer Tracker (OTR)

The outer tracking system [Cap00] is based on honeycomb drift chambers filled with an $Ar/CF_4/CO_2$ (65:30:5) gas mixture. The admixture of CF_4 makes the signals sufficiently fast in order to allow 10 MHz readout without pile-up.

The basic assembly of a detector module is shown in figure 2.7(a): The cathode is formed by a polycarbonate foil loaded with 6 % carbon ("Pocalon-C") for conductivity that is coated with copper and gold (40/50 nm). As anodes, gold-plated tungsten wires of 25 μm diameter are used, being supported about every 50 cm by FR4 strips to which they are soldered with 50 μm precision. The end pieces are open for gas circulation [Sch01].

To account for the different charged particle fluxes in the inner and outer regions of the OTR and limit both occupancies and total number of channels, in the inner region a cell diameter of 5 mm is used combined with a shorter cell length compared to the outer regions, where the cell diameter is doubled (see figure 2.7(b)). OTR modules with 5 mm cell diameter consist of four layers of 32 cells each, whereas those with 10 mm cell diameter are built of two or four layers of 16 cells each.

The complete OTR covers an area of about 1000 m^2, consists of roughly 1000 modules providing altogether 115000 channels distributed over 13 superlayers.

In each superlayer, three track projections ($0°, \pm 5°$) are measured. Seven superlayers are placed inside the magnet (Magnet Chambers, MC) to measure the track curvature and improve the momentum resolution. Four superlayers are located in-between Magnet and RICH providing straight track segments for pattern recognition (Pattern Chambers, PC). The last two superlayers are placed between RICH and ECAL and can be used for track extrapolations to the ECAL and muon system. Since they are primarily used by the first level trigger of HERA-B, they are also called Trigger Chambers (TC).

The size of the superlayers increases continously from MC1 ($0.9 \times 0.6\ m^2$) to TC2 ($6.5 \times 4.6\ m^2$). To allow better access, each superlayer is divided into two halves that can be moved along $\pm\ x$ direction of the HERA-B coordinate system.

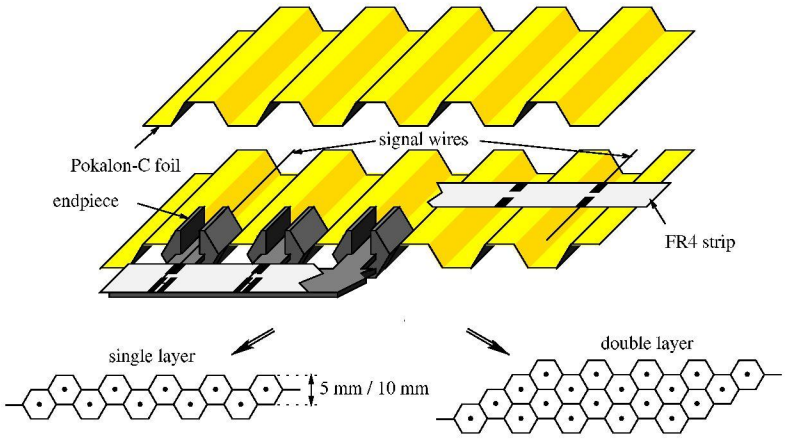

(a)

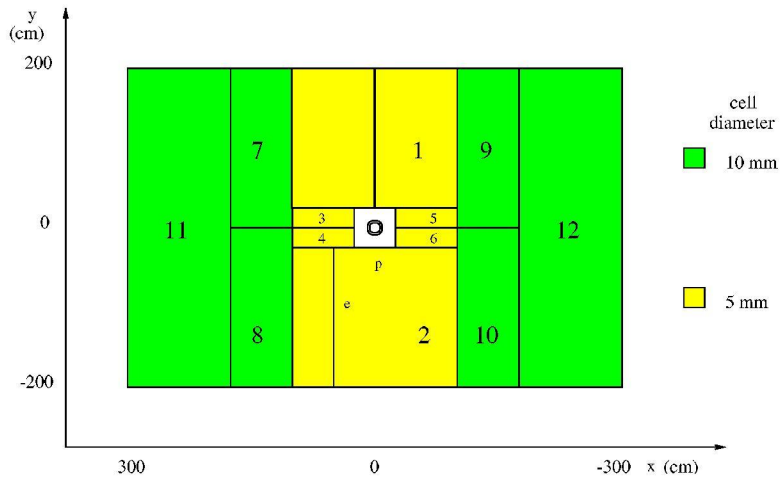

(b)

Figure 2.7: Basic structure of honeycomb chambers (a) and their assembly in a superlayer (b) using different cell diameters. Figure (a) has been taken from [Sch01], figure (b) is based on [Pes01].

Except for the losses of channels due to high voltage problems (see section 2.6), the OTR was working smoothly during the running in 2000. Using a method based on correlations of the measured drift times to estimate the intrinsic detector resolution yields $(350 \pm 50)\ \mu m$ for the 5 mm cells [HB00]. The remaining discrepancy to the design value of 200 μm can be explained by the fact that higher readout thresholds and a lower gas gain had to be used due to the high voltage problems. The resolutions obtained from tracking will be larger since a significant contribution of calibration and alignment is expected to be convoluted in those values.

2.3.4 The Inner Tracker (ITR)

The inner tracker [Zeu00] uses Micro Strip Gas Counters (MSGCs) combined with Gas Electron Multiplier (GEM) foils.

The MSGCs are built from 0.4 mm thick alkali-free glass that is coated with 80 nm amorphous carbon providing a defined surface resistivity in order to prevent the accumulation of ions from the gas amplification on the surface that could cause field distortions. On top of this coating a 0.5 μm thick golden electrode structure consisting alternating of 10 μm wide anode strips and 170 μm wide cathode strips with 60 μm gaps in-between is applied.

The GEM foils are mounted 2.8 mm above the MSGC wafer surface. They are made from 50 μm thick Kapton foils coated on both sides with 7 μm of copper. Into these foils holes with a diameter of about 55 μm in the Kapton and 90 μm in the copper are etched staggered with a pitch of 140 μm.

The drift cathode finally consists of a 125 μm thick Kapton foil coated with 18 μm copper and reinforced with a 0.3 mm thick G10 plate. The basic structure of a GEM-MSGC detector is sketched in figure 2.8.

Typical operation parameters are a drift voltage of -2500 V, a potential difference between the two GEM sides of about 440 V and a cathode voltage of -510 V, while the anodes are kept at ground potential. Consequently, regions of high field strength that allow gas amplification occur in the GEM holes and close to the anodes. The fields above and below the GEM foil are called drift and transfer field and their strengths are chosen to be roughly equal.

The pre-amplification of the GEM foils is necessary since the efficient detection of minimum ionising particles using only MSGCs would require too high gas gains inside the hadronic environment such that heavily ionising particles could induce discharges destroying the anodes.

As counting gas an Ar/CO_2 (70:30) mixture is used, since this shows good ageing properties and does not react with the detector components.

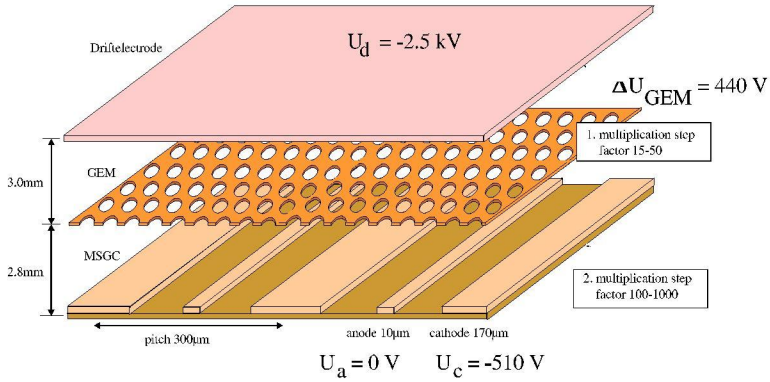

Figure 2.8: Schematic view of a GEM-MSGC detector as applied in the ITR. The typical multiplication factors in the two amplification zones are indicated. The figure is based on [Pes01].

The complete ITR system will consist of 184 chambers providing 768 anode strips each out of which 752 are read out via the HELIX chip, distributed over ten "stations" along the beam. Each station holds 8 to 32 chambers out of which four form one layer around the beam with some overlap to each other to avoid dead regions. Similar to the OTR, three track projections ($0°, \pm 5°$) are measured and the ITR is subdivided in the MC, PC and TC regions. The ITR provides tracking mainly for the positive x_F (see section 1.3) region, covering the polar acceptance between 10 and about 100 $mrad$. The nominal values for the resolutions of the ITR are $\sigma_x \approx 100\ \mu m$, $\sigma_y \approx 1\ mm$ and $\sigma_z \approx 3\ mm$.

In the year 2000, the ITR was being commissioned which resulted in low efficiencies in the beginning of the running period, affecting also the dataset used for the polarisation analysis as shown in section 5.2. However, in the last two months of the running period the operation of the ITR was stable and efficient, applying GEM-MSGC technology in a large scale for the first time in a high energy physics experiment.

A detailed description of the performance of the ITR in the year 2000 can be found in [Bag01], reflecting also the experience gained with several discharge phenomena in the hadronic environment of HERA-B.

2.4 The particle identification system

Based on the needs for an efficient detection of the particles produced in the golden decay (see figure 1.3), HERA-B comprises several subsystems for

particle identification:

The **Ring Imaging Čerenkov Counter (RICH)** [Ari00] allows the separation of electrons, pions, kaons and protons utilising the Čerenkov effect: If a particle traverses a medium of refractive index n at a velocity $\beta \cdot c$ greater than the speed of light c/n in this medium, it emits photons on a cone with opening angle θ_C around its trajectory. This opening angle θ_C depends on n and β as follows: $\cos\theta_C = 1/(\beta n)$.

In the HERA-B RICH, the radiator gas perfluorobutane (C_4F_{10}) is used. The emitted photons are projected by mirrors into circles on the focal surfaces, where they are detected by photomultiplier tubes. By measuring the ring radii, the Čerenkov angles are determined. Together with the momentum information provided by the tracking system, the mass of the particle can be measured: Rewriting the Čerenkov angle relation in the small angle approximation, we get $\theta_C^2 = \theta_{\beta=1}^2 - m^2/p^2$, with $\theta_{\beta=1} = \arccos(1/n)$ being the maximal Čerenkov angle and m the particle's mass. Consequently, when θ_C^2 is plotted versus $(1/p^2)$, particles with a given mass will lie in a band with slope $-m^2$.

The HERA-B RICH allows to separate electrons from pions in a momentum range of 3.4 - 15 GeV/c, pions from kaons in a range of 12 - 54 GeV/c and kaons from protons between 23 GeV/c and 85 GeV/c. $\theta_{\beta=1}$ is found to be 52.3 $mrad$ [HB00].

The **Electromagnetic Calorimeter (ECAL)** [Zoc00] allows the identification of electrons (positrons) and photons via their electromagnetic showers and measures their energy and position. For an electron, the ratio of energy divided by total momentum should be close to 1. A photon can be identified via the lack of a corresponding trajectory in the tracking system.

The HERA-B ECAL consists of 5956 square shaped calorimeter cells and is divided into three regions with different granularity: The cell size in the inner region is 2.24 $cm \times 2.24$ cm, 5.59 $cm \times 5.59$ cm in the middle section and 11.18 $cm \times 11.18$ cm in the outer region. All cells are of "shashlik" type, using a sampling scintillator/absorber sandwich structure, through which wavelength shifter fibres are running perpendicularly that are read out by photomultiplier tubes positioned behind the modules. In the inner region tungsten is used as absorber material, with the cell depth of 13 cm corresponding to 23 radiation lengths, whereas in the outer regions lead is used as absorber in the modules of 34 cm depth, corresponding to 20 radiation lengths. The respective Molière radii are 1.42 cm in the inner and 4.15 cm in the outer regions.

For the inner part, the energy resolution was measured to be $\sigma(E)/E = 22.5\ \%/\sqrt{E} \oplus 1.7\ \%$ with a spatial resolution of 0.2 cm [Avo01].

The **Transition Radiation Detector (TRD)** located in front of the second trigger chamber TC02 is planned to improve the electron-hadron separation in the central region around the beam pipe with an electron identification efficiency of >95 % and a hadron rejection power against single pions of up to 10^{-2} [Sav98].

The **Muon system** [Tit00]: For the detection of muons, their penetration capability can be exploited.

In HERA-B, four superlayers of gas proportional chambers are used for muon detection and tracking with about 1 m thick absorber layers made up of iron and armoured concrete blocks in front of the first three superlayers. The total absorber thickness of about 3 m is a compromise between required hadron absorption and tracking performance limited by multiple scattering. The chosen absorber thickness leads to a low-momentum cut-off at roughly 4.5 GeV/c.

The muon system covers polar angles starting from 9 $mrad$ around the beam pipe up to 160 $mrad$ in y and 220 $mrad$ in x. Each superlayer consists of pixel chambers in the high occupancy region close to the proton beam pipe and tube and pad chambers in the outer sections. In total, the muon system provides roughly 30000 readout channels.

The system performance is discussed in [Tit00] and [HB00].

2.5 Trigger and Data acquisition system

The trigger and data acquisition system of HERA-B is clocked using the HERA timing of 10.4 MHz. To read out all $\sim$ 500000 channels of the experiment at this frequency would correspond to a data-flow of $\sim$ 4.7 TB/s. Even if it would be possible to permanently store these data, it would not be feasible to reconstruct this amount of data with today's standard computing technology. The natural approach to handle this data-flow is thus to preselect the measured data very quickly and scale down the amount of data that has to be read out, processed and stored.

For a measurement of CP violation in the Golden Decay with HERA-B, almost all events are not interesting since the signal to background ratio is about $2.9 \cdot 10^{-11}$. Consequently, an efficient background suppression and selection of useful events is crucial. For this purpose, a four stage trigger system [Kre01] with a pretrigger has been designed (see figure 2.10). It searches for lepton pairs originating from the target region already at the first level, corresponding to the signature of the Golden Decay depicted in figure 1.3:

The **pretriggers** search with few, fast available signals for electron can-

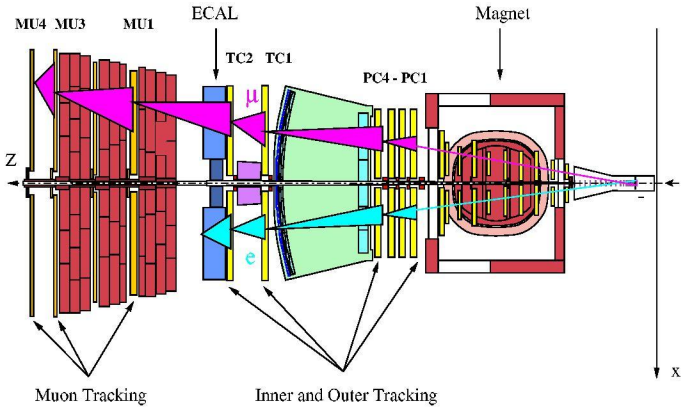

Figure 2.9: The basic concept of the FLT: The way a track is followed towards the magnet exit using ROIs is indicated. The figure is taken from [Sch01].

didates in the ECAL (selected by cluster shape and energy) or muon candidates in the muon system (selected by coincidences in the last two muon superlayers)[4] [Avo01, Ada01].

If lepton candidates are found, the **First Level Trigger** (FLT) receives their positions from the pretriggers, and follows the track candidates towards the magnet inside a corresponding search field (see figure 2.9), the "region of interest" (ROI), based on a Kalman filtering technique using a subset of the available tracking chambers. To enlarge efficiencies, hits used by the FLT are a logical OR of two cells. If a track candidate can be traced back to the exit of the magnet a rough momentum estimation can be obtained from the kink in the magnet, assuming the track originated from the target region. Finally, the invariant mass of all possible combinations of accepted lepton candidates can be estimated and a cut on a certain mass window (e.g. the J/Ψ) can be applied using lookup tables containing the trigger decision.

The FLT is realised in dedicated hardware processors to be able to give a trigger decision within 12.3 μs. Since in this time 128 bunch crossings will occur, all sub-detectors have to be able to store their raw data together with the respective bunch number in internal pipelines for this time.

The FLT is designed to reduce the event rate by a factor of 200, resulting in an input rate of 50 kHz for the next trigger stage.

If an event has been accepted by the FLT, the entire detector data for the respective bunch crossing are stored in the second level buffer (SLB) realised

[4]In addition, high-p_t tracks can be searched for with the three superlayers of pad and pixel chambers of the high-p_t system located inside the magnet, allowing also the search for hadron pairs.

in the dual ported memories of DSP's. The **Second Level Trigger** (SLT) refines the selection of the FLT by refitting the tracks more precisely using more tracking superlayers and also the drift time information in the ROIs. If a track candidate can still be traced back to the exit of the spectrometer magnet, it is propagated through the magnet using a look-up table for the magnetic field and track segments in the VDS are reconstructed. An event is accepted, if the lepton pair candidates have a common vertex, that can be additionally demanded to be displaced from the target to suppress prompt J/Ψs.

The SLT is implemented in a farm of 240 off-the-shelf PCs that are connected to the DSP's that also provide the necessary switched network to the SLB. The suppression factor due to the SLT is 100 - 1000, resulting in an output frequency of 500 - 50 Hz, depending on the event class that is searched for. For the J/Ψ trigger, the output rate should be already low enough at this stage to make further event filtering unnecessary.

After a positive decision of the SLT, a complete event record is built from the respective information stored in the SLB. There is an option to use additionally a **Third Level Trigger** (TLT) algorithm, running on $\sim$ 20 % of the CPUs of the SLT/TLT farm. This would thus be the first trigger level that can use the full event information and an additional reduction of the event rate by a factor of 10-20 for certain event classes is expected, yielding an output frequency of $\sim$ 50 Hz that can be logged to tape. In the year 2000 running, however, this option was not needed since the event rate delivered by the SLT was already below 50 Hz.

The data of the SLT/TLT farm are transferred via a commercial network to the **Fourth Level Trigger** (4LT) also being implemented in a farm of 200 off-the-shelf PCs. Here the events are completely reconstructed, classified and - if still necessary - filtered such they can be archived (logged) on tape. Since only about 10 MB/s can be logged, the maximum logging rate is about 50 Hz for an average (reconstructed) event size of $\sim$ 200 kB.

Additionally, on the 4LT farm alignment and calibration constants can be calculated online and data quality monitoring is done.

The described trigger system is highly configurable and thus allows trigger modes different from the one described above, like triggering on single leptons, tracks with high p_t, events containing an interaction[5], or a random trigger uniformly sampling all HERA bunches (yielding minimum bias data). In the case of minimum bias data taking, no preselection is needed (except perhaps for an interaction trigger) and the amount of data that can be taken

[5]An interaction can be detected e.g. by energy deposition in the ECAL above a certain threshold or by demanding a minimal number of photons in the RICH.

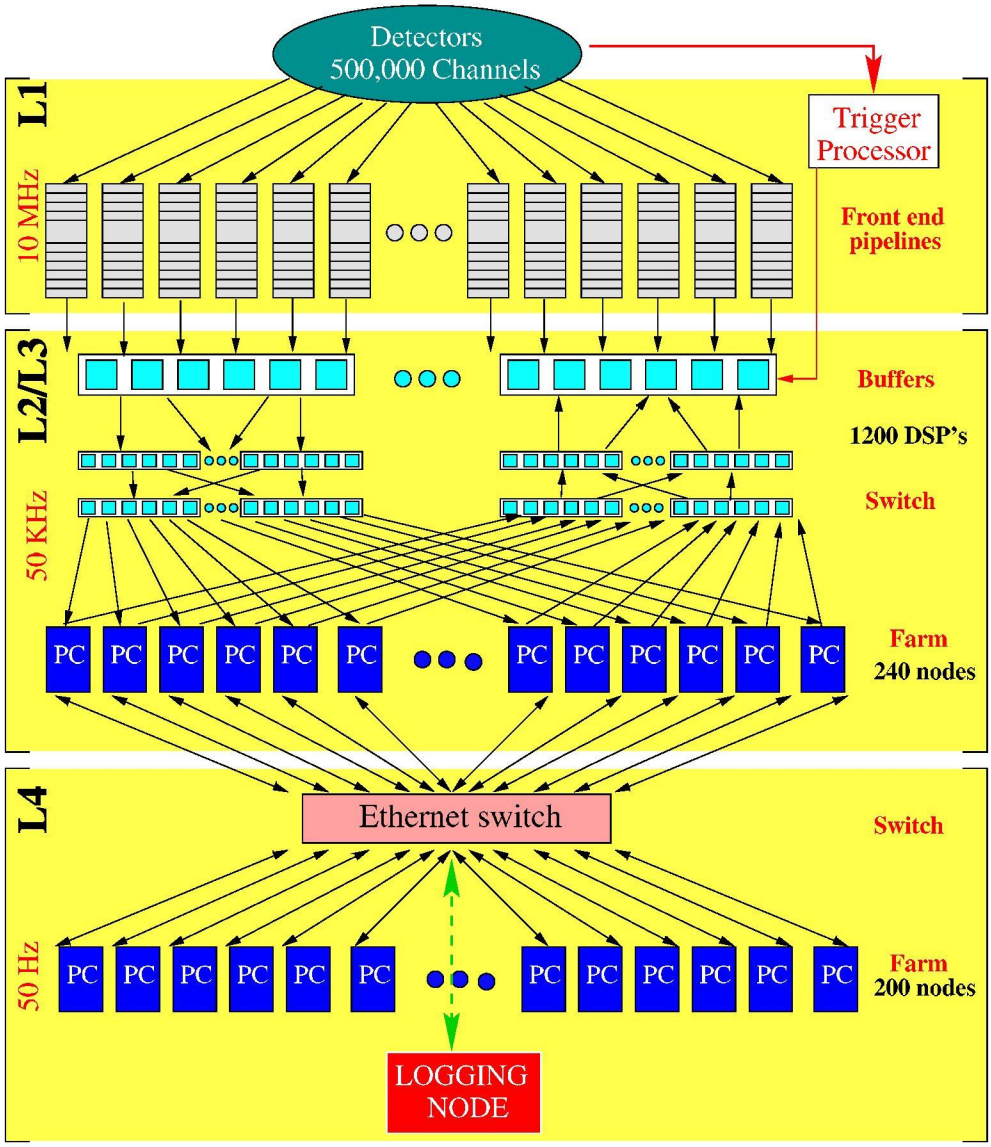

Figure 2.10: The data acquisition system of HERA-B with corresponding trigger levels and event rates. The figure has been taken from [HB00].

in a certain time period is limited by the maximal possible logging rate.

The complete chain of data acquisition is summarised in figure 2.10 and a more detailed description of the HERA-B data acquisition system can be found in [Her00, San02c].

2.6 Detector status in the year 2000

The detector assembly was principally finished in the end of 1999, and the year 2000 running was thus devoted to the commissioning of the detector. This process was already essentially completed for some subsystems like the RICH or VDS, whereas it took longer than expected for other subsystems like ITR, OTR and the FLT. This was not due to problems with the high radiation environment, but more due to not properly commissioned electronics.

For example, the OTR continuously lost channels mainly due to shorts on the high voltage distribution boards at such a rate that by the end of the running in 2000, the OTR had almost lost 7 % of his channels due to this problem. Due to the organisation of the high voltage distribution, the temporary channel losses were even higher since the final containment of the error requires short access to the detector which is possible on average once per month.

Especially since the commissioning of the FLT could not be completed within the running period 2000 that ended in August due to the luminosity upgrade of HERA, the detection of Golden Decays as described in section 2.5 was not feasible. Nevertheless, several major data sets were taken, including also minimum bias data that will be used for the presented analysis.

The long HERA shutdown and possible access to the detector for more than one year allowed for many improvements of the sub-systems. A detailed description of the detector condition in 2000 and the planned improvements during the shutdown in 2000/2001 can be found in [HB00] and references therein. Also from the physical and software point of view, the collaboration has taken advantage of the available time for a deeper understanding of detector calibration and alignment and for improvements of the reconstruction and analysis framework. Consequently, HERA-B is eagerly awaiting data taking in 2002 with a highly improved detector.

The experiences gained so far also provide important input for the future planned hadronic B factories like LHCb.

Chapter 3

Minimum Bias data and analysis framework

After introducing the minimum bias dataset used for the polarisation analysis, this chapter will describe how tracks and vertices are reconstructed from the data and which criteria are used to select high quality physical tracks.

3.1 The Minimum Bias dataset

The main contribution to events seen by the HERA-B spectrometer are "soft" inelastic interactions producing the light u, d and s quarks in the final state according to the respective cross sections. For any heavy flavour decay to be disentangled from the observed event, those interactions form the underlying background. A detailed investigation of such inelastic interactions without using any trigger to enhance heavy flavours is thus not only useful for studies of the basic underlying physics, but also a fundamental step of detector commissioning.

For this purpose, four HERA proton fills were used in April 2000 for a minimum bias running, where data were taken with a random trigger uniformly sampling all HERA bunches. In order to be able to study dependencies on target material and interaction rate, for each available target material (Al, C, Ti, W) a proton fill was used and target rate scans were performed. To monitor the stability of the detector performance, one calibration run was taken per fill under the same conditions using the titanium wire at 5 MHz interaction rate. For detailed studies of A dependencies, also large data samples were collected for each target material at 5 MHz target rate.

The data taking period took place under very stable detector conditions and the results of detailed studies of e.g. single particle inclusive distributions

were used to tune the Monte Carlo description of the HERA-B detector. This well studied dataset was also used for the Λ polarisation analysis[1], and the basic features of the *used* data are summarised in table 3.1.

data taking	10. - 14. 04. 2000 (57h)
trigger	random
target rate	$1 - 10\ MHz$
used targets	inner 1 (Ti), inner 2 (C), above 2 (Al), below 2 (W)
used events	3 952 085

Table 3.1: Properties of the minimum bias dataset used for the analysis. For the target naming scheme refer to figure 2.3 (a).

Because data taking at 20 MHz was not very stable and did not take place for all target materials, these runs were not included for the polarisation analysis. The loss of statistics due to this is roughly 3 %. Since for the data taking mainly a random trigger was used, about 50 % of the recorded events were empty. A list of the used runs with further details can be found in appendix B.

3.2 Event reconstruction

The software framework used for event reconstruction and also analysis at HERA-B is called ARTE (Analysis and Reconstruction Tool, [Art02]). ARTE is used both for *online reconstruction* for data quality purposes and fast feedback to the data taking and *offline reconstruction* (reprocessing) of the data when all calibration constants are known.

The event record is stored in different linked data structures called tables from low level information like hits (HITB table) via intermediate steps of reconstruction as track segments in different sub-detectors (RSEG table) up to highest level information like fully reconstructed tracks (RTRA table) and vertices (RVER table). The tables also contain links to entries from other tables that were used for the filling of the respective table, allowing to reproduce the flow of information afterwards.

The filling of the different tables is done by various functions, some of which will be outlined shortly to give a glimpse on the reconstruction chain.

[1]The term "Λ polarisation analysis" or "polarisation analysis" will be used throughout this thesis referring to the polarisation analysis of *both* Λ and $\bar{\Lambda}$.

Again, special emphasis will be placed on VDS and OTR since they play a basic role in the presented analysis.

Hit preparation

Before any track reconstruction can start, the raw data have to be translated into hit information for each sub-detector. As an example, for the vertex detector the data reduction due to selection of hit information from the raw data is a factor of 20, taking into account a maximal occupancy per event of 5 % [HB95].

In case of the VDS, the program package MARVIN [Wag99] is performing the following steps to isolate hit-information from the raw data:

1. For each channel, a characteristic, slowly varying pedestal is determined and subtracted.

2. For all channels of a readout chip, baseline jumps[2] are evaluated and subtracted for every event.

3. After those steps, for each channel the level of statistical fluctuations (noise) is determined.

4. Finally, the search for hits is performed for one or more neighbouring VDS strips ("cluster") by checking the height of a possible signal above the statistical fluctuations.

5. For identified clusters, the centre of gravity is stored together with signal to noise value and number of contributing strips into the HITB table.

A more detailed description of the used algorithms and cuts in MARVIN can be found in [Wag99].

For the OTR, the raw data are sparsified removing channels containing no signal. For the filling of the HITB table, noisy channels are removed before the combined information of hit position and drift time is stored.

Standalone reconstruction and track finding

After the filling of the hit information, the standalone reconstruction for each sub-detector can start with ring search in the RICH, energy cluster finding in the ECAL and track segment reconstruction in VDS, OTR,....

[2]baseline fluctuations on an event by event basis affecting all channels of a readout chip, also called common mode

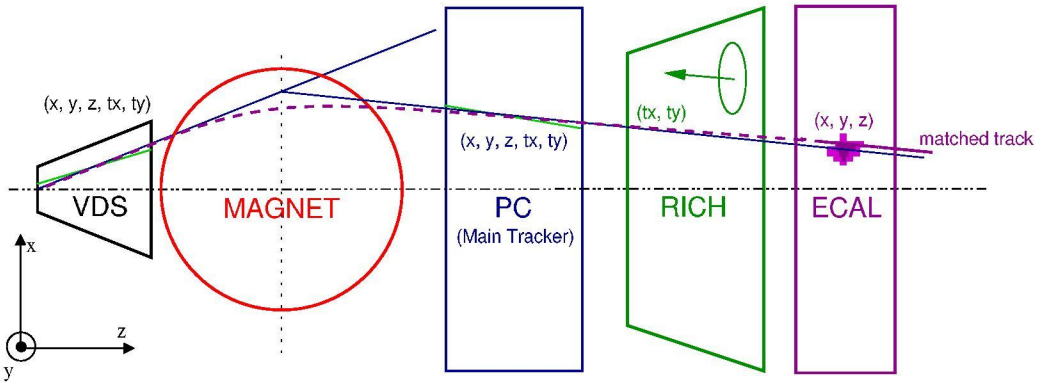

Figure 3.1: The track matching: VDS and PC (Pattern Chamber) segments are prolongated to the magnet centre at $z = 4.55\ m$ and cuts on the differences in the x position are applied. The figure is based on [Aga01].

The track reconstruction package used in the VDS is CATS (a Cellular Automaton for Tracking in Silicon [Eme01a], [Kis99]). Unlike many other tracking programs based on the Kalman filter, this package utilises a cellular automaton for track search.

Since this algorithm is based on space points, first all hits in the planes of a superlayer are combined into three dimensional points whose coordinates are corrected for the track slopes assuming the tracks originate from the target region. To compensate possible detector inefficiencies, a space point can be built from two to four hits. Then track segments combining neighbouring superlayers with at most one missing superlayer in between (regarding detector acceptance and inefficiencies) are forming the cells on which the automaton is finally run. From the track candidates proposed by the automaton finally the longest and smoothest are selected and fitted with a discrete Kalman filter algorithm.

For the main tracker, a package based on the same principles, OTR/ITR-CATS has been developed [Eme01b]. The results for the respective track segments is stored in the RSEG table.

Track matching

After the standalone reconstruction is done for every sub-detector, the individual information is combined into objects (tracks) traversing the complete detector (see figure 3.1). The package used for the merging of track segments, ECAL clusters and RICH rings into a complete track is MARPLE [Igo98]. Many matching schemes are possible and supported within MARPLE like

VDS-MAIN, VDS-RICH, VDS-ECAL, MAIN-RICH, MAIN-ECAL,....

The matching between track segments in the VDS and in the main tracker pattern chambers (PCs) behind the magnet is the most important one for the polarisation analysis (information from the magnet chambers was not used). For this, the point at the end of the VDS segment is extrapolated to the PC entry point using the segment slope. Segments passing a cut on the difference in y (where no bending occurs) are propagated together with the PC segment to be matched with, into the centre of the magnet where a cut on the difference in x is applied. On the found matches a refit is performed before further matches to the ECAL and RICH are added.

The RTRA table in which the results of the matching are stored, contains the found track parameters (the initial space point of the track with the slopes), the momentum and charge of the track, the χ^2 and degrees of freedom of the track fit, the number of hits in the sub-detectors, IDs for the used segments and likelihoods for different particle hypothesis determined by RICH, ECAL, muon system and TRD.

Vertexing

The vertexing package used for primary and secondary vertex[3] finding in this analysis is GROVER (Generic Reconstruction Of VERtices) [Eme01c].

The primary vertex finder applies the Rover algorithm [Eme00] where only tracks within 3.5 σ of the target wire(s) are used with σ being the track resolution. The changing wire position can be determined internally by a wire following mechanism based on the statistical mean of positions of reconstructed primary vertices. The vertex fit itself is performed without usage of momentum information purely based on geometrical track information using a Kalman algorithm.

For all vertices found, information like position, covariance matrix, links to used RTRAs, χ^2 and degrees of freedom of the fit and a type flag is stored in the RVER table.

Reconstruction settings used for the analysis

The reconstruction chain described above is identical for both real and Monte Carlo simulated data as soon as the hits are prepared[4]. The ARTE version

[3] A primary vertex denotes the location where the first interaction occurs. Secondary vertices result from the decays of long living particles produced in the primary interaction or subsequent interactions of the particles emerging from the primary vertex.

[4] For reasons that will be explained in section 5.2, no information of the ITR was used in the reconstruction.

used for reconstruction in the Λ polarisation analysis was `ARTE-03-09-r3`. The kumac used for the steering of the various subprograms was based on the rp3004 kumac [Her02] which was a predecessor to that of the official third reprocessing of the year 2000 data basically using an older calibration database version (KEYBOOK 14) than the final version. The later database changes had no impact on the presented analysis since they were mainly introducing an improved noise reduction in the ECAL [San01].

3.3 Clone removal

Since the RTRA table contains every combination of track segments that the matching procedure between the sub-detectors generates, many track segments are used more than once to form a track (see figure 3.2), which has mainly two reasons:

- In order to increase *efficiency* in the track finding, many different combinations using the same track segments are stored with the drawback that the user himself has to take care of the *purity* of the track sample he wants to use.
- In the search for special physical processes like pair conversions where the pair could appear in the VDS as one segment due to its small opening angle and then show up as two segments in the main tracker after the magnetic field, the multiple usage of track segments can be useful.

However, for many analysis purposes it is essential to select a clone-free subset of all tracks provided in the RTRA table where every track segment is used only once. The unification of the algorithm to determine this subsample of the RTRA table also allows easier comparison of the results of different analyses being based on the same set of tracks.

The function Cloneremove is such a tool to select the tracks according to simple criteria which will be described in detail below. This selection is just using two basic conditions in order to allow a preferably unbiased analysis:

1. Only reconstructed charged tracks are accepted having the RTRA fit flag = 0.
2. Only tracks having at least a VDS segment are used.

The *basic idea* of this tool is very simple: The algorithm will ignore all tracks which do not fulfil the two requirements stated above and sort the

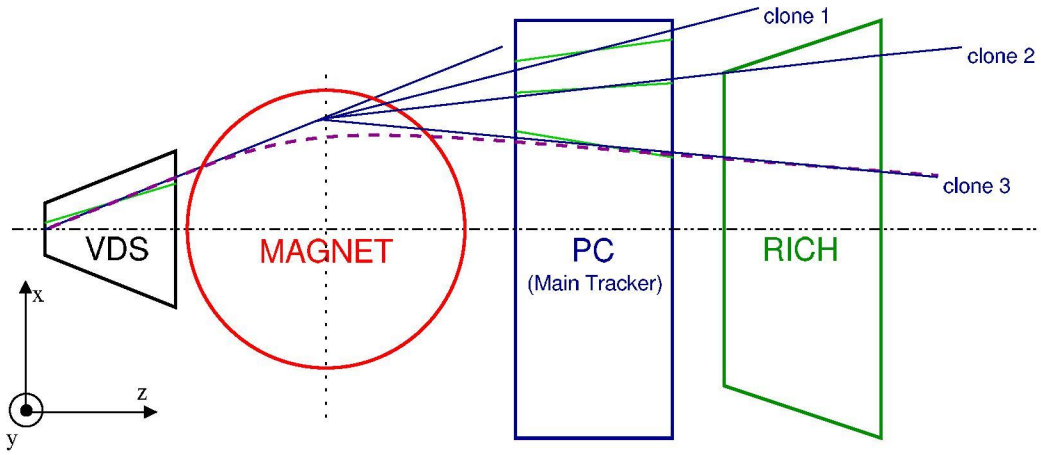

Figure 3.2: Generation of track clones: The matching procedure may use track segments more than once to form a complete track. Tracks sharing the same track segment are called clones. The figure is based on [Aga01].

remaining tracks according to their quality. Then, the tracks are accepted beginning with those of highest quality. Before a track is approved, it is checked whether this track is not using segments already used by (higher quality) tracks accepted before.

The tracks accepted by this code can be any combination of a VDS-segment with MAIN/ECAL/RICH or VDS only tracks. For all approved tracks, the bit `Rsegc::clonerm` in the RTRA `cmp` field is set and the number of accepted tracks is returned by the program. Thus, no tracks are actually discarded from the RTRA table, but the clonerm bit allows easily to select a well-defined clone-free subset from the full RTRA table.

The *key problem* for the Cloneremove function is to find an appropriate track quality algorithm without introducing a bias. The information available for this purpose is anything stored in the RTRA table like:

- Number of hits of the track in the sub-detectors
- Number of sub-detectors seeing the track
- χ^2 per degrees of freedom of the track fit.

Many different algorithms calculating a figure of merit (FoM) using the available RTRA information have been tested and their performance was judged by the resulting quality of the K^0_s signal in a reference data set (details can be found in [Ple01]). Finally, the simplest algorithm with the best signal has been used for Cloneremove, working as follows:

- First, the number of hits in the VDS and main tracker are added up.
- If RICH information exists, the number of hits divided by four (rescaled with respect to the average number of hits in the VDS) is added.
- If the ECAL is present, a further 1 is added.
- From this number finally the χ^2 per degrees of freedom of the track fit is subtracted intermixing the basic hierarchy of tracks with respect to the presence of different sub-detector information.

The resulting figure of merit reads as follows:

$$FoM = hitsvds + hitsmain + \frac{hitsrich}{4}^{\exists ECAL?}_{+1} - \frac{\chi^2}{ndof}.$$

For the analysis described in this thesis, version 1.2 of `Cloneremove.C` was used. The differences to version 1.0 described in [Ple01] are the following:

1. Usage of trigger information was added: Triggered tracks get a very high FoM and are thus preferred with respect to "normal" tracks. They cannot be skipped due to a missing VDS segment or wrong fit flag.
2. For tracks with clone-free VDS and MAIN segments no clone removal is done any more for RICH and ECAL.
3. The implementation was improved by using higher precision internal variables and excluding the theoretical possibility of losing tracks with the same FoM[5].

All changes had only a marginal impact on the performance and behaviour of the code described in [Ple01].

`Cloneremove.C` might be further improved in the future by exploiting the extra information that has meantime been added in the RTRA table. For example, for VDS and OTR now bit patterns for the expected and found hits in the detector layers are available. This allows to judge the track quality not by the absolute number of hits of a track but relative to the expected number of hits, no longer preferring long tracks with respect to short ones. Additionally, more than one check bit might be introduced to account for the different demands of the various analysis tasks.

[5]To improve code readability, the name of the check bit `Rsegc::bit20` was substituted by `Rsegc::clonerm`.

Chapter 4

V^0 reconstruction

The typical topology of a V^0 event is shown in figure 4.1: A V^0 appears as a two track secondary vertex downstream from the target region, with the reconstructed total momentum pointing back to the target. Thus, for an efficient reconstruction of inclusively produced $V^0 s$, vertex and momentum information on the decay products are crucial. Once this information is available, it is straightforward to check different mass hypothesis for each decay vertex and improve the physical signal by requiring V^0 characteristics like a certain flight length and impact parameter to the primary vertex.

In this chapter it will be shown how the background to the V^0 signals mainly coming from primary vertex tracks and low momentum tracks affected

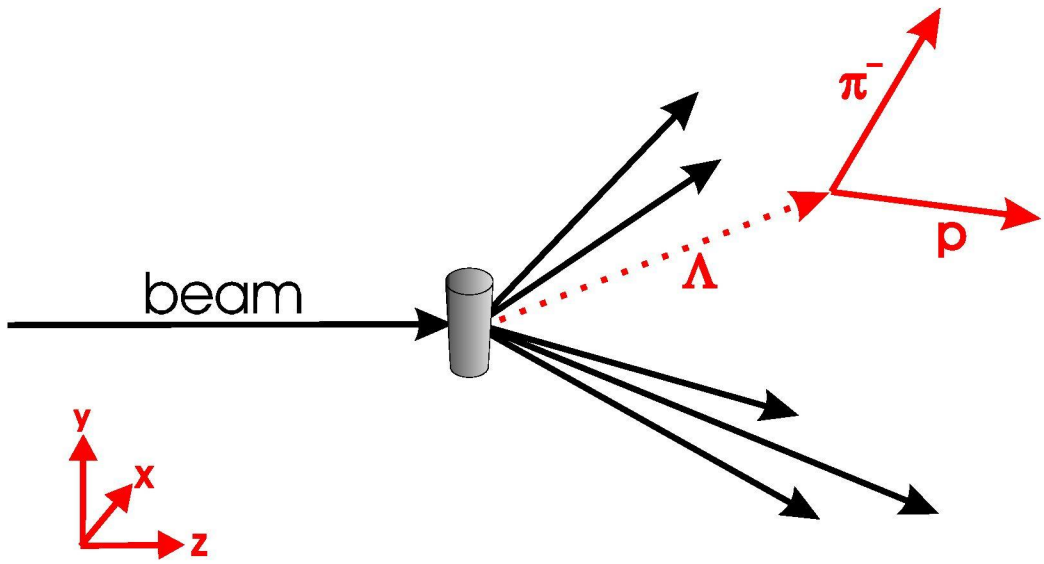

Figure 4.1: Typical topology of a V^0 event.

strongly by multiple scattering can be effectively separated from the signal by using appropriate cuts and track selection. Thus the usage of the particle identification sub-detectors of HERA-B like the RICH was not necessary for the V^0 reconstruction.

4.1 V^0 selection criteria

After the preparation of tracks and vertices as described in chapter 3, finally the V^0 reconstruction[1] can start as follows:

- In order to skip quickly empty events, first it is checked that the event contains at least two tracks after clone removal.
- After this it is demanded that the event to be processed contains at least one primary vertex consisting of at least three tracks or segments in the VDS.

For any event fulfilling these requirements, all pairs of oppositely charged tracks are vertexed. For the mass hypothesis to be used, the kinematical properties of the different V^0 decays illustrated in figure 4.2 can be exploited [Pod54]: Here the transverse momentum p_t of the oppositely charged decay products with respect to the V^0 is plotted versus their asymmetry in the longitudinal momentum relative to the V^0. Since the decay products of $K_s^0 \to \pi^+\pi^-$ have the same mass, their momenta will be on average symmetrically distributed, whereas for $\Lambda \to p\pi^-$ ($\bar{\Lambda} \to \bar{p}\pi^+$) the (anti-) proton will take on average more momentum, resulting in the asymmetry shown in figure 4.2. It should be noted that in the regions where the K_s^0 band overlaps with the Λ ($\bar{\Lambda}$) band, both particles are kinematically indistinguishable on an event by event basis[2]. Thus, to minimise the background on the Λ ($\bar{\Lambda}$) signal, this overlap region should be removed.

For every track pair, the maximum of the momentum ratios $max\left(\frac{p^+}{p^-}, \frac{p^-}{p^+}\right)$ is calculated. If it is smaller than 4, that is if the momenta are distributed more symmetrically, first the K_s^0 mass hypothesis is checked, else the Λ or $\bar{\Lambda}$ hypothesis is tested, depending on the charge of the track with the dominant momentum. If the calculated invariant mass does not fall into a predefined window ($0.428\ GeV/c^2 < m_{K_s^0} < 0.568\ GeV/c^2$ respectively

[1] The used algorithm was based on the file `rcSelect_K0S_Lambda.C` in the ARTE `reco` module. Since this code is using an outdated track selection, this was replaced by `Cloneremove.C`, version1.2 (see section 3.3).

[2] In high statistics, those K_s^0's will form a flat background under the $\Lambda/\bar{\Lambda}$ signal.

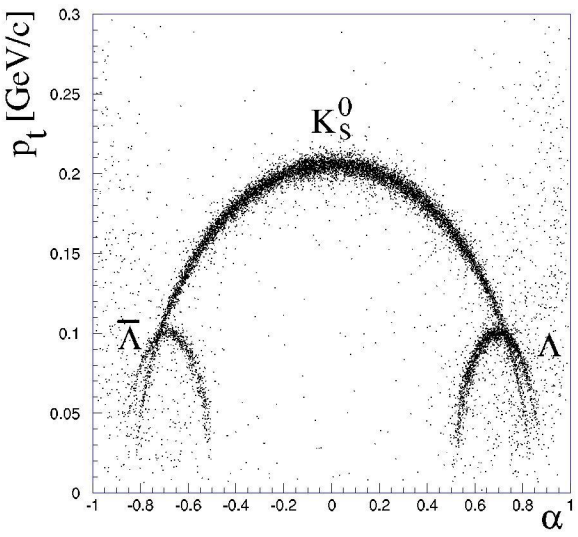

Figure 4.2: Armenteros-Podolanski plot for V^0s [Pod54]: The transverse momentum p_t of the oppositely charged decay products with respect to the V^0 is plotted versus their asymmetry in the longitudinal momentum relative to the V^0 $\alpha = \frac{p_l^+ - p_l^-}{p_l^+ + p_l^-}$.

$1.09\ GeV/c^2 < m_{\Lambda/\bar{\Lambda}} < 1.14\ GeV/c^2$), the remaining hypotheses are cycled through: $\underleftarrow{K_s^0 \rightarrow \Lambda \rightarrow \bar{\Lambda}}$.

If no hypothesis fits into the mass window, the actual track combination is skipped, else the information about this V^0 candidate like the momenta of the two tracks, the positively checked particle hypothesis, etc. is filled into an ntuple.

Of special interest are variables that can be exploited for improving the desired signal quality. The following information is used for further cuts[3]:

1. the distance between the V^0 tracks, cut at $>$ 400 μm
2. the impact parameter of the V^0 to the closest primary vertex, cut at $>$ 600 μm
3. the flight path of the V^0 in the V^0 rest frame ct_0 ("flgt"), cut at $<$ 1.3 mm
4. the flight path of the $\Lambda/\bar{\Lambda}$ in the $\Lambda/\bar{\Lambda}$ rest frame $ct_0 \cdot p_t$ of the decay products relative to the $\Lambda/\bar{\Lambda}$ ("p_t·flgt"), cut at $<$ 0.05 $cm\ GeV/c$.

[3]For the filling of the ntuple, however, all cuts quoted below are not yet applied in order to be still able to study the behaviour of the signal depending on the cut values.

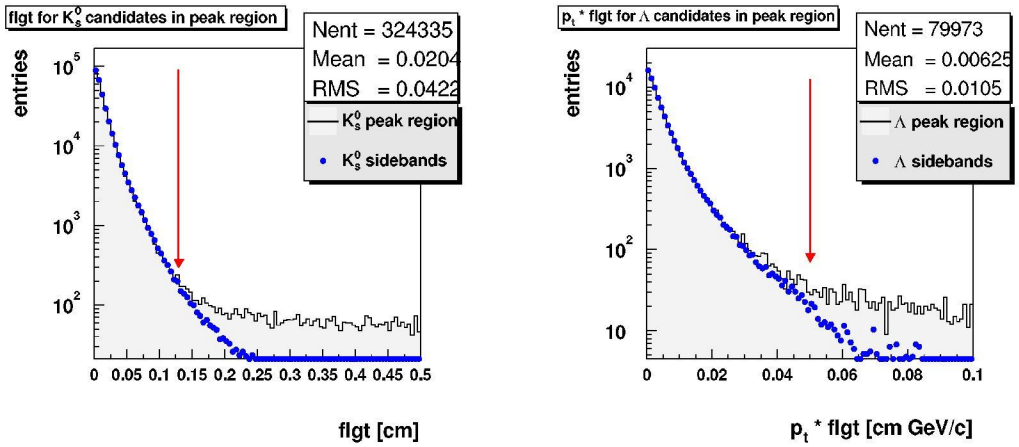

(a) (b)

Figure 4.3: Distributions of cut variables for the V^0 signals in the minimum bias dataset after the preselection cuts: (a) the flight path of the K^0_s in the K^0_s rest frame ct_0 and (b) the flight path of the Λ in the Λ rest frame $ct_0 \cdot p_t$ of the decay products relative to the Λ are shown for peak and sideband regions respectively. The chosen cut values are indicated by the arrows.

The first two cuts can be understood as a soft preselection in order to reduce the amount of data to be processed: Taking into account the resolutions of the VDS as stated in [Brä01], the cut on the distance between the V^0 tracks corresponds to more than 6 σ of the distance of closest approach distributions. The cut on the impact parameter to the closest primary vertex corresponds to more than 8 σ of the impact parameter resolution.

The cut on the flight path of the V^0 in the V^0 rest frame is a very powerful tool in order to get rid of much shortlived background produced in the target. Since $c\tau_{K^0_s} \approx \frac{1}{3}\, c\tau_\Lambda$, the cut is much more selective on the K^0_s signal than for the Λ.

In figure 4.3 (a) the distribution of the flight path ct_0 is shown for the 3 σ peak region of the K^0_s signal (histogram) overlayed with the distribution in the sidebands which is normalised to the peak distribution (polymarkers) after applying the preselection cuts 1. and 2.. The cut value indicated by the arrow is set at the position where the background distribution drops below the signal distribution.

The fourth cut is applied additionally for $\Lambda/\bar{\Lambda}$ candidates in order to reject background originating e.g. from pair conversions or split reconstructed VDS

segments that populate preferredly the region below $p_t \approx 0.05\ GeV/c$ in the Armenteros-Podolanski plot. Rather than cutting on the area below $p_t = 0.05\ GeV/c$ which would cause a significant loss of signal, it is possible to recover $\Lambda/\bar{\Lambda}$ candidates in that region by cutting on the product $p_t \cdot ct_0$ $(flgt)$. In figure 4.3 (b) the distribution of $p_t \cdot flgt$ for Λ candidates after applying the preselection cuts 1. and 2. is plotted for the 3 σ peak region of the Λ signal (histogram) and for the sidebands renormalised to the peak distribution (polymarkers). Again the cut was chosen at the position where signal and background start to be distinguishable.

As already stated before, K_s^0's are kinematically indistinguishable from $\Lambda/\bar{\Lambda}$ in the regions where the respective bands in the Armenteros-Podolanski plot overlap. In order to diminish systematic errors on the polarisation analysis introduced by K_s^0's, this background is minimised by the following two measures:

- To prevent an overlap of the K_s^0 band with the $\Lambda/\bar{\Lambda}$ bands, for all K_s^0 candidates the maximal momentum ratio of the decay tracks is chosen to be < 3.
- To remove K_s^0's that are kinematically indistinguishable from $\Lambda/\bar{\Lambda}$, all $\Lambda/\bar{\Lambda}$ candidates are removed that fulfil a K_s^0 mass hypothesis in the mass window $0.485\ GeV/c^2 < m_{K_s^0} < 0.515\ GeV/c^2$.

To illustrate above cuts, figure 4.4 shows their effect on the Armenteros-Podolanski plot. The loss of $\Lambda/\bar{\Lambda}$ signal due to the K_s^0 removal is about 10 %.

4.2 Track selection

For the V^0 reconstruction the most important ingredients are the vertex reconstruction and momentum determination. Taking into account only tracks containing at least a VDS segment, there are the following possible track compositions (neglecting the muon system and TRD):

1. VDS + MAIN + RICH + ECAL
2. VDS + MAIN + RICH
3. VDS + MAIN + ECAL
4. VDS + MAIN
5. VDS + RICH + ECAL

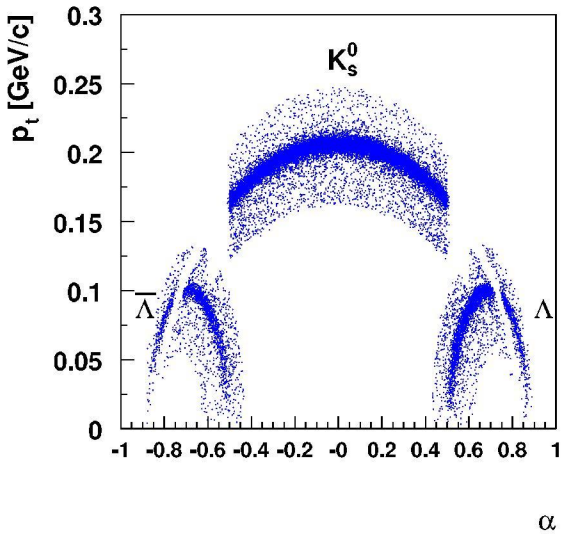

Figure 4.4: Armenteros-Podolanski plot for the minimum bias dataset after K^0_s-background removal.

6. VDS + RICH
7. VDS + ECAL
8. VDS only

The different track compositions will contribute to the V^0 signal with different efficiency. Especially tracks containing no information from the main tracking system might introduce considerable background to the desired signal due to increased ghost track contributions and lower matching efficiencies. Since `Cloneremove()`[4] being applied by the V^0 selection uses all track constitutions mentioned above, it is useful to check how the signal quality depends on the used track selection.

To study this effect, the V^0 selection described in the previous section was applied to the same set of tracks (run 14577, reprocessing 2) using different track selections.

In table 4.1 the outcome of these tests is shown: The first row shows the yield of V^0s using the described V^0 selection criteria and an outdated track selection widely used before completion of the `Cloneremove.C` function, which was replaced by `Cloneremove.C`, version1.2 in the second row. The

[4]See section 3.3.

	K_s^0	Λ	$\bar{\Lambda}$
Old track selection	2099 ± 47	387 ± 20	159 ± 13
`Cloneremove.C`, version1.2	2561 ± 56	415 ± 22	206 ± 17
Modified `Cloneremove.C`, version1.2	2244 ± 49	392 ± 21	175 ± 14

Table 4.1: V^0 yield for different track selection codes in a fixed data set (run 14577).

last row finally shows the result of using a modified clone removal, allowing only tracks having at least VDS and main tracker information to be used.

It is obvious that the yield of V^0s is improved by the usage of `Cloneremove.C` instead of the outdated track selection, leaving only the decision open *which* `Cloneremove.C` version should be used.

To illustrate the differences in the signal quality, figure 4.5 shows how the quality improves if tracks consisting of VDS only, VDS + ECAL and VDS + RICH + ECAL are removed in `Cloneremove.C`, version1.2: For plot (a) the signal / $\sqrt{background}$ is 49, whereas it is 101 for plot (b), where the above mentioned tracks are removed.

Because it was possible to reduce the background in the V^0s considerably by removing tracks as stated above and thus reduce necessary systematic corrections of the polarisation measurement, the modified `Cloneremove()` was used in this analysis ignoring those tracks. Since the matching between VDS and RICH was switched off in the track reconstruction, the removal of above track types is equivalent to require each track to have at least a VDS and a main tracker segment for optimal momentum information.

4.3 Reconstructed V^0 signals

Finally, the V^0 mass distributions obtained from the minimum bias dataset after applying all cuts mentioned in section 4.1 and using the track selection as stated in section 4.2 are shown in figure 4.6.

To each mass distribution a Gaussian plus a linear background has been fitted. The obtained signal width for the K_s^0 signal is 6 MeV/c^2, for the $\Lambda/\bar{\Lambda}$ it is about 2.2 MeV/c^2. For comparison purposes, the mass values of the particle data group (PDG) are shown as red lines in each plot. From the very good agreement in the mass positions it can be concluded that calibration and alignment of the HERA-B detector are well understood for this dataset. An overview of the signal statistics obtained in the minimum bias dataset compared to the MC dataset can be found in table 5.1.

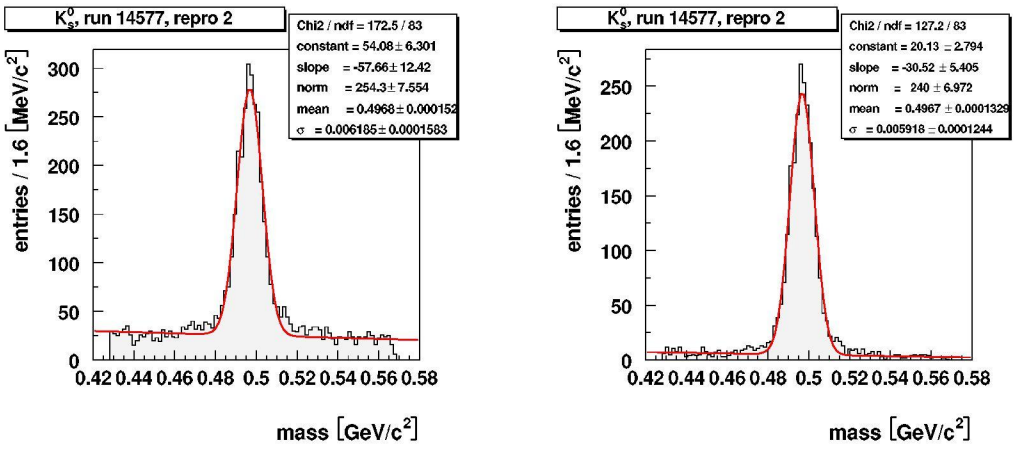

(a) (b)

Figure 4.5: (a): K^0_s signal using `Cloneremove()` V1.2 as track selection for the V^0 reconstruction, (b): K^0_s signal using `Cloneremove()` V1.2 *without* VDS only, VDS + ECAL and VDS + RICH + ECAL tracks for the V^0 reconstruction.

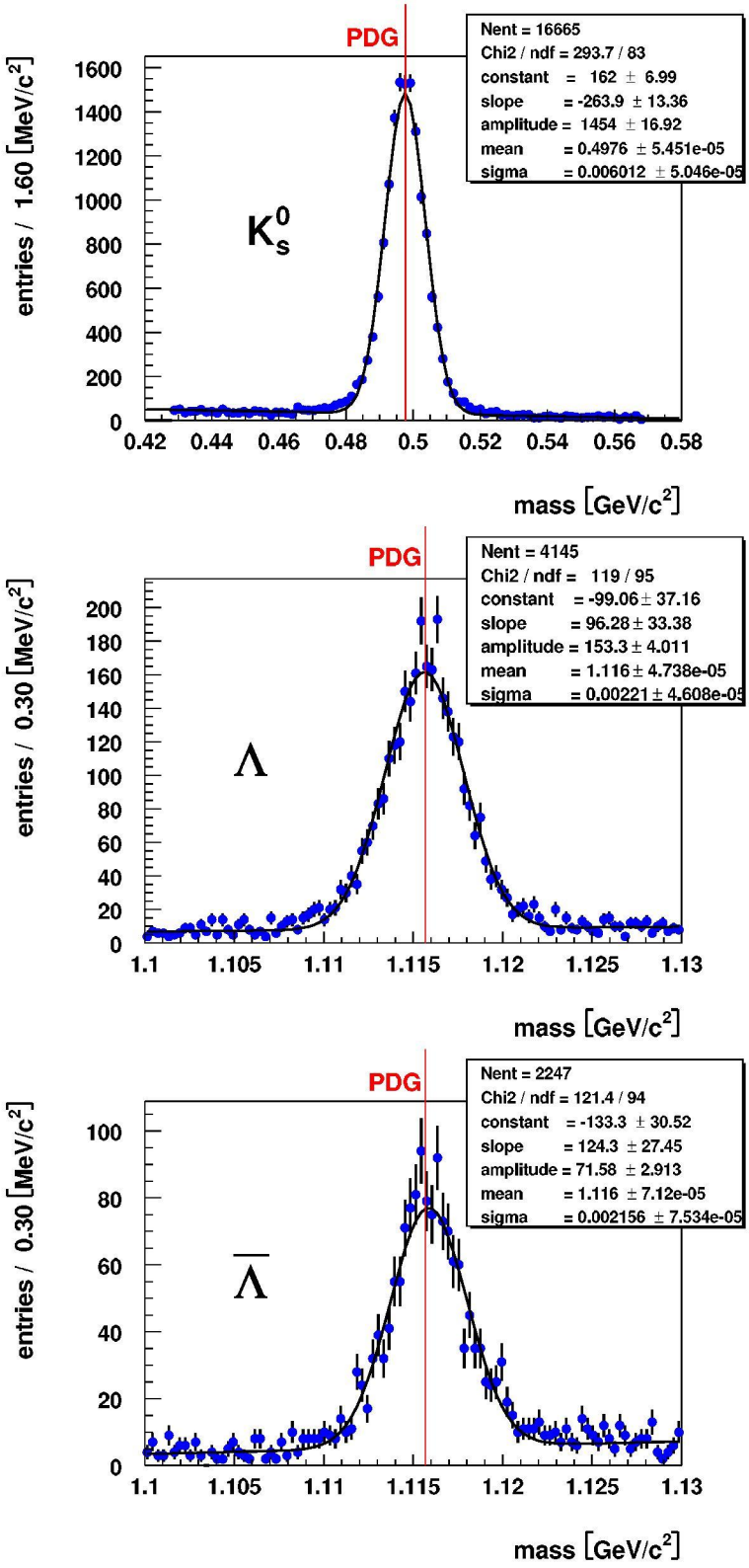

Figure 4.6: V^0 mass distributions in the minimum bias dataset after application of the cuts and track selection described in this chapter. To each mass distribution a Gaussian plus a linear background has been fitted.

Chapter 5

Acceptance determination

As already shown in section 1.5, to determine the Λ ($\bar{\Lambda}$) polarisation it is necessary to analyse the angular distributions of the decay (anti-) proton in the Λ ($\bar{\Lambda}$) rest frame. Since the measured angular distributions will be convoluted with the detector acceptance $A(\cos\ \vartheta_i)$ (see equation 1.12), the acceptance determination is a crucial point. In the analysis presented in this thesis, the acceptance of the HERA-B apparatus has been determined with Monte Carlo (MC) simulations: The angular distributions in the MC truth (before reconstruction) have been generated flatly, so the observed distortions after reconstruction will be due to the detector acceptance. To prove the validity of the detector simulation with respect to material budgets, resolutions, efficiencies, etc., additional observables have been checked with respect to the data.

This chapter will show how the Monte Carlo simulations were generated and how the reconstruction of the generated data was done. Possible sources for deviations between real data and simulation will be discussed in more detail since they might have a strong impact on the acceptance determination and thus the polarisation analysis.

5.1 Monte Carlo generation

The generation of Monte Carlo simulated events proceeds in two steps: First, event generators simulate all the particles that are produced in the primary interaction. After that, those particles are propagated through the simulated detector.

5.1.1 Event generation

The default event generators used for simulations at HERA-B are the PYTHIA and FRITIOF programs [Iva99]: The PYTHIA package, which uses internally the JETSET program for fragmentation of hadronic jets [Sjö94], is used to generate e.g. the heavy quarks of interest in a hard scattering process. Because PYTHIA is restricted to the collisions of nucleons and not able to simulate nuclear effects, the remaining energy of the event is then passed into the FRITIOF [Pi92] simulation package. FRITIOF, which is optimised for the treatment of nuclear environment like simulating energy loss and multiple scattering of partons traversing the target nucleus, is then generating the underlying event.

However, for the purpose of this analysis, the PYTHIA package was *not* used: The Λs and $\bar{\Lambda}$s were generated purely following the kinematic distribution described in equation 5.1 below. The remaining energy of the event was then passed to FRITIOF for the generation of the underlying event as a virtual π^+ as beam particle, following again the usual simulation scheme. Since the K_s^0's were generated by FRITIOF with sufficiently high statistics (see table 5.1), no dedicated K_s^0 sample was needed.

Assuming that x_F and p_t are independent variables to describe the V^0 kinematics, parametrising it in p_t^2 as experimentally observed and in x_F as described in [Gun79] and references therein, one yields the following distribution form:

$$\frac{d^2\sigma}{dp_t^2 dx_F} = C(1-x_F)^n \cdot exp(-Bp_t^2). \tag{5.1}$$

In order to adopt the generated kinematic distributions to the observed experimental data, the Λs and $\bar{\Lambda}$s were generated according to the above distribution with $n = 0$ (assuming a flat x_F distribution in the observed range) and $B = \frac{1}{<p_{t,\ data}^2>} \approx 2.1\ \frac{c^2}{GeV^2}$ with $< p_{t,\ data}^2 >$ being the observed mean value of the p_t^2 distribution in real V^0 data taken with HERA-B and other experiments.

Extensive consistency checks have successfully been performed with this way of Monte Carlo generation which are described in detail in [HB02] and references therein. The flatness of the angular distributions of the decay (anti-) proton in the Λ ($\bar{\Lambda}$) rest frame was also successfully checked which leads to the fact that the reconstructed Monte Carlo distributions can be directly used for acceptance corrections. All events were generated on the inner 2 carbon wire (see figure 2.3 (a)).

5.1.2 Detector simulation

The HERA-B detector simulation is performed within the HBGEAN [Now94] package based on GEANT [GEA94]. Here, the detector has to be exhaustively described with respect to geometrical shapes, positions, type and amount of material of all detector components in every detail.

All particles generated as described above are passed to HBGEAN propagating them through the simulated detector. Here they leave Monte Carlo impact points (MIMPs) in detector volumes sensitive to the particular particle, decay according to their specific lifetime and can encounter energy loss or multiple scattering according to the particle's momentum and crossed material. All relevant information is again stored in ARTE tables like the MIMPs (MIMP table), the tracks/particles (MTRA table) and the vertices (MVER table). Since the information stored in those tables is not affected by detector efficiencies and resolutions, it is also referred to as Monte Carlo truth.

For a proper simulation of the detector behaviour, of course those efficiencies and resolutions have to be taken into account as described in the next section.

5.2 Monte Carlo reconstruction

The crucial point for Monte Carlo reconstruction is the digitisation where the Monte Carlo truth is converted into information like the real detector would record it.

For example, MIMPs are (not) converted into hits according to the known efficiencies or dead channels of the respective sub-detector. Detector resolutions are included if needed by the smearing of hit positions according to Gaussian error distributions reflecting the known resolutions.

After digitisation, the event reconstruction chain for Monte Carlo and real data is identical and proceeds like described in section 3.2[1]. Figure 5.1 summarises again the commonnesses and differences for real data taking and Monte Carlo simulations. Since the finally filled structures are identical for both after reconstruction, the same analyses can be performed easily on both reconstructed data and Monte Carlo.

[1]Like for real data reconstruction, the used ARTE version was `ARTE-03-09-r3`, and also the used steering file (kumac) was based again on the rp3004 kumac (see section 3.2). The significant difference in the kumac is the usage of the geometry file that was also used for the Monte Carlo generation (`10_p10000.g0308r5-04.d991015.geo`) and the initialisation of the digitisation which used information optimised for the minimum bias period.

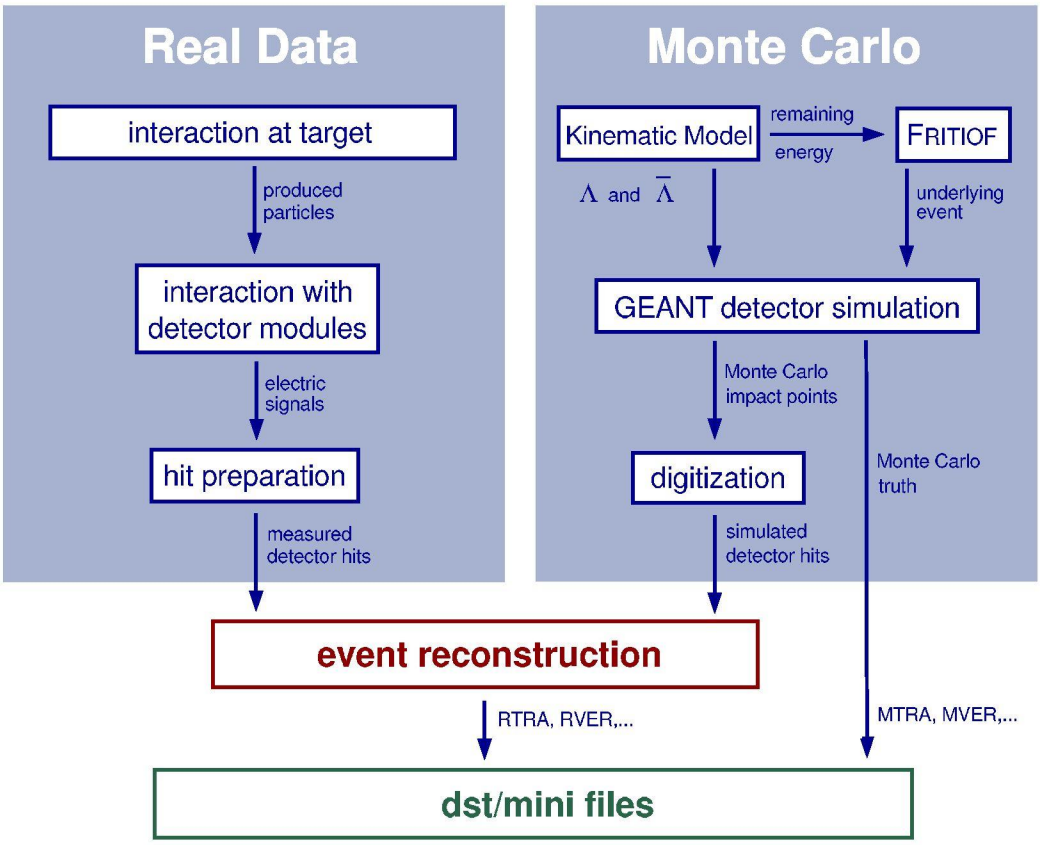

Figure 5.1: Comparison of real data taking and Monte Carlo simulations. The figure is based on [Aga01].

For the polarisation analysis, the goal to obtain a good detector acceptance description with the reconstructed Monte Carlo was being more complicated by the fact that the whole detector system was still being commissioned as stated already in section 2.6. Especially since the ITR was not fully operational during the minimum bias data taking, it had to be crosschecked that usage of this information would not corrupt the description of the main tracker in Monte Carlo and thus the acceptance determination. An effective means of checking whether the ITR is described correctly in Monte Carlo is to compare the distribution of inbending and outbending track pairs with real data:

Figure 5.2 illustrates that a proper variable to distinguish between in- and outbending tracks is the product of charge and x component of the momentum p_x which is positive for outbenders and negative for inbenders. The picture also illustrates the reconstruction of inbenders will rely much

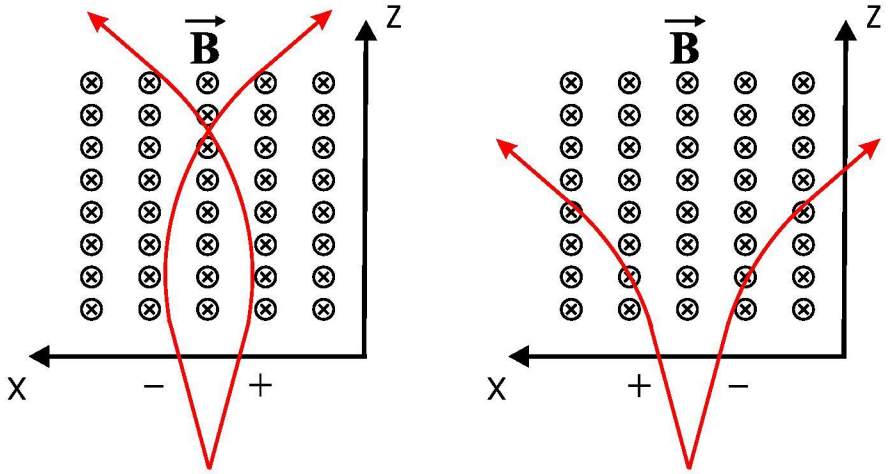

Figure 5.2: Properties of (a) in- and (b) outbending tracks in HERA-B: For inbenders charge · p_x is negative, for outbenders it is positive.

more on an efficient inner tracking area in HERA-B than the reconstruction of outbenders. In figure 5.3 the distribution of in- and outbenders for data and Monte Carlo normalised to the same integral is compared (a) before and (b) after removing the ITR information from reconstruction.

It is clearly visible that the efficiency of the ITR is overestimated in Monte Carlo, causing an excess of inbenders compared to real data. After removing the ITR information, the agreement between data and Monte Carlo is evident.

Table 5.1 summarises the obtained V^0 signal statistics for the minimum bias data and the produced Monte Carlo after removing the ITR from reconstruction, applying the V^0 selection as described in chapter 4. The overestimation of ITR efficiency in Monte Carlo becomes again evident in the signal loss due to ITR removal which is twice as high for simulated data than for real data. *For the reasons stated above, no ITR information was used for reconstruction in minimum bias data and Monte Carlo in this analysis.*

Having a look at the available statistics for the Λ polarisation analysis, one might think of using other datasets taken in the year 2000 additionally in order to increase statistics. This possibility was also checked for the Single Lepton dataset taken in August 2000 using a trigger on a single lepton with

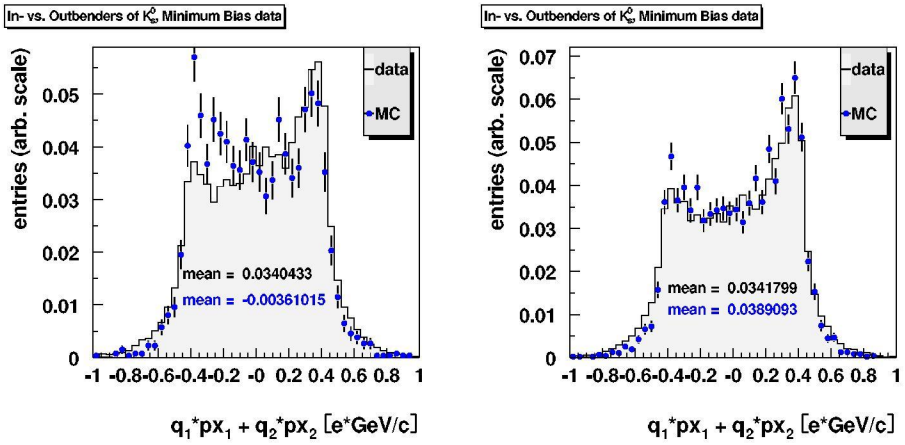

(a) (b)

Figure 5.3: Comparing in- and outbenders in MC and Data for K^0_s normalised to the same integral (a) before and (b) after removal of the ITR in the reconstruction.

Dataset	particle	signal	ITR-loss	source
DATA	K^0_s	13800	-15 %	Min Bias
	Λ	2900	-15 %	Min Bias
	$\bar{\Lambda}$	1350	-18 %	Min Bias
MC	K^0_s	3750	-29 %	FRITIOF
	Λ	3450	-26 %	KIN & FRITIOF
	$\bar{\Lambda}$	850	-38 %	KIN & FRITIOF

Table 5.1: V^0 statistics in the Monte Carlo and minimum bias datasets *after* removing ITR information for reconstruction. ITR-loss states the loss in statistics due to the ITR removal. KIN refers to the kinematic model applied for $\Lambda/\bar{\Lambda}$ generation as described in equation 5.1.

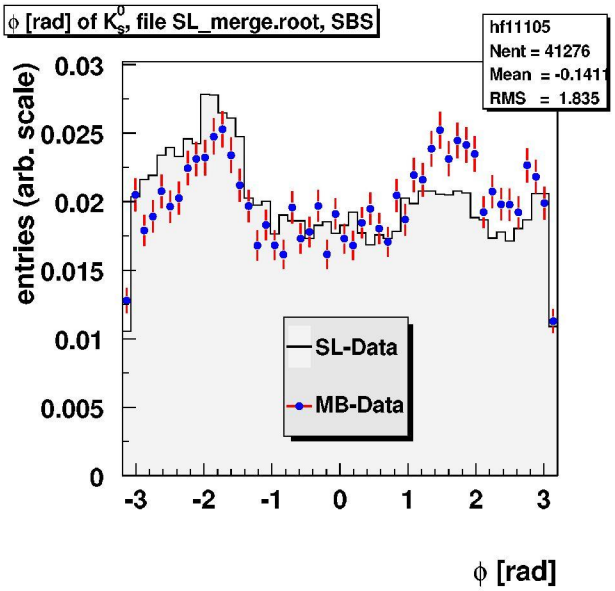

Figure 5.4: Comparison of the Φ distribution of K^0_s's for minimum bias (MB) and Single Lepton (SL) data after sideband subtraction (see chapter 6) normalised to the same integral.

high p_t ($p_t > 1\ GeV/c$)[2]. This dataset was also taken in a short time period such that effects of the detector commissioning on the data are expected to be small. Merging this dataset with the minimum bias data, a factor of 3.5 in statistics would have been gained.

Unfortunately, the detector had changed significantly between April and August 2000. For example, the OTR was losing channels continously due to shorts on the high voltage distribution boards. Comparing the Single Lepton and minimum bias data after identical reconstruction, it was easily visible that the detector had changed that much in between that a merging of the data would be far from trivial. As an example, in figure 5.4 the K^0_s azimuthal angle (Φ) distribution is shown for minimum bias (MB) and Single Lepton (SL) data normalised to the same integral.

The obvious differences would have also been quite time consuming to be implemented in Monte Carlo. Since in the year 2002 data taking, a larger data sample by a factor of 10-100 can easily be accumulated in a very short time period with much more stable running conditions, it was decided that the effort to merge Single Lepton and minimum bias data is too high compared to the gained statistics.

[2]A more detailed description can be found in [Aga01].

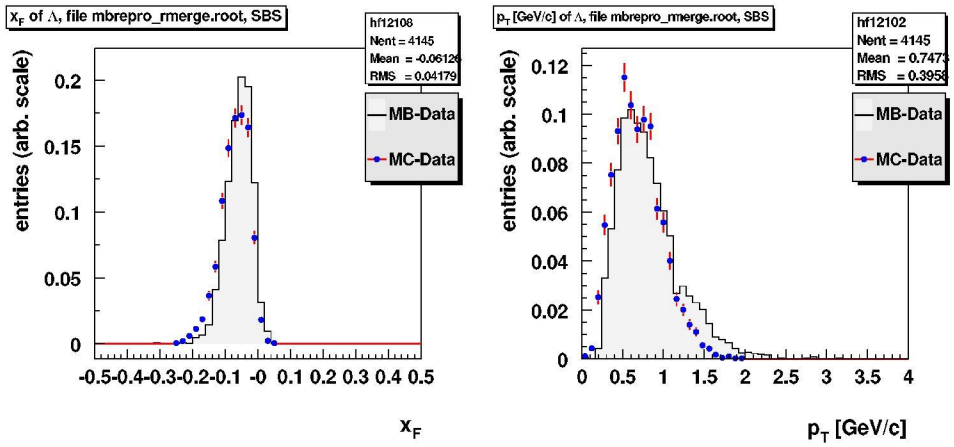

(a) (b)

Figure 5.5: (a) x_F and (b) p_t distributions for Λs in Monte Carlo (MC) and minimum bias (MB) data after sideband subtraction (see chapter 6) normalised to the same integral.

To make sure that Monte Carlo is in good agreement with real data, for all V^0s many distributions like θ, Φ, p_t, x_F, $mass$, $p_z, flightpath, \ldots$ were compared with real data, and reasonable agreement was found as shown in appendix A. The widths of the mass peaks were found to be smaller in reconstructed Monte Carlo compared to real data showing that still some more knowledge about the detector needs to be implemented in Monte Carlo: The width in Monte Carlo is $\approx$ 77 %, $\approx$ 81 % and $\approx$ 75 % of that in data, for K^0_s, Λ and $\bar{\Lambda}$ respectively.

Of special importance, however, are the x_F and p_t distributions on which the polarisation to be measured depends. Figure 5.5 shows the comparison between minimum bias data and Monte Carlo for Λs in x_F and p_t normalised to the same integral.

The discrepancy of the shapes between data and Monte Carlo in the x_F distribution shows that it is obviously not flat as it was generated using the kinematical model stated in equation 5.1. This approach was only chosen because no model was available in the kinematic region of HERA-B. Using the reconstructed x_F distribution in Monte Carlo normalised to the integral of the data distribution as acceptance correction for the data and sideband subtraction for both distributions, the resulting distribution can be fitted with a parametrisation $k \cdot (1 - |x_F|)^c$. Figure 5.6 shows the result of the fit

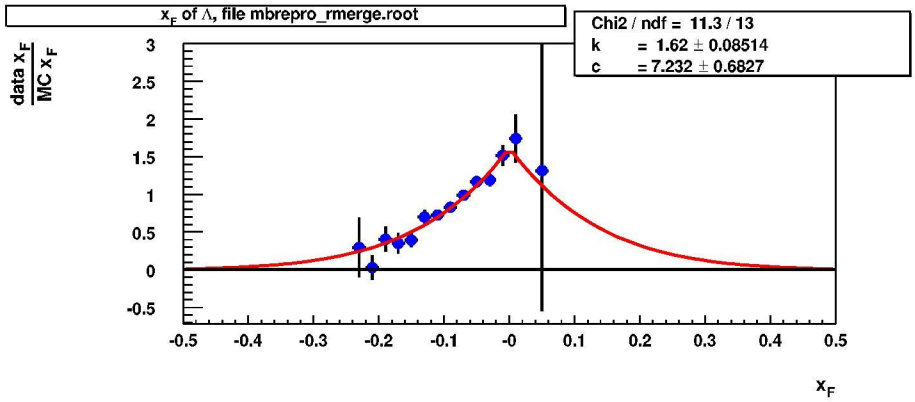

Figure 5.6: Parametrisation of the acceptance corrected x_F distribution for Λs after sideband subtraction (see chapter 6): The result of the fit using $k \cdot (1 - |x_F|)^c$ as fit function is shown as red line with the corresponding parameters in the fit box.

yielding a value of 7.23 ± 0.68 for c.

The effect of this discrepancy on the polarisation analysis can be estimated by reweighting the Monte Carlo in x_F with respect to the minimum bias data and using the observed difference in the polarisation result to obtain a systematic error.

A more striking difference between data and simulation occurs in p_t above $\approx 1.2\ GeV/c$ (figure 5.5(b)): Here, a bump where the data are significantly above the simulation, is visible.

Having a closer look at the p_t^2 distributions of Λs in data and Monte Carlo, the source of the difference becomes obvious (see figure 5.7 (a)): In the data, a kink occurs in the p_t^2 distribution, making it necessary to fit two exponentials instead of one, whereas Monte Carlo can be described by just fitting one exponential. Figure 5.7 (b) shows that the effect observed in our data is a well-known fact also to other experiments: The p_t^2 distributions of different hyperons also show a kink occurring around $1.2\ GeV^2/c^2$, being observed by the WA89 experiment using a 320 GeV Σ^- beam on a Cu target [Zav02]. It follows that this well established experimental fact is obviously not described properly in the Monte Carlo used for this analysis, as can be understood easily regarding the simple kinematic model used so far (see equation 5.1).

To estimate the systematic error introduced by this deviation, the polarisation calculated from the full data sample will be compared to the value obtained from the subsample below a p_t of $\sqrt{1.2}\ GeV/c \approx 1.1\ GeV/c$.

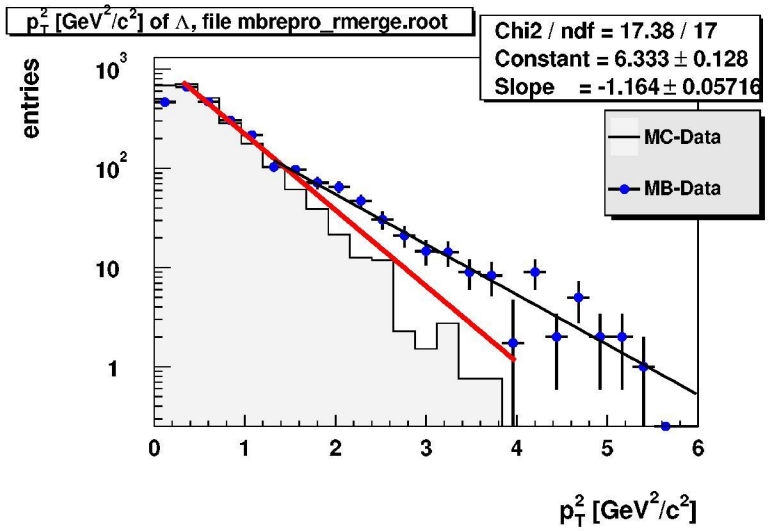

(a)

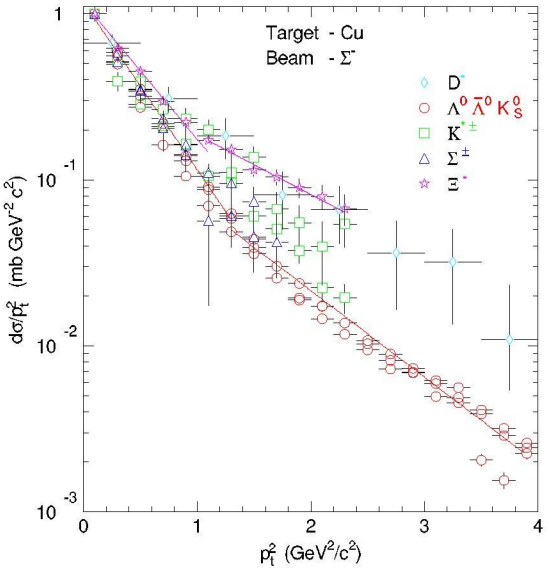

(b)

Figure 5.7: Discrepancy between data and MC in p_t^2: (a) shows that *two* slopes are necessary to fit the data, whereas the first slope is enough to describe the Monte Carlo distribution (rescaled with respect to data). The result of the fit for the black line is shown in the fit box. (b) shows the p_t^2 distributions for K_s^0 and different hyperons in WA89 [Zav02]: Also here two slopes are necessary to describe the data.

Chapter 6

Polarisation analysis

This chapter will explain how the actual polarisation analysis is carried out. The necessary steps prior to this are the reconstruction of data and Monte Carlo, checking the agreement between real data and Monte Carlo detector description and finally the reconstruction of V^0s, which have been explained in the previous chapters.

The polarisation analysis proceeds as follows:

1. For both minimum bias data and Monte Carlo, the mass distributions for all V^0 signals are filled. To each distribution, a linear background and a Gaussian signal is fitted. From the obtained width σ, a peak and a sideband region is defined using a value of 3 σ from the found peak position as limit.

2. For each V^0 signal, different distributions of interest like Φ, θ, x_f, $p_t, \ldots$ *and* the angular distributions of the decay p, $\bar{p}$, π^+ of Λ, $\bar{\Lambda}$, K_s^0 (see section 1.5) are filled separately for peak and sideband region defined in the first step.

3. The sideband distributions are rescaled with respect to the integral over the linear background in the peak region fitted in the first step.

4. If a weighted filling of all distributions with respect to any variable of interest (e.g. x_F) is desired, for that variable the rescaled sideband distribution is subtracted from the peak distribution (sideband subtraction, see figure 6.1) both in data and Monte Carlo. The resulting distributions are divided by each other to obtain a weight factor for each bin of the variable to be weighted for. By this, the Monte Carlo can be adopted to real data for any distribution of interest.

5. To obtain all distributions weighted with respect to the variable of interest, the steps 2. and 3. are repeated using the weights calculated in 4..

6. Finally, the polarisation for all three V^0 signals in all three directions is evaluated using either the unweighted or the weighted angular distributions: First, a sideband subtraction is done both for data and Monte Carlo distributions. To get rid of acceptance effects, the obtained distributions are divided by each other. Finally, a straight line fit is applied to all acceptance corrected distributions, with the slope being $\alpha \cdot polarisation$. The polarisation values are then obtained using $\alpha_{K^0_s} = 1,\ \alpha_\Lambda = 0.642,\ \alpha_{\bar{\Lambda}} = -0.642$.

Figure 6.1 illustrates again the concept of sideband subtraction used in the analysis: Assuming that the background in the peak region (drawn in blue) is identical to that in the sidebands (shown in red), the background under the

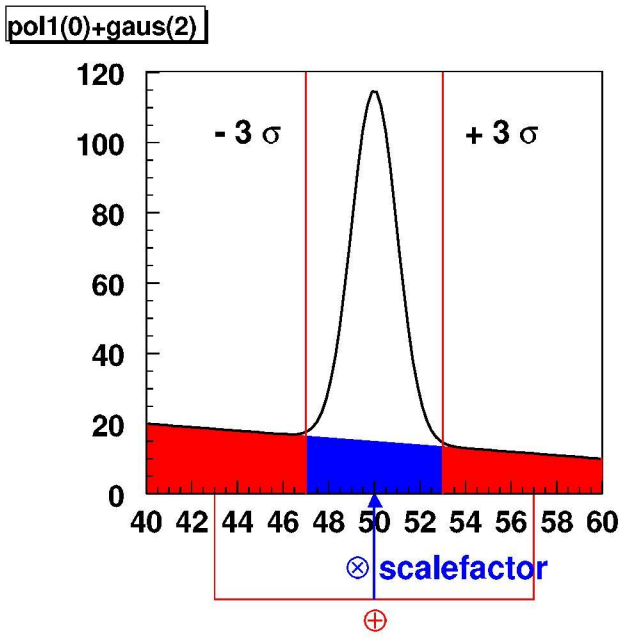

Figure 6.1: Illustration of sideband subtraction: The sideband regions beyond 3 σ are shown as red areas; the corresponding background under the signal is shown in blue. Assuming identical behaviour of background in peak and sideband region, the rescaled sidebands can be used to estimate the background in the central region.

peak can be subtracted by using the distribution in the sidebands rescaled with respect to the expected integral of the background under the peak.

The result of the polarisation analysis for K_s^0, Λ and $\bar{\Lambda}$ using the unweighted angular distributions is shown in figures 6.2 - 6.4: The figures (a) & (b), (c) & (d) and (e) & (f) show the overlayed angular distributions for minimum bias data and Monte Carlo rescaled to the same integral and the data distribution divided by the simulation with a straight line fit applied for x, y and z direction respectively.

Because the kinematics of the decay products for Λ and $\bar{\Lambda}$ is the same, also the angular distributions for the decay proton and anti proton look very similar. The dip in z direction for both Λ and $\bar{\Lambda}$ results from the removal of K_s^0 candidates from the samples. The negative slope of this distribution introducing an asymmetry between positive and negative cos θ_z can be understood in the following way: A positive cos θ_z means that the (anti) proton is flying in the direction of the Λ ($\bar{\Lambda}$), i.e. the direction of the boost. That is equivalent to the π^- (π^+) being emitted opposite to the boost direction, resulting in a very soft track that will fall below the reconstruction threshold with a probability increasing with increasing positive cos θ_z.

The differences in V^0 kinematics between minimum bias data and Monte Carlo in x_F and p_t as described in the previous chapter will mainly influence the z related angular distributions since z points to the direction of the reconstructed V^0 momentum. Accordingly, the largest deviations from zero are expected to occur in cos θ_z, as actually observed. A mapping of x_F versus p_t to correct for the observed deviations is not possible due to the limited statistics. To illustrate how the result in z is depending on the kinematics, in table 6.1 the polarisation results are shown additionally using x_F weighting for Λ and $\bar{\Lambda}$, where deviations in x_F are obvious as shown in appendix A[1]. The results in z are closer to zero after x_F weighting as expected.

The used kinematical model as stated in equation 5.1 certainly has some room for improvement, but since the kinematics in the range of HERA-B are not known, it provides only a first estimate. Provided sufficient statistics in data and Monte Carlo, the observed deviations could be used to draw conclusions about the real underlying kinematics at HERA-B.

Since the y coordinate is more independent from the kinematics, the respective results are more important as consistency crosscheck, and good agreement with zero is found. A detailed discussion of systematic errors on the polarisation measurement that could arise from the observed deviations in x_F and p_t will follow in the next chapter.

[1]For the K_s^0 signal, the deviations in x_F are only marginal as can be seen in appendix A, thus also the effect of the weighting is marginal.

The angular distributions of the K_s^0 are finally expected to be symmetrically around zero, since the kinematics of the decay products is - in contrast to Λ and $\bar{\Lambda}$ - completely symmetric, which is also observed. The restricted range of the cos θ_z distribution ($|\cos\ \theta_z| \lessapprox 0.7$) is due to the cut on the momentum ratio for K_s^0 candidates (see chapter 4).

Table 6.1 summarises the results obtained from the straight line fits after the correction for the respective α factor.

particle	direction	polarisation	σ polarisation	$\frac{polarisation}{\sigma\ polarisation}$
K_s^0	x	-0.001	0.026	-0.023
	y	-0.011	0.031	-0.358
	z	-0.087	0.057	-1.514
Λ	x	0.073	0.073	1.001
	x (weighted)	0.074	0.072	1.032
	y	-0.076	0.084	-0.905
	y (weighted)	-0.084	0.084	-0.998
	z	0.129	0.076	1.689
	z (weighted)	-0.006	0.078	-0.083
$\bar{\Lambda}$	x	0.006	0.129	0.047
	x (weighted)	-0.070	0.129	-0.539
	y	0.006	0.144	0.042
	y (weighted)	0.046	0.147	0.316
	z	-0.238	0.141	-1.693
	z (weighted)	0.069	0.147	0.467

Table 6.1: Polarisation values with statistical errors for all V^0 signals and directions. For Λ and $\bar{\Lambda}$, additionally the results using x_F weighting are shown. Note that the polarisation measurement refers to the x direction of Λ and $\bar{\Lambda}$.

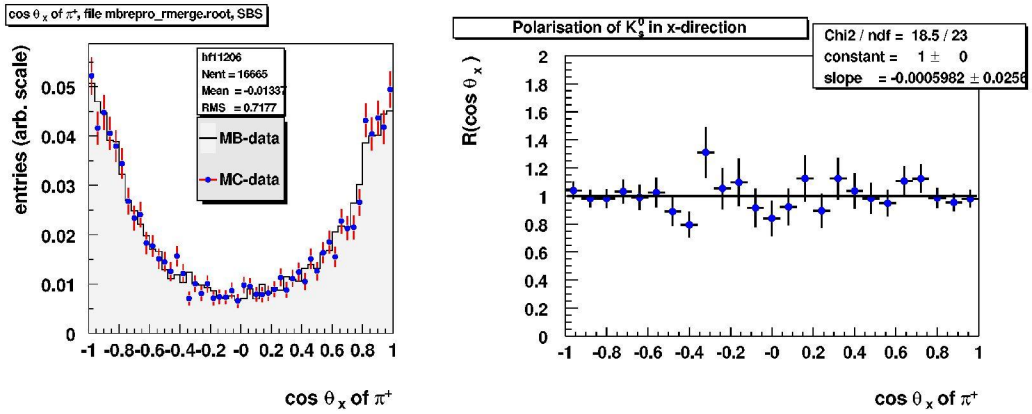

(a)

(b)

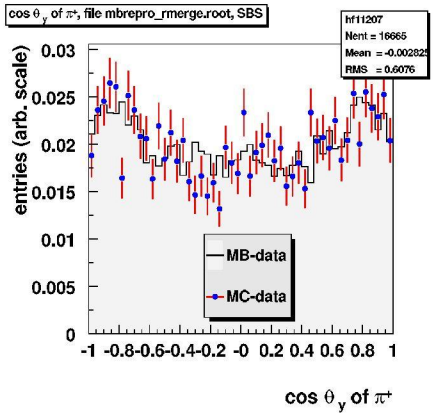

(c)

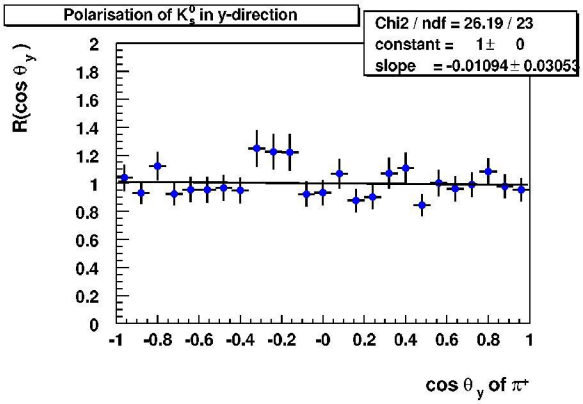

(d)

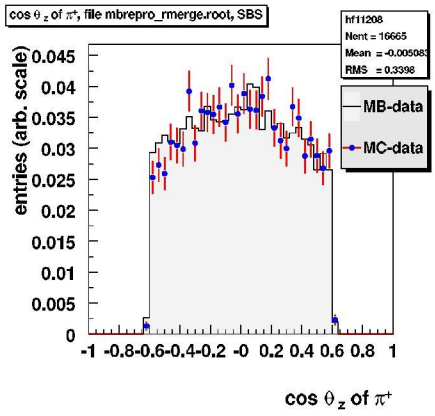

(e)

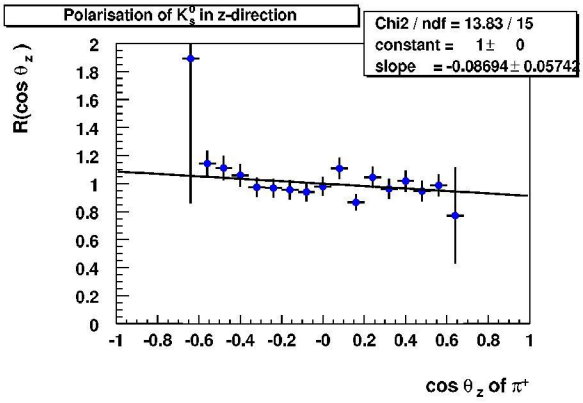

(f)

Figure 6.2: Unweighted angular distributions in data and Monte Carlo (rescaled to the same integral) after sideband subtraction and result of the linear fits after acceptance correction for the K_s^0 signal for x, y and z direction.

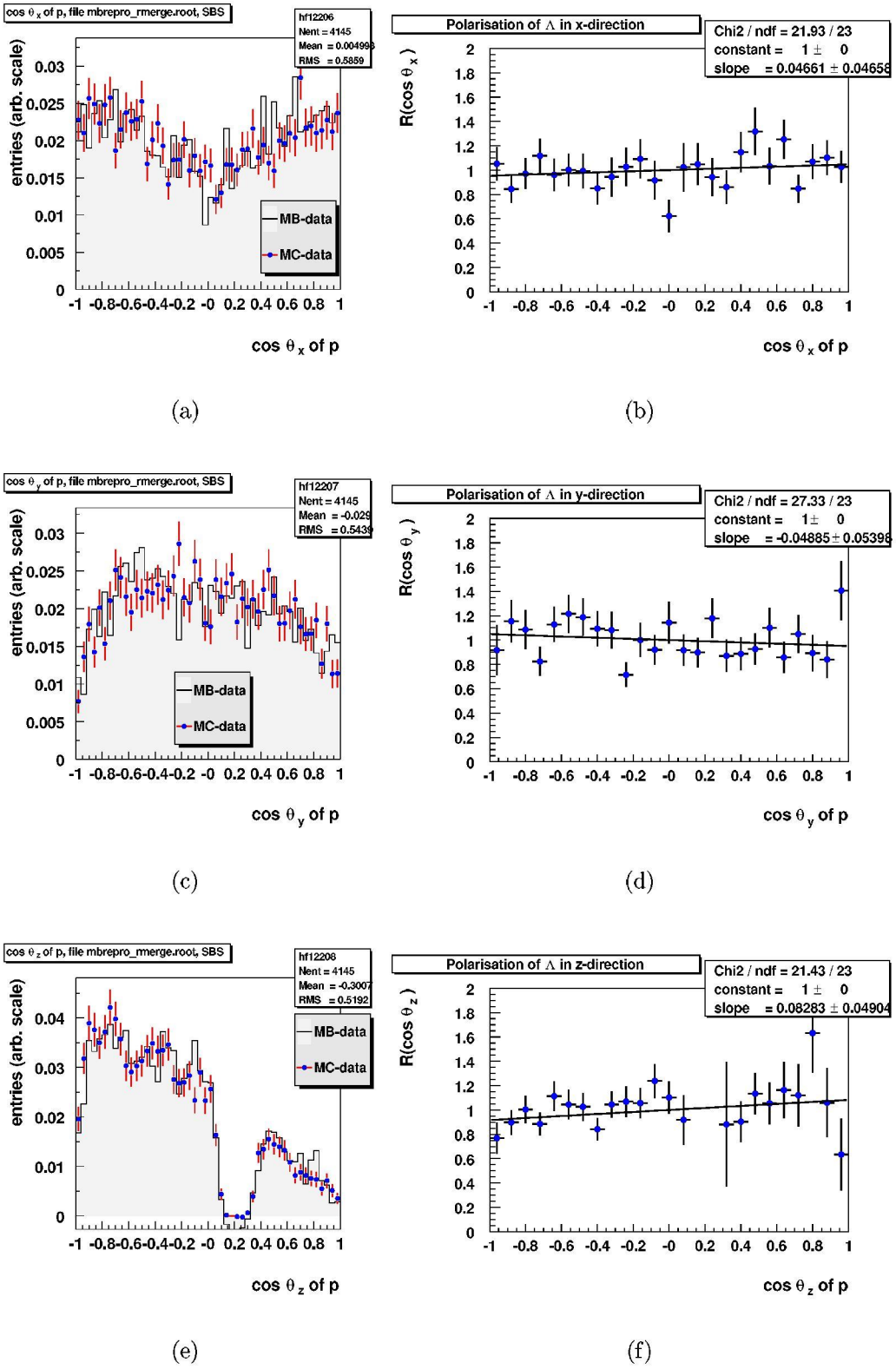

Figure 6.3: Unweighted angular distributions in data and Monte Carlo (rescaled to the same integral) after sideband subtraction and result of the linear fits after acceptance correction for the Λ signal for x, y and z direction.

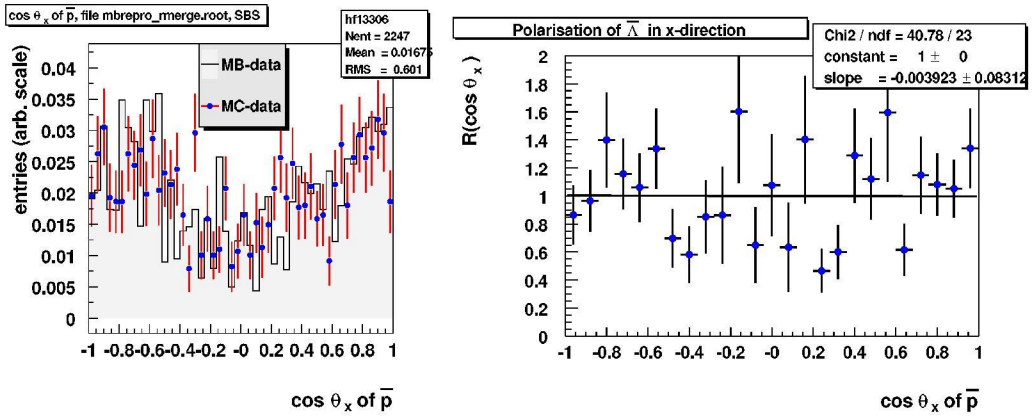

(a)

(b)

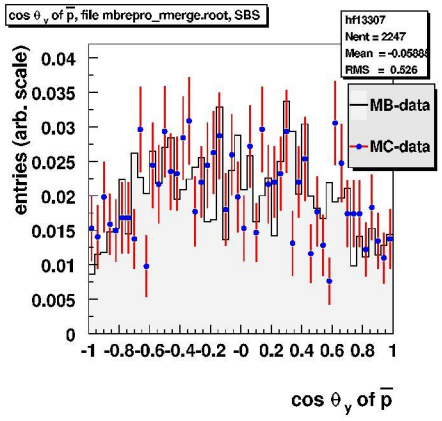

(c)

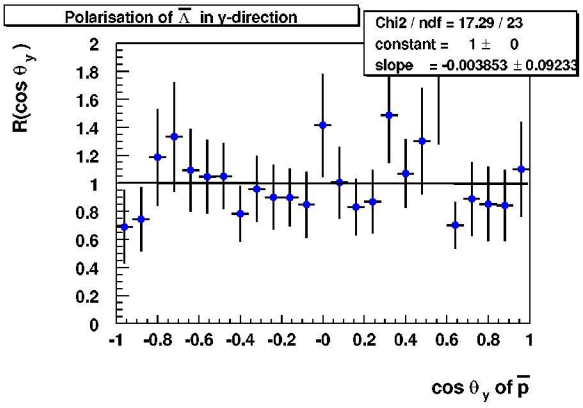

(d)

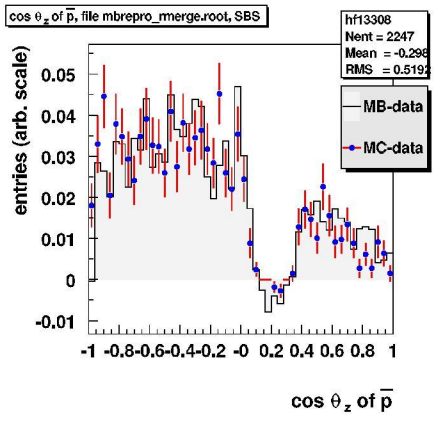

(e)

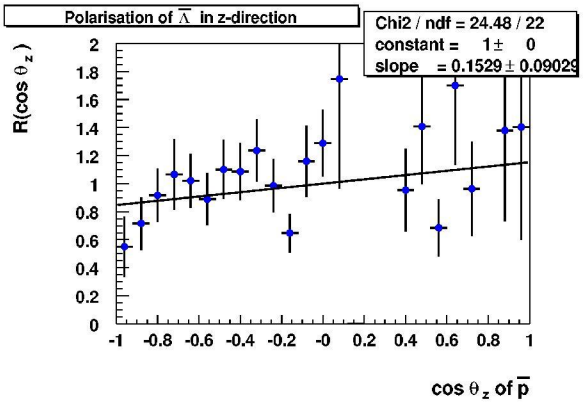

(f)

Figure 6.4: Unweighted angular distributions in data and Monte Carlo (rescaled to the same integral) after sideband subtraction and result of the linear fits after acceptance correction for the $\bar{\Lambda}$ signal for x, y and z direction.

Chapter 7

Systematic errors

This chapter will discuss the influence of inherent biases of the presented analysis method on the results presented in the last chapter.

For simplicity reasons, the term "polarisation" will be also used for the K_s^0 even though it has no spin. In this case, the result of the linear fit to the acceptance corrected angular distribution will be quoted, corresponding to the polarisation analysis using $\alpha_{K_s^0} = 1$.

Since all calculations have been performed using the full available precision whereas fewer digits are shown in the tables, rounding effects may occur for the presented results compared to the underlying values shown in the tables.

7.1 Beam movement

The HERA proton beam enters HERA-B inclined with respect to the z coordinate of HERA-B's coordinate system with a slight tilt in x direction to compensate for the momentum kick the protons encounter in the HERA-B magnet. The nominal value for the beam tilt corresponds to a rotation of 0.6887 *mrad* around the y axis of HERA-B's coordinate system[1].

Since this beam tilt was simulated in Monte Carlo with the nominal value, whereas for the real data beam movements may occur, it has to be checked whether those deviations have any impact on the polarisation values to be obtained, keeping in mind that the beam direction directly enters into the definition of the reaction plane. For that purpose, the polarisation analysis was performed keeping the beam direction for Monte Carlo data fixed to the nominal value and varying the x direction of the beam in 200 MeV/c

[1]This yields a momentum vector of $(-0.6336, 0, 919.9998)$ GeV/c for each incoming proton.

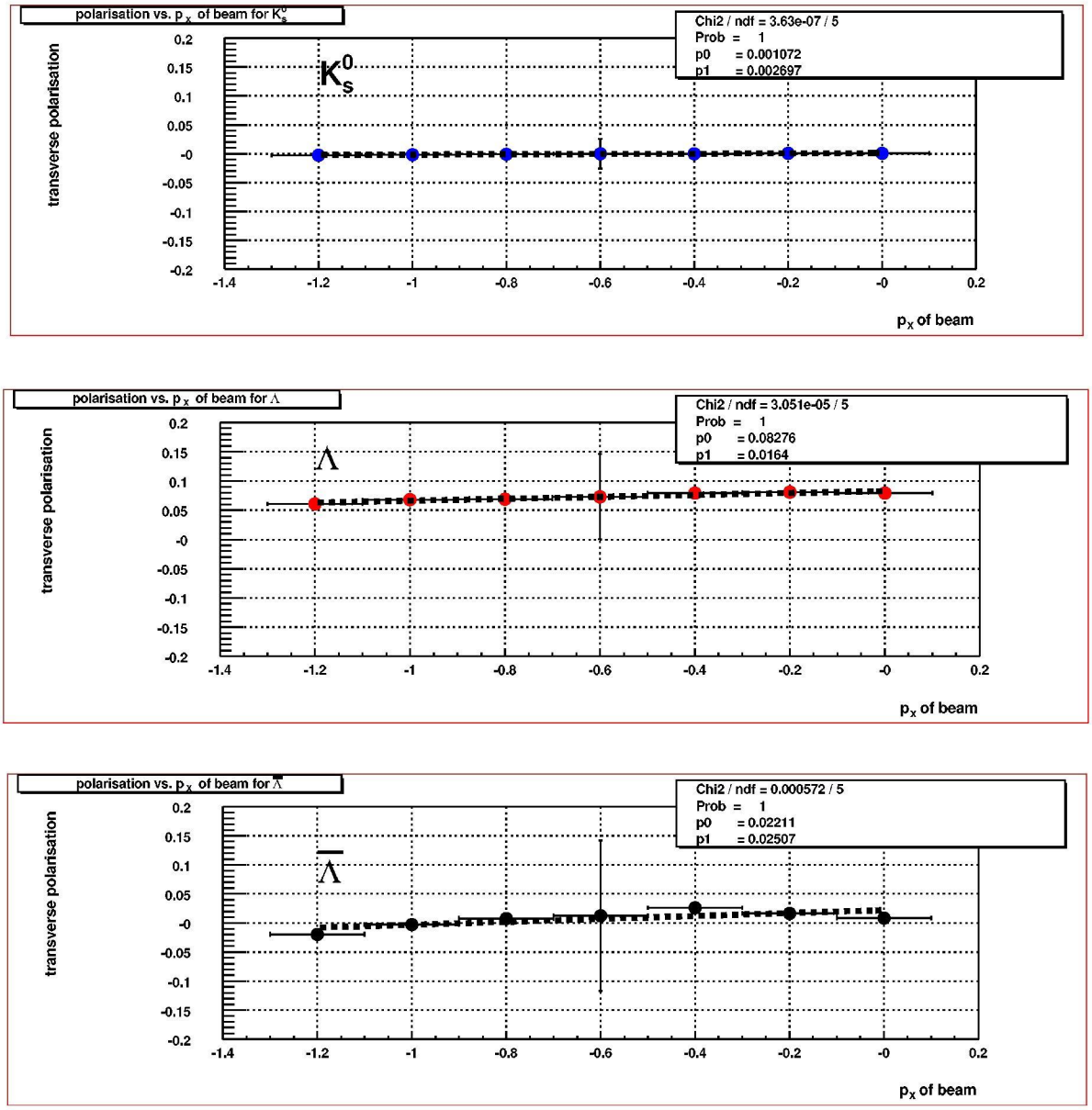

Figure 7.1: Effect of beam movement on polarisation results for all V^0 signals. The outcome of the straight line fit is shown as dashed line with the fit parameters indicated in the fit box. Since always the same data were analysed, the errors on the polarisation will be completely correlated. Because of this, only one polarisation error is drawn for each V^0. p_x of the beam is displayed in GeV/c.

steps from 0 to 1.2 GeV/c for the data, corresponding to a beam movement of 100 % around its nominal value. The resulting transverse polarisations versus the x component of the beam momentum are shown in figure 7.1 for all V^0s with a linear fit applied to each diagram.

To estimate the effect of beam movement on the polarisation measurement, we assume a beam deviation from the nominal value of 50 %:

$$\begin{aligned} K_s^0: \ \sigma_{beam}^{syst} &= 0.0027 \cdot 0.6336 \cdot 0.5 \approx 0.0009 \\ \Lambda: \ \sigma_{beam}^{syst} &= 0.0164 \cdot 0.6336 \cdot 0.5 \approx 0.0052 \\ \bar{\Lambda}: \ \sigma_{beam}^{syst} &= 0.0251 \cdot 0.6336 \cdot 0.5 \approx 0.0079. \end{aligned}$$

It is obvious that the changes to the polarisations due to beam movement are negligible. To illustrate this, the biggest increase of the total error occurs for the $\bar{\Lambda}$ transverse polarisation, where it is still on the per mill level if the systematic error due to beam movement is accounted for:

$$\begin{aligned} \sigma_{\bar{\Lambda}}^{tot} &= \sqrt{(\sigma_{\bar{\Lambda}}^{stat})^2 + (\sigma_{beam}^{syst})^2} \\ &= \sqrt{0.129464^2 + 0.007942^2} \approx 0.129707 \\ &\approx 1.002 \cdot \sigma_{\bar{\Lambda}}^{stat}. \end{aligned}$$

The derived systematic errors due to beam movement will be used for the calculation of the total errors for the sake of completeness.

7.2 Error on α

For the polarisation values stated in the last chapter, the errors cited were just the errors on the slope of the straight line fit to the acceptance corrected angular distributions using the measured decay asymmetry parameters for $\Lambda/\bar{\Lambda}$ as constants. Taking additionally into account the error on the measured $\alpha = 0.642 \pm 0.013$ [Gro00], the relative error of the polarisation changes as follows:

$$\frac{\sigma^{pol}}{pol} = \frac{\sigma^{slope}}{slope} \ \Rightarrow \ \frac{\sigma^{pol}}{pol} = \sqrt{\left(\frac{\sigma^{slope}}{slope}\right)^2 + \left(\frac{\sigma^{\alpha}}{\alpha}\right)^2}.$$

Calculating the polarisation errors using the error on α, one yields in the x direction for Λ and $\bar{\Lambda}$:

$$\begin{aligned} \frac{\sigma_{\Lambda}^{pol}}{pol_{\Lambda}} &= 1.00021 \cdot \frac{\sigma_{\Lambda}^{slope}}{slope_{\Lambda}} \\ \frac{\sigma_{\bar{\Lambda}}^{pol}}{pol_{\bar{\Lambda}}} &= 1.00000 \cdot \frac{\sigma_{\bar{\Lambda}}^{slope}}{slope_{\bar{\Lambda}}}. \end{aligned}$$

particle	$polarisation_{nocut}$	$polarisation_{cut}$	$pol_{cut} - pol_{nocut}$	$\sqrt{(\sigma^{pol}_{cut})^2 - (\sigma^{pol}_{nocut})^2}$
K^0_s	-0.001 $\pm$ 0.026	-0.002 $\pm$ 0.026	-0.0010	0.0056
Λ	0.073 $\pm$ 0.073	0.042 $\pm$ 0.079	-0.0302	0.0310
$\bar{\Lambda}$	0.006 $\pm$ 0.129	0.077 $\pm$ 0.136	0.0714	0.0401

Table 7.1: Results for the *transverse* polarisation measurement before and after cutting on $p_t < 1.1\ GeV/c$ for all V^0 signals.

Obviously, the error is completely dominated by the statistics. The calculation of a systematic error σ^{syst}_{α} only gives a mentionable value for the Λ and will again only be used in the final error calculation for completeness:

$$\Lambda: \ \sigma^{syst}_{\alpha} = pol \cdot \frac{\sigma^{\alpha}}{\alpha} \approx 0.0015$$
$$\bar{\Lambda}: \ \sigma^{syst}_{\alpha} = pol \cdot \frac{\sigma^{\alpha}}{\alpha} \approx 0.0001.$$

7.3 Error due to p_t description in Monte Carlo

As already stated in section 5.2, the Monte Carlo simulation does not describe the behaviour of the data in p_t properly in the range above 1.1 GeV/c. To estimate the systematic error introduced by this, the polarisation analysis was repeated on the p_t subsample in data and Monte Carlo below 1.1 GeV/c. The signal loss due to the cut is roughly 8 % for K^0_s, 19 % for Λ and 14 % for $\bar{\Lambda}$.

Table 7.1 shows how the values for the transverse polarisation are changed by this cut: Clearly, the values before and after cutting are compatible with each other. Also the statistical significance of the removed sample is comparable to the value of the possible bias.

Since the usage of above information for a systematic error $\sigma^{syst}_{p_t}$ is unfavourable due to the implied further reduction of available statistics, this error is determined in the following way:

The Monte Carlo was reweighted with respect to p_t of the minimum bias data, removing all events having a zero weight in Monte Carlo and minimum bias data also in the unweighted polarisation analysis to see the pure effect of the weighting. The results shown in table 7.2 finally yield the systematic errors $\sigma^{syst}_{p_t}$ for all V^0s using the absolute values of the deviations due to the

particle	$polarisation_{noweighting}$	$polarisation_{weighting}$	$pol_{weight} - pol_{noweight}$
K^0_s	-0.0002 ± 0.0257	-0.0018 ± 0.0260	-0.0016
Λ	0.0755 ± 0.0728	0.0711 ± 0.0738	-0.0044
$\bar{\Lambda}$	0.0267 ± 0.1280	0.0284 ± 0.1302	0.0017

Table 7.2: Results for the *transverse* polarisation measurement before and after p_t weighting of Monte Carlo with respect to the data for all V^0 signals.

p_t weighting:

$$K^0_s: \ \sigma^{syst}_{p_t} = 0.0016$$
$$\Lambda: \ \sigma^{syst}_{p_t} = 0.0044$$
$$\bar{\Lambda}: \ \sigma^{syst}_{p_t} = 0.0017.$$

Again, the errors are found to be very small compared to the statistical errors.

7.4 Error due to x_F description in Monte Carlo

To check the effect of the deviations between real data and simulation in x_F on the polarisation results, the Monte Carlo simulation was reweighted with respect to x_F of the minimum bias data. To see the pure effect of the weighting, all events having a zero weight were skipped in Monte Carlo and minimum bias data also in the unweighted polarisation analysis.

The observed larger effect of the weighting on the $\bar{\Lambda}$ transverse polarisation compared to the Λ corresponds to the bigger deviations between data and simulation for $\bar{\Lambda}$ as shown in appendix A.

As stated there, one major difference between the Λ and $\bar{\Lambda}$ sample is the enhanced fraction of FRITIOF generated $\bar{\Lambda}$s in the $\bar{\Lambda}$ sample, having different kinematical properties than the model stated in equation 5.1. Additionally,

particle	$polarisation_{noweighting}$	$polarisation_{weighting}$	$pol_{weight} - pol_{noweight}$
K^0_s	-0.0008 ± 0.0256	-0.0003 ± 0.0256	0.0004
Λ	0.0806 ± 0.0725	0.0741 ± 0.0718	-0.0065
$\bar{\Lambda}$	-0.0323 ± 0.1280	-0.0696 ± 0.1291	-0.0372

Table 7.3: Results for the *transverse* polarisation measurement before and after x_F weighting of Monte Carlo with respect to the data for all V^0 signals.

the observed bigger effect of x_F weighting could be an indication for the fact that using a flat x_F distribution in the kinematical model is more problematic for $\bar{\Lambda}$ than for Λ as it might be expected due to leading particle effects.

Using the symmetrised deviations due to the x_F weighting (see table 7.3) as systematic errors, one gets:

$$\begin{aligned} K_s^0: \ \sigma_{x_F}^{syst} &= 0.0004 \\ \Lambda: \ \sigma_{x_F}^{syst} &= 0.0065 \\ \bar{\Lambda}: \ \sigma_{x_F}^{syst} &= 0.0372. \end{aligned}$$

7.5 Background sources

The most prominent sources for secondary Λs ($\bar{\Lambda}$s) are Σ^0s and Ξ^0s/Ξ^-s/Ω^-s with their respective antiparticles:

- The Ξ^0 decays predominantly into $\Lambda\ \pi^0$ with a $c\tau$ of 8.71 *cm* [Gro00]. Since the Λs originating from Ξ^0s will, in general, not point back to the primary vertex, the cut on the impact parameter used in the V^0 selection discussed in section 4.1 will already discard most of this background.
  Analogue arguments hold for the $\Xi^- \rightarrow \Lambda\pi^-$ and the $\Omega^- \rightarrow \Lambda K^-$ with a $c\tau$ of 4.91 *cm* and 2.46 *cm* respectively.

- The Σ^0s decay predominantly into $\Lambda\gamma$ with a $c\tau$ of $2.22 \cdot 10^{-11} m$ [Gro00]. The short lifetime makes a cut on the impact parameter to discard Λs originating from Σ^0s useless. Since those Λs are hard to be disentangled from the ones coming from the primary vertex, Λ polarisation measurements *usually account for both channels inclusively.*
  To correct for the contamination due to Σ^0s, their fraction in the dataset and the polarisation of those indirect Λs need to be known. For the latter, theoretical models have to be applied. In general, the polarisation of direct Λs is expected to be greater than the measured value [Fan99, Hel85, And79].

Using FRITIOF simulations, the fraction of Λs ($\bar{\Lambda}$s) coming from $\Xi^0/\Xi^-/\Omega^-$ and their antiparticles was estimated to be ≈ 10 %. After application of the standard V^0 selection cuts, this fraction is reduced to ≈ 1 % [San02b]. The impact of this remaining fraction is negligible considering additionally the convolution of the respective decay asymmetry parameters into a possible distortion of the $\Lambda/\bar{\Lambda}$ polarisation.

The fraction of Λs ($\bar{\Lambda}$s) originating from Σ^0s ($\bar{\Sigma}^0$s) was roughly estimated to be 50 % [San02a] in good agreement with the literature where this fraction

is measured to be (43 ± 7) % [Yul91]. Using the ECAL, it should be possible to perform detailed studies of Σ^0s in a high statistics V^0 dataset.

Additional future data will add the possibility to study hyperons decaying into $\Lambda/\bar{\Lambda}$ + X in detail. This study is not feasible within the current data sample due to the lack of statistics.

7.6 Total systematic errors

To obtain the total systematic errors, the errors discussed so far are combined in the following way:

$$\sigma_{tot}^{syst} = \sqrt{(\sigma_{beam}^{syst})^2 + (\sigma_{\alpha}^{syst})^2 + (\sigma_{p_t}^{syst})^2 + (\sigma_{x_F}^{syst})^2} \; .$$

The results are summarised in table 7.4 for each V^0:

	K_s^0	Λ	$\bar{\Lambda}$
σ_{beam}^{syst}	0.0009	0.0052	0.0079
σ_{α}^{syst}	0	0.0015	0.0001
$\sigma_{p_t}^{syst}$	0.0016	0.0044	0.0017
$\sigma_{x_F}^{syst}$	0.0004	0.0065	0.0372
σ_{tot}^{syst}	0.0019	0.0095	0.0381

Table 7.4: Single and combined systematic errors for all V^0 signals.

The presented analysis is clearly dominated by the poor statistics (compare with the statistical errors given in table 6.1). A further improvement of the systematic errors is thus not necessary for the presented analysis.

For the upcoming measurements in 2002 the signal statistics will be a factor of 10-100 larger. The systematic errors due to the deviations between data and Monte Carlo in x_F and p_t can be reduced by adopting the kinematical model used for V^0 generation as described in equation 5.1 to the observed properties of the data by introducing, for example, the two slopes in p_t^2 as shown in figure 5.7 and reduce the fraction of FRITIOF generated $\Lambda/\bar{\Lambda}$ which have different kinematical properties. Additionally, the statistics of the generated Monte Carlo must be increased dramatically not to spoil the possible precision of the bigger real data set.

With increased statistics, the systematic error on α will also become more important. Additional studies like acceptance differences between different target wires should be performed to be able to improve the detector description in Monte Carlo.

Chapter 8

Results and discussion

Λ polarisation measurements are usually done for different bins in x_F and p_t to study the dependencies on these variables, as illustrated in section 1.3. Due to the very limited signal statistics in the used dataset (see table 5.1), however, it is not useful to subdivide the available data in more than two bins.

Table 8.1 shows the results of the polarisation analysis as described in chapter 6 using the default cuts and no weighting for the available data split in x_F at -0.06 or in p_t at 0.7 GeV/c. The values for the splitting were chosen such that the statistics of the Λ sample is roughly the same in both halves. The kinematical range stated in the table refers to the values obtained after removing up to 16 outlying events at both upper and lower edges of the distributions, keeping at least 98 % of the data.

The obtained results for the Λ are shown in figure 8.1 compared to other experiments. The achieved precision is already comparable to that of the other inclusive measurement at negative x_F by [Yul91], and within the errors the values are compatible. For the K^0_s and $\bar{\Lambda}$, where no changes of the polarisation with respect to x_F and p_t are expected, a constant was fitted to the two polarisation values obtained after splitting in x_F or p_t. Their χ^2 with respect to the fit value obtained probabilities between 9 and 79 %[1] just using the statistical errors, indicating the two values are compatible.

For the full dataset, the following transverse polarisations were found (the corresponding kinematical regions are stated in table 8.1):

$$\begin{aligned} K^0_s: &\quad -0.001 \pm 0.026 \pm 0.0019, \\ \Lambda: &\quad 0.073 \pm 0.073 \pm 0.0095, \\ \bar{\Lambda}: &\quad 0.006 \pm 0.129 \pm 0.0381, \end{aligned}$$

[1]For cutting in x_F, the probabilities are 9 % and 28 % for K^0_s and $\bar{\Lambda}$; for p_t the probabilities are 79 % and 63 % for K^0_s and $\bar{\Lambda}$.

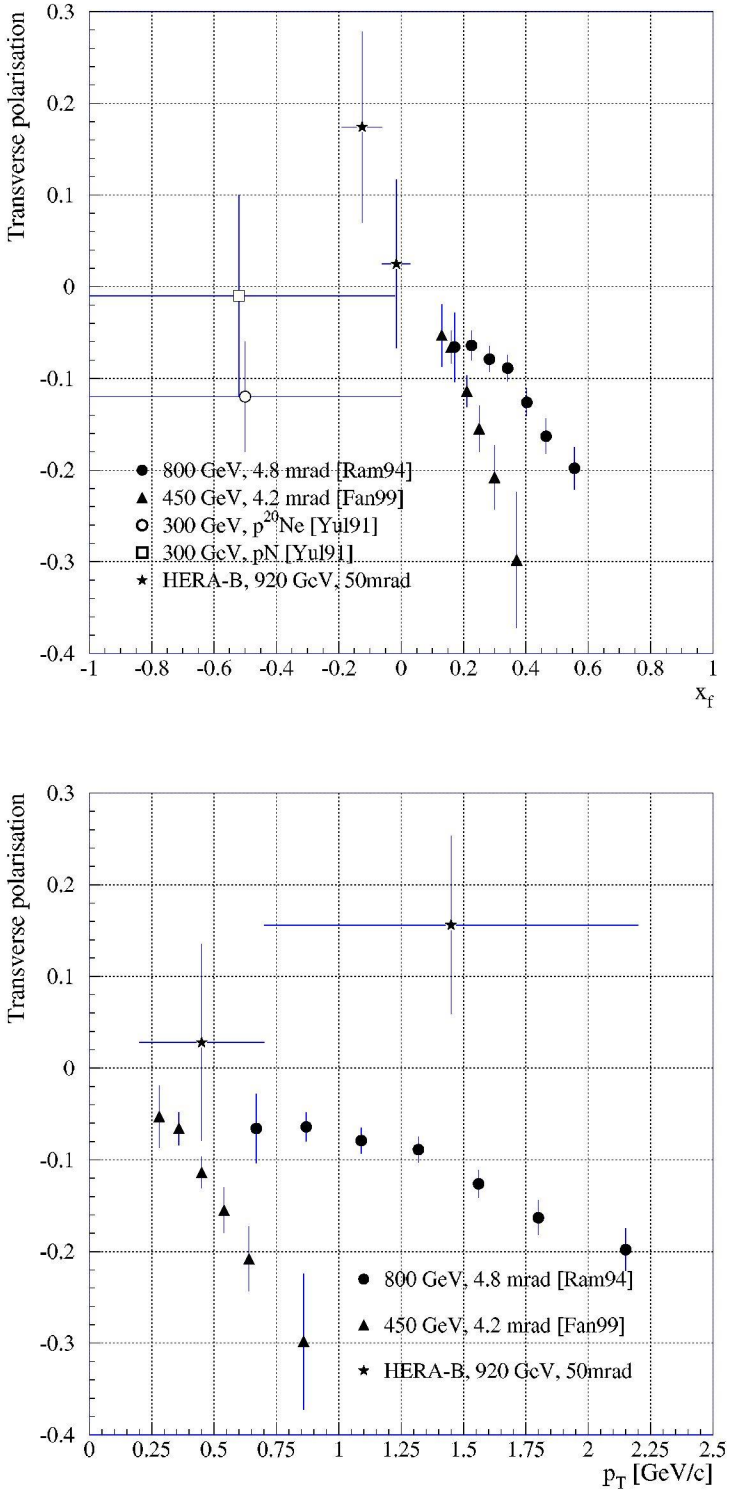

Figure 8.1: Measured Λ polarisation versus x_F and p_t: Only the statistical errors are drawn.

	splitting	p_t	x_F	polarisation
K_s^0	no	1.14 ± 1.14	-0.06 ± 0.09	-0.001 ± 0.026
	x_F	1.14 ± 1.14	-0.015 ± 0.045	0.007 ± 0.026
		1.14 ± 1.14	-0.105 ± 0.045	-0.189 ± 0.113
	p_t	1.49 ± 0.79	-0.06 ± 0.09	-0.010 ± 0.058
		0.35 ± 0.35	-0.06 ± 0.09	0.007 ± 0.029
Λ	no	1.20 ± 1.00	-0.08 ± 0.11	0.073 ± 0.073
	x_F	1.20 ± 1.00	-0.015 ± 0.045	0.025 ± 0.092
		1.20 ± 1.00	-0.125 ± 0.065	0.174 ± 0.104
	p_t	1.45 ± 0.75	-0.08 ± 0.11	0.156 ± 0.097
		0.45 ± 0.25	-0.08 ± 0.11	0.028 ± 0.107
$\bar{\Lambda}$	no	0.88 ± 0.76	-0.06 ± 0.07	0.006 ± 0.129
	x_F	0.88 ± 0.76	-0.025 ± 0.035	0.067 ± 0.165
		0.88 ± 0.76	-0.095 ± 0.035	-0.215 ± 0.199
	p_t	1.17 ± 0.47	-0.06 ± 0.07	0.032 ± 0.189
		0.41 ± 0.29	-0.06 ± 0.07	0.156 ± 0.177

Table 8.1: V^0 transverse polarisations in different kinematical regions: For each V^0, the polarisation results are shown for the full kinematic range of HERA-B and for the sample split at $x_F = -0.06$ or $p_t = 0.7\ GeV/c$. The indicated errors on the polarisation values are statistical only.

where the first error is the statistical one and the second is the systematic error as discussed in chapter 7.

The analysis shows to be self consistent since all polarisations in the production plane (y and z direction referring to the coordinate system defined in section 1.5) of each V^0 are found to be compatible with zero (see table 6.1), as expected by parity conservation in the strong interaction. For the K_s^0 being a spinless particle, also the polarisation transverse to the production plane must be zero like actually observed.

The obtained result is in addition compatible with the experimental observations concerning $\bar{\Lambda}$ polarisation which has been found to be always compatible with zero, independent of x_F and p_t.

Concerning the Λ polarisation, a value slightly different from zero could have been expected regarding the linear dependencies of Λ polarisation versus x_F and p_t. Unfortunately, no theoretical model is available explaining the phenomenon of hyperon polarisation (see section 1.4), thus no comparison can be made.

It is obvious that the presented measurements are completely dominated by the statistical errors, and, consequently, no conclusive proposition can be made about size or sign of inclusive Λ polarisation in our kinematical region, except that the value is close to zero.

8.1 Outlook

In the upcoming data taking of HERA-B, a minimum bias data sample with 10-100 times more statistics can easily be obtained. Assuming a factor of 50 in statistics would allow already to gain almost one order of magnitude in the statistical errors and provide polarisation measurements with a precision on the percent level, competitive to other experiments measuring at $x_F > 0.2$.

A sample of this size allows also meaningful measurements in the x_F and p_t regions at the edges of the detector acceptance (see figure 1.6). With the ITR being commissioned, the kinematically accessible region will be further increased in the positive x_F direction compared to the presented measurements, where the ITR was not used.

HERA-B could provide the first measurements on polarisation A dependencies in the kinematical region $x_F < 0$. So far, A dependencies have only been measured in the positive x_F region, and the effects were found to be on a few percent level [Hel85].

To be on the safe side, two data samples providing a factor of 50 more statistics compared to the presented analysis would be needed for the lightest (carbon) and heaviest (tungsten) target wire available for the 2002 running, allowing also small effects to be observed. Since HERA-B can access the target fragmentation region for the first time for those measurements, it could well be that significantly stronger effects are observed than in the previous measurements in the beam fragmentation region.

An enhanced statistical sample could facilitate even the measurement of strangeness correlations, allowing the polarisation measurement of coherently produced $\Lambda\ \bar{\Lambda}$ pairs, where for the difference of the polarisations contradicting model predictions exist: For example, according the Lund model (see section 1.4.3), Λ and $\bar{\Lambda}$ must have equal polarisations in this case, whereas the $\bar{\Lambda}$ polarisation is expected to be zero in the DeGrand and Miettinen model for that case (see section 1.4.2). HERA-B could thus contribute to the understanding of the underlying polarising physical process.

Using the ECAL for photon detection, also the main background channel to Λ polarisation measurements, $\Sigma^0 \to \Lambda\gamma$ (see section 7.5), could be further investigated which is not possible for most other experiments due to the lack of photon identification.

Since $\sim$ 10 % of the Λs/$\bar{\Lambda}$s are originating from $\Xi^0/\Xi^-/\Omega^-$ and their antiparticles, also studies of those hyperons will be possible.

The needed data samples could be taken with marginal impact to the HERA-B physics program as illustrated in appendix C.

Due to the needed very precise acceptance determination via Monte Carlo, also other analyses will profit from the experiences gained from the polarisation analysis.

8.2 Conclusion

The presented analysis has shown that hyperon polarisation measurements with HERA-B are feasible. Due to the unique kinematical range covered by the spectrometer, new insights into the phenomenon of hyperon polarisation can be gained that could lead to a better understanding of the yet unexplained polarisation effects. The measurements in the transition region between beam and target fragmentation will provide important input to the theories which is missing at the moment.

Appendix A

Comparison of V^0 properties in data and MC

This appendix illustrates the extensive studies that have been performed to check the agreement between Monte Carlo simulation and minimum bias data. All shown distributions were generated using the default cuts as described in chapter 4 and sideband subtraction without weighting (see chapter 6). To facilitate the comparison, both real data and simulation were normalised to the same integral.

The variables used for comparison are:

(a) mass: The invariant mass calculated from the V^0 track pair for the particle hypothesis found by the V^0 selection described in section 4.1.

(b) flgt: flight path of the V^0 in the V^0 rest frame (ct_0).

(c) p_{tot}: Total momentum of the V^0 candidate measured in the laboratory frame.

(d) p_z: Z (longitudinal) component of the total momentum of the V^0 candidate measured in the laboratory frame (with respect to HERA-B coordinates).

(e) Φ: Azimuthal angle of the V^0 candidate.

(f) Θ: Polar angle of the V^0 candidate.

(g) p_t: Transverse component of the total momentum (perpendicular to z) of the V^0 candidate measured in the laboratory frame (with respect to HERA-B coordinates).

(h) p_t^2: Squared transverse momentum.

(i) x_F: Feynman x of the V^0 candidate: $x_F = \frac{p_l}{p_l(max)} \approx \frac{2 \cdot p_l}{\sqrt{s}}$, with p_l being the longitudinal momentum in the centre of mass system.

Taking into account that statistics and thus statistical errors for data and simulation are comparable, the agreement for most distributions is satisfactory. The observed deviations in the mass, x_F and p_t distributions are discussed in more detail in section 5.2 and chapter 7.

Slight differences in the Monte Carlo p_t and x_F distributions between Λ and $\bar{\Lambda}$ can be explained by the fact that the fraction of $\bar{\Lambda}$s produced by FRITIOF in the $\bar{\Lambda}$ sample is much higher than the fraction of Λs produced by FRITIOF in the Λ sample. Since the generated Λ sample also provided already several hundred $\bar{\Lambda}$s being produced by FRITIOF, fewer files were generated for $\bar{\Lambda}$ using the kinematical model described in equation 5.1. As a result, approximately 38 % of the $\bar{\Lambda}$ sample were produced by FRITIOF, whereas this fraction is only roughly 15 % for the Λ sample.

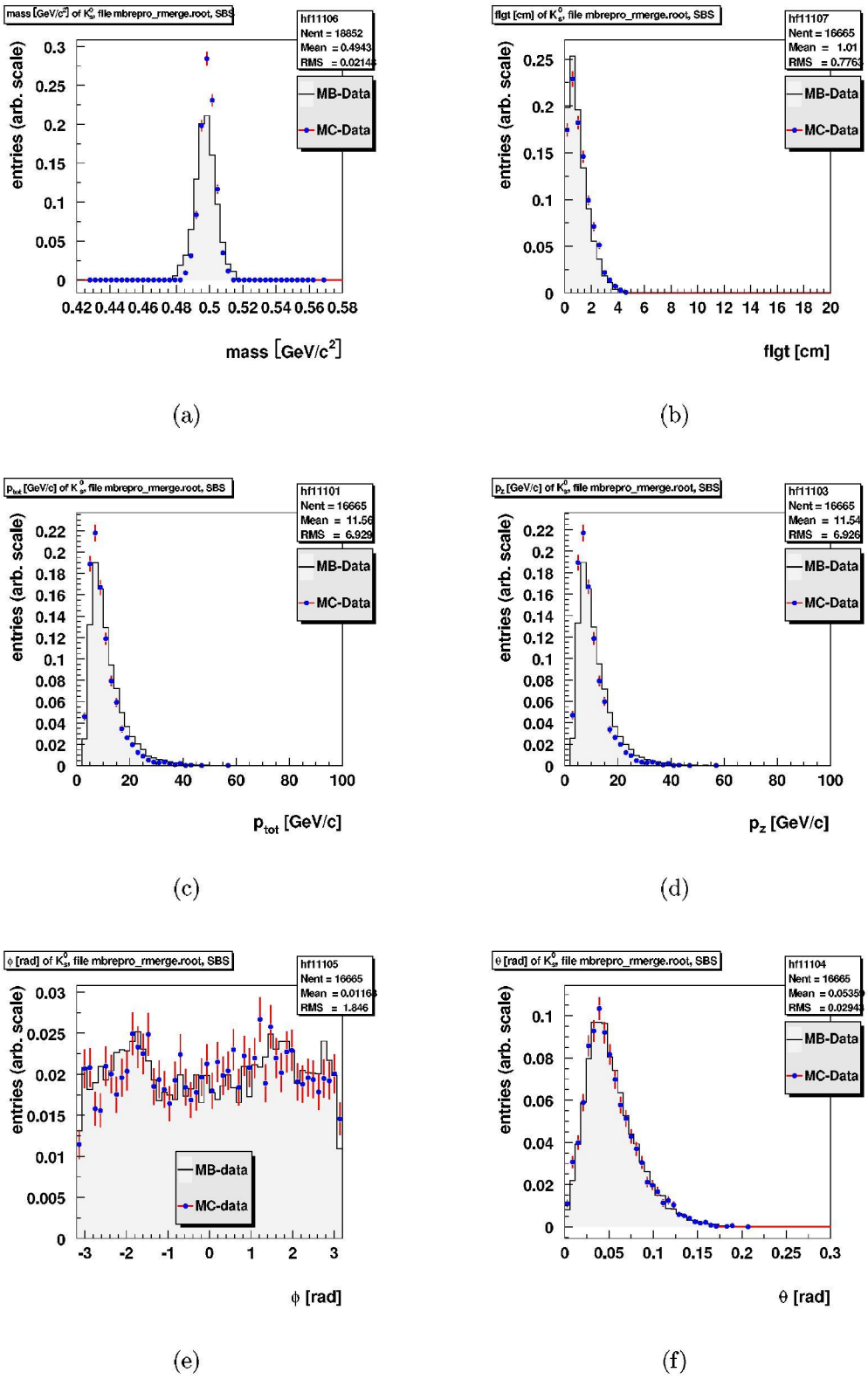

Figure A.1: Comparison of K_s^0 properties in minimum bias data (MB) and MC, part1.

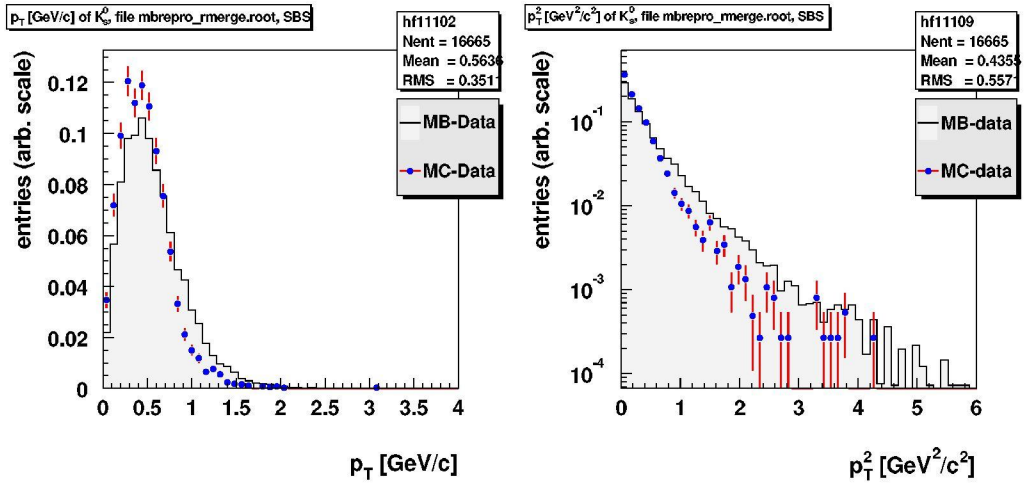

(g) (h)

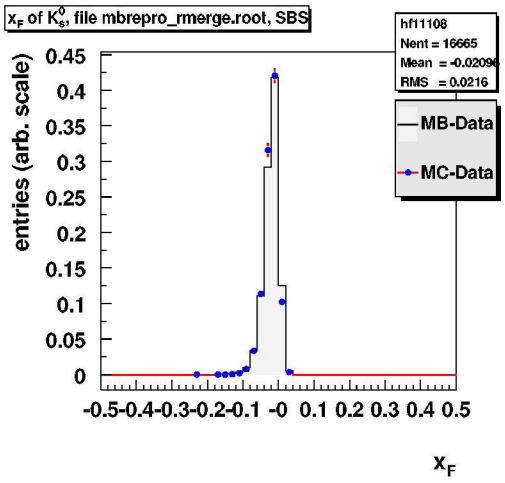

(i)

Figure A.2: Comparison of K^0_s properties in minimum bias data (MB) and MC, part2.

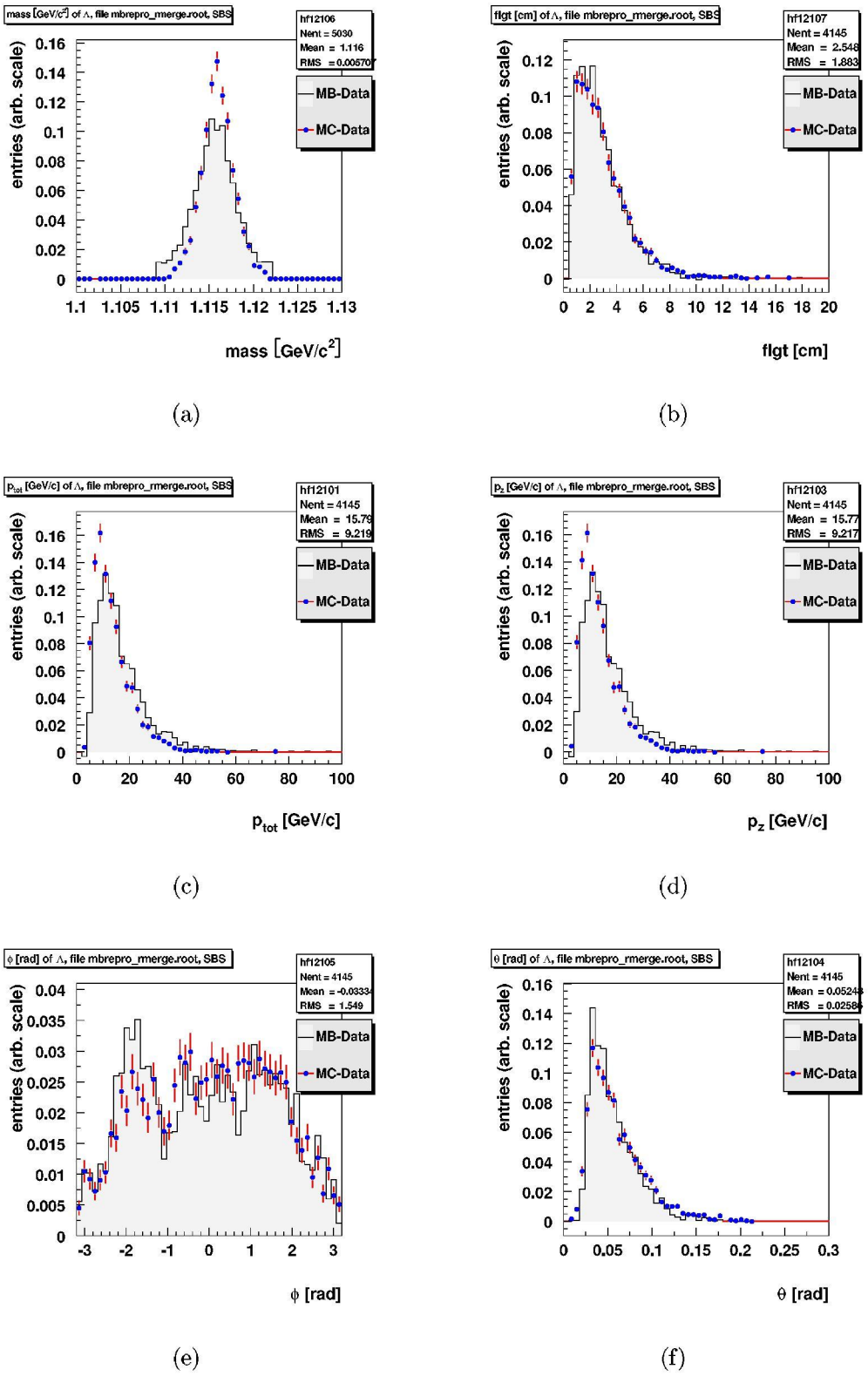

Figure A.3: Comparison of Λ properties in minimum bias data (MB) and MC, part1.

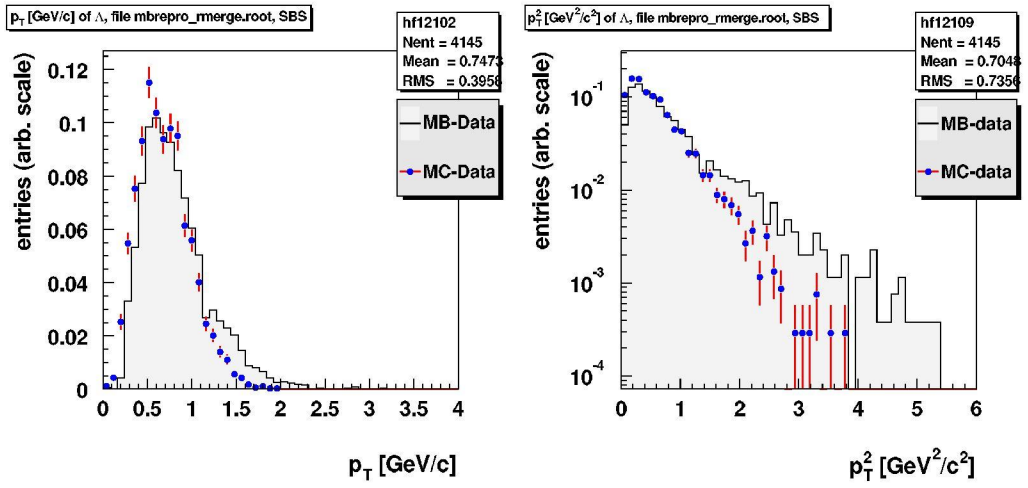

(g) (h)

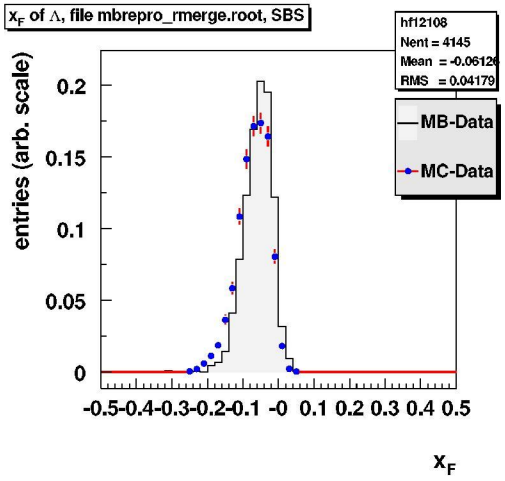

(i)

Figure A.4: Comparison of Λ properties in minimum bias data (MB) and MC, part2.

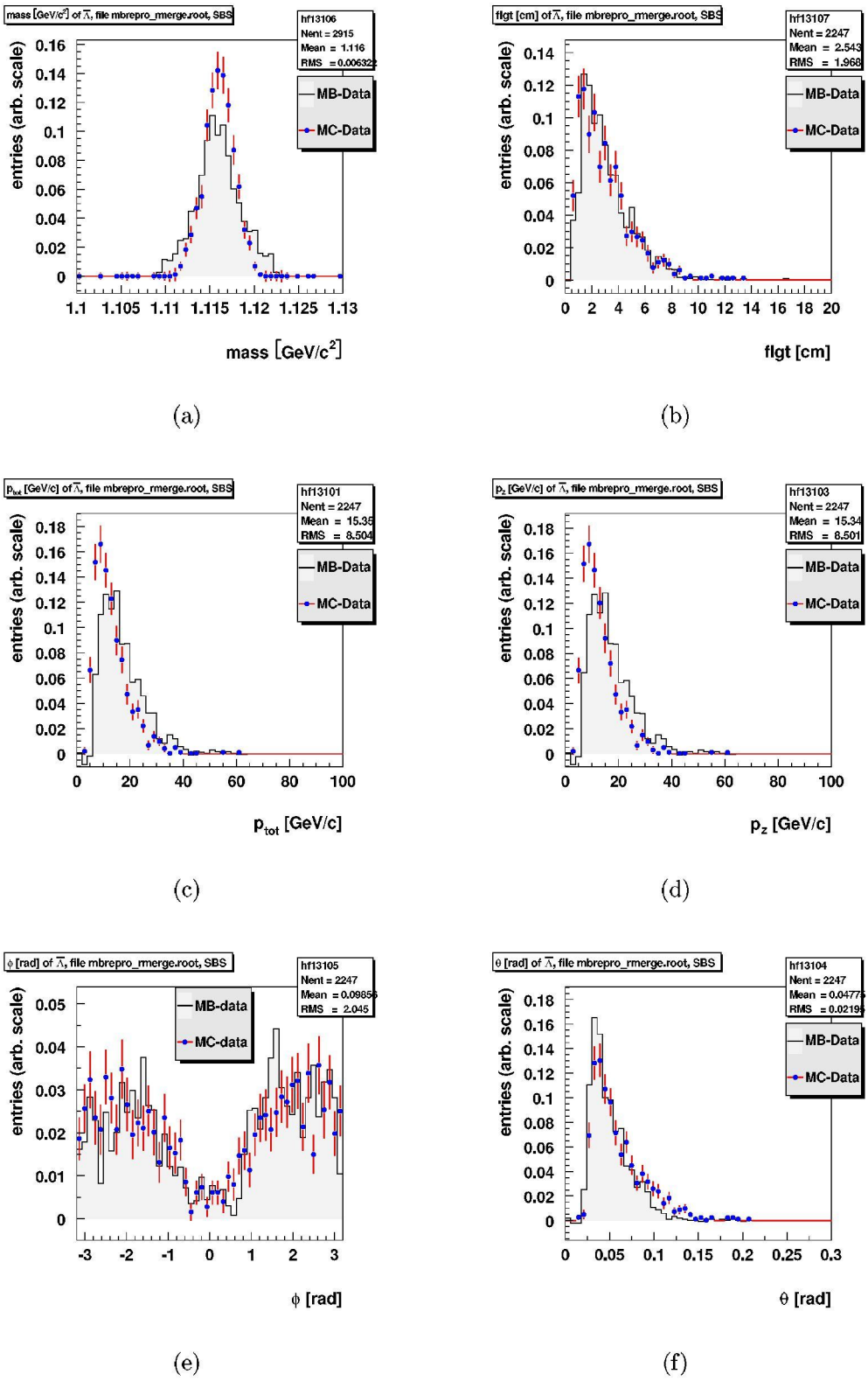

Figure A.5: Comparison of $\bar{\Lambda}$ properties in minimum bias data (MB) and MC, part1.

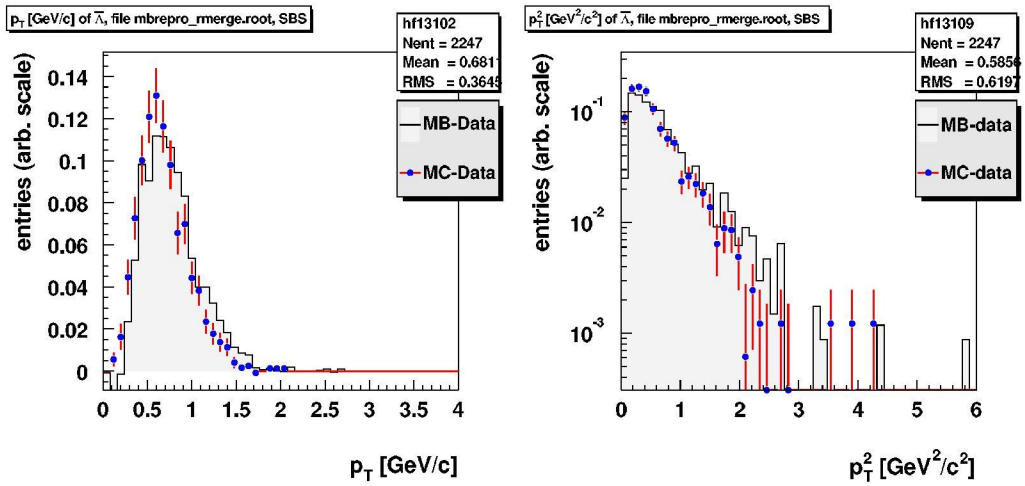

(g) (h)

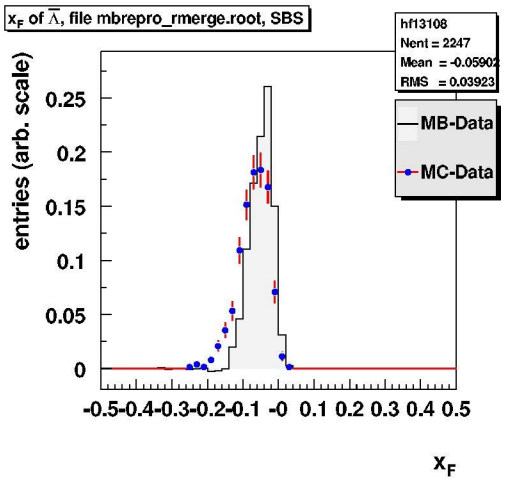

(i)

Figure A.6: Comparison of $\bar{\Lambda}$ properties in minimum bias data (MB) and MC, part2.

Appendix B

List of used minimum bias runs

This appendix lists those minimum bias runs that were used for the polarisation analysis in chronological order, starting from run 14543 taken on 10.04.2000 and ending with run 14654 taken on 14.04.2000. In total, four HERA proton fills were dedicated to minimum bias data taking. Runs that were taken using the same HERA proton fill are grouped into one table.

The applied target material, wire position, interaction rate and number of taken events are indicated as well as additional comments referring to the data taking conditions.

Rate Scan with Ti-Wire / Random Trigger ("bx")				
target rate	events	run number	events written	comments
2 MHz	20,000	14543	68711	problems with muon SC
5 MHz	20,000	14544	27888	
10 MHz	20,000	14545	25199	
10 MHz	20,000	14547	16986	bad VDS at end
5 MHz	20,000	14548	20335	
2 MHz	20,000	14549	20220	
Minimum-Bias Data with Ti-Wire / Random Trigger ("bx")				
target rate	events	run number	events written	comments
5 MHz	500,000	14551	233733	run crashed
		14552	20k	run crashed
		14553	236683	run crashed
		14554	20532	regular run end
Ti-Wire with Interaction Trigger ("interaction")				
target rate	events	run number	events written	comments
2 MHz	$\leq$ 100,000	14555	25k	did not work in trigger mode
Minimum-Bias Data with Ti-Wire / Random Trigger ("bx")				
target rate	events	run number	events written	comments
5 MHz	extra	14556	114829	up to HERMES high density run
	extra	14557	49564	stopped when disk at 96 %

Table B.1: Used minimum bias runs taken in the first HERA fill. For the stated runs solely the titanium wire (inner I) was used.

Rate Scan with C-Wire / Random Trigger ("bx")				
target rate	events	run number	events written	comments
2 MHz	20,000	14566	47k	bad BX distribution in beginning
5 MHz	20,000	14567	28k	
10 MHz	20,000	14568	29k	
10 MHz	20,000	14570	25k	
5 MHz	20,000	14571	20k	
2 MHz	20,000	14572	20k	
Minimum-Bias Data with Ti Reference Wire (Inner I) / Random Trigger ("bx")				
target rate	events	run number	events written	comments
5 MHz	40,000	14575	20k	
		14576	20k	
Minimum-Bias Data with C-Wire / Random Trigger ("bx")				
target rate	events	run number	events written	comments
5 MHz	500,000	14577	500k	
Minimum-Bias Data with Ti Reference Wire (Inner I) / Random Trigger "bx"				
target rate	events	run number	events written	comments
5 MHz	$\leq$ 100,000	14585	84k	5 bad HIPT FEDs; until Disk Full
if still within fill: C-Wire with Interaction Trigger ("interaction")				
target rate	events	run number	events written	comments
1 MHz	$\leq$ 100,000	14589	88k	

Table B.2: Used minimum bias runs taken in the second HERA fill. If not stated otherwise, the carbon wire (inner II) was used.

Rate Scan with Al-Wire / Random Trigger ("bx")				
target rate	events	run number	events written	comments
2 MHz	20,000	14591	20400	$\approx$ 30 VDS FED errors
5 MHz	20,000	14592	20456	
10 MHz	20,000	14593	21855	
10 MHz	20,000	14595	22 k	
5 MHz	20,000	14596	21452	
2 MHz	20,000	14597	18986	no bunch structure
Minimum-Bias Data with Ti Reference Wire (Inner I)/ Random Trigger ("bx")				
target rate	events	run number	events written	comments
5 MHz	40,000	14600	44291	BX1 only
		14601	30074	better bx-structure
		14604	41k	BX1 prominent
Minimum-Bias Data with Al-Wire / Random Trigger ("bx")				
target rate	events	run number	events written	comments
10 MHz		14603	370k	10 MHz to scrape coasting beam
5 MHz	500,000	14605	238k	unstable interaction rate
		14606	190k	40 % coasting beam
10 MHz		14607	100k	
Minimum-Bias Data with Ti Reference Wire (Inner I) / Random Trigger ("bx")				
target rate	events	run number	events written	comments
5 MHz	$\leq$ 100,000	14610	100k	VDS DQ-dmon crashed
if still within fill: Al-Wire with Interaction Trigger ("interaction")				
target rate	events	run number	events written	comments
1 MHz	$\leq$ 100,000	14611	104k	bad BX distribution

Table B.3: Used minimum bias runs taken in the third HERA fill. If not stated otherwise, the aluminium wire (above II) was used.

Rate Scan with W-Wire / Random Trigger ("bx")				
target rate	events	run number	events written	comments
2 MHz	20,000	14627	25k	unstable rate
5 MHz	20,000	14628	20k	unstable rate
10 MHz	20,000	14629	20k	rate between 2 and 12 MHz
10 MHz	20,000	14630	20k	unstable rate
5 MHz	20,000	14631	20k	unstable rate
2 MHz	20,000	14632	4471	e^+ beam loss
Minimum-Bias Data with Ti Reference Wire (Inner I) / Random Trigger ("bx")				
target rate	events	run number	events written	comments
5 MHz	40,000	14637	40k	
Minimum-Bias Data with W-Wire / Random Trigger ("bx")				
target rate	events	run number	events written	comments
5 MHz	500,000	14639	360 k	SL5, sector 1 of VDS OFF
		14644	160 k	SL5, sector 1 of VDS OFF
Minimum-Bias Data with Ti Reference Wire (Inner I) / Random Trigger ("bx")				
target rate	events	run number	events written	comments
5 MHz	$\leq$ 100,000	14649	90k	VDS problem
if still within fill: W-Wire with Interaction Trigger ("interaction")				
target rate	events	run number	events written	comments
2 MHz	$\leq$ 100,000	14654	90k	46 bad VDS-FEDs

Table B.4: Used minimum bias runs taken in the fourth HERA fill. If not stated otherwise, the tungsten wire (below II) was used.

Appendix C

Possibility for fast minimum bias data taking in the 2002 running period

This appendix will illustrate how a minimum bias dataset with a factor of 50 more statistics can easily be obtained with marginal impact to the HERA-B physics program in the 2002 running period.

As reference, the data taking conditions of the minimum bias dataset in 2000 will be used: Here, about 4 million events were taken using 4 HERA proton fills in a total time of about 57 hours. The data taking was limited by the logging rate of 10 MB/s which yields an event rate of 50 Hz taking into account the size of a reconstructed event of 200 kB. Since mostly a random trigger was used, 50 % of the taken events were empty, resulting in an effective sample size of 2 million events. Also the dataset was split in many runs at different data taking conditions as illustrated in appendix B, which resulted in the fact that not the full time available was used for data taking. For the following discussion, a fill duration of 12 hours will be assumed which is well below the average fill duration of the minimum bias data taking in 2000.

The key ideas to speed up the data taking would thus be to

- use an interaction trigger to avoid empty events,
- increase the logging rate and
- reduce the event size.

The logging rate can be increased by using additional logging nodes which can write the data to up-to-date hard disk drives at 20-30 MB/s. The

number of these additional logging nodes is limited to at most 2, since this corresponds to the maximal SLT network output bandwidth.

Additionally, the event size can be reduced if only the raw data are written away, where the average event size amounts to about 80 kB.

Consequently, the additional logging nodes would allow for an event rate of

$$\frac{25\ MB/s}{80\ kB} = \frac{25 \cdot 1024\ kB/s}{80\ kB} = 320\ Hz$$

each.

Assuming only one additional logging node, the total event rate amounts to 370 Hz which allows to take about 16 million events per HERA proton fill, corresponding to $\sim 1\ TB$ of data on the logging node that can be distributed over 8 off-the-shelf hard disk drives.

To gain a factor of 50 compared to the effective sample size in 2000, 100 million events would be needed that can be taken in 6.25 proton fills of 12 hours duration.

The desired factor 50 in statistics can thus be gained in less than one week data taking, compared to the 4 days of minimum bias data taking in 2000. Since minimum bias data are anyhow valuable for the detector calibration, one could think of distributing the minimum bias data taking over a longer time period, e.g. taking one fill with minimum bias data every two weeks. Since in the described data taking mode still fully reconstructed data are written to tape with 50 Hz, this part can be used for online data quality monitoring and calibration immediately.

In total, those minimum bias data should provide $\mathcal{O}(150000)$ Λs which would allow to perform the polarisation analysis with statistical errors on the percent level. As the rough estimation above shows, this dataset can be obtained easily without interference to the main HERA-B physics program.

Acknowledgements

After the thesis is finally completed, all there is left to do is to thank all the people who were helping on the way to this final goal. Of course, since this is quite an important thing to do, according to Murphy's law there will be approximately 5 seconds left for writing until everything has to be sent to the printer. Nevertheless I will try my very best not to skip anyone...

First of all, I would like to thank my supervisor Prof. Dr. Karl-Tasso Knöpfle for his companionship during the last years, for his trust in my abilities and the really interesting topic I had the opportunity to work on. Furthermore, I thank Prof. Dr. Franz Eisele for his immediate agreement to be the second referee of my thesis.

I am really indebted to many people of the HERA-B working group at Heidelberg, first of all to Dr. Federico Sánchez for the countless discussions and illuminating insights into analysis techniques that he gave to me with inexhaustible patience. THANKS!

It has been a real pleasure to discuss (not only...) physical topics with Priv. Doz. Dr. Michael Schmelling (I think I could use some Feuerzangenbowle now...), Dr. Bernhard Schwingenheuer, Dr. Thorsten Glebe (I wonder whether my badminton skills will improve, now that the thesis is finished) and Dr. Christian Bauer. My room mates Dr. Mikhail Zavertiaev, Michaela Agari and Torsten Jagla I would like to thank for the mental and moral support, their humour and of course for all the sweets (I certainly needed some sugar recently...). Of course I have always enjoyed to discuss about something completely different with the guys from the ASIC lab, even if I might have missed one or the other detail. I am grateful also to the crew at DESY for their friendly and good cooperation and support.

All the members of the HESS/HEGRA group I would like to thank for the pleasant atmosphere not only around the coffee table that I hope I can join now more frequently again. The staff, especially Mrs. Suppanz, Mrs. Häfner, Dr. Thomas Kihm and Dr. Frank Köck, should also be mentioned here for their permanent helpfulness.

My friends and former colleagues at Gießen I would like to thank for their persisting friendship and sympathy.

Last but certainly not least I would like to thank all my friends and my family that had to put up with a quite distressed Marc-André during the last months. Especially I would like to thank Martin and Steffen, and of course Petra who performed the "fine-tuning" of my English you had to bear throughout the thesis...

Finally, it is hard to find the right words to express the gratitude I feel for my parents for their support and guidance for over 28 years and for my girlfriend Verena for all her love. I think they know.

Bibliography

[Abe86] F. Abe et al., *Inclusive Lambda0 Polarization In Proton Nucleus Collisions At 12-GeV*, Phys. Rev. D **34**, 1950 (1986)

[Ada01] M. Adams et al., *The muon pretrigger system of the HERA-B experiment*, IEEE Trans. Nucl. Sci. **48**, 1270 (2001)

[Aga01] M. Agari, *Search for the decay of charmed mesons with the HERA-B detector in proton-nucleon collisions at* $\sqrt{s} = 42$ *GeV*, Diploma thesis, Universität Heidelberg, October 2001

[Ama98] S. Amato et al. [LHCb Collaboration], *LHCb technical proposal*, CERN-LHCC-98-4 (1998)

[And79] B. Andersson, G. Gustafson and G. Ingelman, *A Semiclassical Model For The Polarization Of Inclusively Produced Lambda0 Particles At High-Energies*, Phys. Lett. B **85**, 417 (1979)

[Ans01a] M. Anselmino et al., *Lambda polarization from unpolarized quark fragmentation*, Phys. Rev. D **63**, 054029 (2001)

[Ans01b] M. Anselmino, private communication, December 2001

[Ari00] I. Ariño et al., *The HERA-B Rich*, Nucl. Instrum. Meth. A **453**, 289 (2000)

[Art02] The HERA-B software group, *ARTE - HERA-B's Analysis and Reconstruction Tool*, `http://www-hera-b.desy.de/subgroup/software/` (status: March 2002)

[Aub02] B. Aubert et al. [BABAR Collaboration], *Improved measurement of the CP-violating asymmetry amplitude sin(2beta)*, HEP-EX 0203007 (2002)

[Avo01] G. Avoni et al., *The Electromagnetic Calorimeter Of The HERA-B Experiment*, Nucl. Instrum. Meth. A **461**, 332 (2001)

[Bag01] Y. Bagaturia et al., *Inner Tracker Performance in 2000*, HERA-B Internal Note 01-060 (2001)

[Bau00a] C. Bauer et al., *The HERA-B vertex detector system*, Nucl. Instrum. Meth. A **453**, 103 (2000)

[Bau00b] C. Bauer et al., *Status of the HERA-B vertex detector*, Nucl. Instrum. Meth. A **447**, 61 (2000)

[Bau02] C. Bauer et al., *Performance of the HERA-B Vertex Detector System*, submitted for publication to NIMA

[Bou95] D. Boutigny et al. [BABAR Collaboration], *BaBar technical design report*, SLAC-R-0457 (1995)

[Brä01] M. Bräuer, *Die Alignierung des HERA-B Vertexdetektors*, Dissertation, Universität Heidelberg, October 2001

[Bro81] S. J. Brodsky and G. P. Lepage, *Helicity Selection Rules And Tests Of Gluon Spin In Exclusive QCD Processes*, Phys. Rev. D **24**, 2848 (1981)

[Bun76] G. Bunce et al., *Lambda0 Hyperon Polarization In Inclusive Production By 300-GeV Protons On Beryllium*, Phys. Rev. Lett. **36**, 1113 (1976)

[Cap00] M. Capeans, *Status Of The Outer Tracker For The HERA-B Experiment*, Nucl. Instrum. Meth. A **446**, 317 (2000)

[Che95] M. T. Cheng et al. [BELLE Collaboration], *A Study of CP violation in B meson decays: Technical design report*, BELLE-TDR-3-95 (1995)

[DeG81a] T. A. DeGrand and H. I. Miettinen, *Quark Dynamics Of Polarization In Inclusive Hadron Production*, Phys. Rev. D **23**, 1227 (1981)

[DeG81b] T. A. DeGrand and H. I. Miettinen, *Models For Polarization Asymmetry In Inclusive Hadron Production*, Phys. Rev. D **24**, 2419 (1981)

[DES01] Deutsches Elektronen Synchrotron Hamburg, URL: `http://www.desy.de/` (status: May 2002)

[Duk87] E. C. Dukes et al., *Polarization of Sigma0 Hyperons in inclusive production from 28.5 GeV/c protons on Beryllium*, Phys. Lett. B **193**, 135 (1987)

[Ehr00] K. Ehret, *Commissioning Of The HERA-B Internal Target: Using The Hera Proton Ring As A B-Factory*, Nucl. Instrum. Meth. A **446**, 190 (2000)

[Ehr01] Klaus Ehret, private communication, September 2001

[Ehr02] Klaus Ehret, private communication, May 2002

[Eme00] D. Emeliyanov et al., *Primary Vertex Reconstruction by ROVER*, HERA-B Internal Note 00-139 (2000)

[Eme01a] D. Emelyanov et al., *CATS: a Cellular Automaton for Tracking in Silicon for the HERA-B vertex detector*, Published in Beijing 2001, CHEP, 160, September 2001.

[Eme01b] D. Emeliyanov et al., *OTR/ITR-CATS: Tracking Based on Cellular Automaton and Kalman Filter*, HERA-B Internal Note 01-137 (2001)

[Eme01c] D. Emeliyanov et al., *Grover*, available at:
`http://wwwhera-b.mppmu.mpg.de/analysis/grover.html`
(status: March 2002)

[Erh79] S. Erhan et al., *Lambda0 Polarization In Proton-Proton Interactions At S**(1/2) = 53-GeV And 62-GeV*, Phys. Lett. B **82**, 301 (1979)

[Fal98] W. Fallot-Burghardt, *A CMOS Mixed-Signal Readout Chip for the Microstrip Detectors of HERA-B*, Dissertation, University of Heidelberg, June 1998.

[Fan99] V. Fanti et al., *A measurement of the transverse polarization of Lambda hyperons produced in inelastic p N reactions at 450-GeV proton energy*, Eur. Phys. J. C **6**, 265 (1999)

[Fel99] J. Felix, *On Theoretical Studies Of Lambda0 Polarization*, Mod. Phys. Lett. A **14**, 827 (1999)

[Fel02] J. Felix et al. [E690 Collaboration], *Lambda0 polarization in 800-GeV/c p p → p(f) (Lambda0 K+)*, Phys. Rev. Lett. **88**, 061801 (2002)

[Fun99] Michael Funcke, *Alignment der HERA-B Targetmechanik*, Diploma thesis, Universität Dortmund, March 1999

[GEA94] *GEANT 3.21 Detector Description and Simulation Tool*, CERN Program Library Long Writeup W5013, CERN, Geneva (1994), available at: `http://wwwinfo.cern.ch/asdoc/Welcome.html`
(status: March 2002)

[Gro00] D.E. Groom et al., The European Physical Journal C **15** (2000) 1 and 2001 off-year partial update for the 2002 edition available on the PDG WWW pages (URL: `http://pdg.lbl.gov/`)

[Gun79] J.F. Gunion, *Short distance counting rules for low p_t fragmentation*, Phys. Lett. B **88**, 150 (1979)

[Har98] P. F. Harrison and H. R. Quinn [BABAR Collaboration], *The BaBar physics book: Physics at an asymmetric B factory*, SLAC-R-0504 (1998)

[HB94] T. Lohse et al., *HERA-B – An Experiment to Study CP Violation in the B System Using an Internal Target at the HERA Proton Ring*, Proposal, DESY-PRC 94/02, May 1994

[HB95] H. Albrecht et al., *HERA-B – An Experiment to Study CP Violation in the B System Using an Internal Target at the HERA Proton Ring*, Technical Design Report, DESY-PRC 95/01 (January 1995)

[HB00] The HERA-B collaboration, *Report on status and prospects*, DESY-PRC 00/04 (October 2000)

[HB02] The HERA-B collaboration, M. Zavertiaev et al., *V^0 inclusive production cross sections - Technical note*, in preparation.

[Hel78] K. Heller et al., *Polarization Of Lambdas And Anti-Lambdas Produced By 400-GeV Protons*, Phys. Rev. Lett. **41**, 607 (1978)

[Hel83] K. Heller et al., *Polarization Of Xi0 And Lambda Hyperons Produced By 400-GeV/c Protons*, Phys. Rev. Lett. **51**, 2025 (1983)

[Hel85] K. Heller, *Inclusive hyperon polarization: a review*, J. de Physique C2 V **46**, 121 (1985)

[Hel90] K. Heller, *Hyperon Polarization At High Energy: A Tool To Investigate The Strong Interaction*, J. Phys. Colloq. **51**, 163 (1990)

[Her00] J. M. Hernández et al., *HERA-B Data Acquisition System*, Proceedings of the IEEE NPSS conference, Lyon (October 2000)

[Her02] J. M. Hernández, *Reprocessing*, available at: `http://www-hera-b.desy.de/subgroup/software/arte/reco/RP.html` (status: March 2002)

[Ho90] P. M. Ho et al., *Production Polarization And Magnetic Moment Of Anti-Xi+ Anti-Hyperons Produced By 800-GeV/c Protons*, Phys. Rev. Lett. **65**, 1713 (1990)

[Igo98] O. Igonkina, *MARPLE -Version 1.03-*, HERA-B Internal Note 98-129 (1998); a more recent online manual (version 3.04) can be found on:
`http://www-hera-b.desy.de/subgroup/software/arte/MARPLE`
(status: March 2002)

[Iva99] J. Ivarsson et al., *PYTHIA and FRITIOF: Event Generators for HERA-B*, HERA-B Internal Note 99-067 (1999)

[Kis99] I. Kisel and S. Masciocchi, *CATS - A Cellular Automaton for Tracking in Silicon for the HERA-B Vertex Detector*, HERA-B Internal Note 99-242 (1999)

[Kob73] M. Kobayashi and T. Maskawa, *CP-Violation in the Renormalizable Theory of Weak Interaction*, Prog. Theor. Phys. **49**, 652 (1973)

[Kre01] P. Kreuzer [HERA-B Collaboration], *Experience With HERA-B Triggering*, Nucl. Instrum. Meth. A **462**, 212 (2001)

[Lac91] J. Lach, *Hyperons: Insights into baryon structures*, FERMILAB-CONF-91-200 (1991)

[Lun89] B. Lundberg et al., *Polarization In Inclusive Lambda And Anti-Lambda Production At Large P(T)*, Phys. Rev. D **40**, 3557 (1989)

[Mag95] A. Maggiora, *Spin And Strangeness At Saturne*, Nucl. Phys. News **5**, 23 (1995)

[Mor93] A. Morelos et al. [E761 Collaboration], *Polarization of Sigma+ and anti-Sigma- hyperons produced by 800-GeV/c protons*, Phys. Rev. Lett. **71**, 2172 (1993)

[Now94] S. Nowak, *A Description of HERA-B GEANT*, HERA-B Internal Note 94-123 (1994); a more recent online description can be found on:
`http://www-hera-b.desy.de/subgroup/software/arte/gean/hbgean.html`
(status: March 2002)

[Per82] D.H. Perkins, *Introduction to High Energy Physics*, 2nd edition, Addison-Wesley, 1982

[Pes01] R. Pestotnik, *Identification of Pions, Kaons and Protons in the HERA-B Spectrometer*, Dissertation, University Lljubljana, January 2001

[Pi92] H. Pi, *An event generator for interactions between hadrons and nuclei - FRITIOF version 7.0*, Comp. Phys. Comm. **71**, 173 (1992)

[Ple01] M.-A. Pleier, *Cloneremove V1.0*, HERA-B Internal Note 01-062 (2001)

[Pod54] J. Podolanski and R. Armenteros, *Analysis of V-Events*, Phil. Mag. **45**, 13 (1954)

[Pon85] L. G. Pondrom, *Hyperon Experiments At Fermilab*, Phys. Rept. **122**, 57 (1985)

[Pyr98] J. Pyrlik, *Schematic drawing of the HERA-B detector*, `http://www-hera-b.desy.de/subgroup/pictures/detector_schematic.eps`

[Ram94] E. J. Ramberg et al., *Polarization of Lambda and anti-Lambda produced by 800-GeV protons*, Phys. Lett. B **338**, 403 (1994)

[San01] F. Sánchez, private communication, December 2001

[San02a] F. Sánchez, private communication, February 2002

[San02b] F. Sánchez, private communication, April 2002

[San02c] F. Sánchez et al., *HERA-B Data Acquisition System*, to be published in NIMA

[Sav98] V. Saveliev [HERA-B Collaboration], *The HERA-B Transition Radiation Detector*, Nucl. Instrum. Meth. A **408**, 289 (1998)

[Sch01] A. Schreiner, *Aging Studies of Drift Chambers of the HERA-B Outer Tracker Using CF4 based Gases*, Dissertation, Humboldt-Universität Berlin, November 2001

[Sjö94] T. Sjöstrand, *PYTHIA 5.7 and JETSET 7.4 - Physics and Manual*, Computer Physics Commun. **82**, 74 (1994), hep-ph/9508391

[Spr00] S. Spratte, *Bestimmung der Wechselwirkungsrate des HERA-B Targets und Untersuchung des Coasting Beam am HERA Protonen-Ring*, Dissertation, Universität Dortmund, June 2000

[Tit00] M. Titov [HERA-B Muon Collaboration], *The Muon System In The HERA-B Experiment*, Nucl. Instrum. Meth. A **446**, 355 (2000)

[Tro89] L. H. Trost et al., *New Measurement Of The Production Polarization And Magnetic Moment Of The Cascade Minus Hyperon*, Phys. Rev. D **40**, 1703 (1989)

[Tru00] U. Trunk, *Development and Characterisation of the Radiation tolerant HELIX128-2 Readout Chip for the HERA-B Microstrip Detectors*, Dissertation, University of Heidelberg, July 2000.

[Wag99] W. Wagner, *Auswertung der Daten des HERA-B Vertexdetektors im Hinblick auf die physikalischen Eigenschaften der verwendeten Siliziumstreifenzähler*, Dissertation, Ludwig-Maximilians-Universität München, December 1999.

[Wah85] Y. W. Wah et al., *Measurement Of Sigma- Production Polarization And Magnetic Moment*, Phys. Rev. Lett. **55**, 2551 (1985)

[Wil87] C. Wilkinson et al., *Polarization And Magnetic Moment Of The Σ^+ Hyperon*, Phys. Rev. Lett. **58**, 855 (1987)

[Wol83] L. Wolfenstein, *Parametrization of the Kobayashi-Maskawa Matrix*, Phys. Rev. Lett. **51**, 1945 (1983)

[Yul91] B. S. Yuldashev et al., *Neutral Strange Particle Production In P Ne-20 And P N Interactions At 300-GeV/c*, Phys. Rev. D **43**, 2792 (1991)

[Zav02] M. Zavertiaev, private communication, February 2002

[Zeu00] T. Zeuner [HERA-B Collaboration], *The Msgc-Gem Inner Tracker For HERA-B*, Nucl. Instrum. Meth. A **446**, 324 (2000)

[Zoc00] A. Zoccoli [HERA-B Collaboration], *The Electromagnetic Calorimeter Of The HERA-B Experiment*, Nucl. Instrum. Meth. A **446**, 246 (2000)